SENSORS IN AGRICULTURE: SYSTEMS AND METHODS FOR TWO SENSOR SYSTEMS FOR PLANT PHENOTYPE DETECTION

A Dissertation

by

GEORGE CODY BAGNALL

Submitted to the Office of Graduate and Professional Studies of
Texas A&M University
in partial fulfillment of the requirements for the degree of

DOCTOR OF PHILOSOPHY

Chair of Committee,	J. Alex Thomasson
Co-Chair of Committee,	Cristine L. S. Morgan
Committee Members,	Stephen W. Searcy
	William Rooney
Head of Department,	Stephen W. Searcy

December 2020

Major Subject: Biological and Agricultural Engineering

ABSTRACT

Sensors are increasingly being used in agricultural settings to provide data on the physical characteristics of plants under field conditions. Accurate data provides researchers and producers with the ability to make decisions with a high level of confidence. This work addresses two sensing systems for measuring important plant characteristics. The first system investigates accuracy differences between two unmanned aerial vehicle (UAV) camera calibration methods. The second system explores the development and testing of a novel *in situ* root imaging rhizotron. The UAV study compared autoexposure and fixed exposure radiometric calibration methods to a single calibrated manned aircraft image and to a ground target measured with a spectroradiometer. In a band by band comparison, the autoexposure method, which uses a pre-flight image of a single panel for calibration, produced almost twice as much radiometric error on average compared with fixed exposure using in-field targets for image calibration. When comparing the exposure methods using the Visible Atmospherically Resistant Index (VARI), the autoexposure method produced twice as much RMSE compared to the fixed exposure method. The study on the novel *in situ* root sensor developed a low field magnetic resonance imaging (LF-MRI) rhizotron. A scaled 8 cm bore model was designed, built and tested across three types of soil, Weswood silt loam, Belk clay, and Houston black clay. The results demonstrated the viability of this technology to produce root information in clay soils. A 28 cm bore unit was designed, built and tested under field conditions. The resulting system provided root information and visualization of roots with 2-D projection images in a Weswood silt loam, and Belk clay both *in situ* and *ex situ*. In summary, (1) using a fixed exposure calibration method for UAV remote sensing improved accuracy in reflectance data, providing a better understanding of in-field plant conditions and better decision-making capability; and (2) the LF-MRI Rhizotron allowed visualization of plant roots in agricultural soils under field conditions. Both sensing systems and methods have the potential to be used as tools for improving crop production for researchers or growers.

DEDICATION

I dedicate this dissertation, and the years of work that went into it to my lovely wife Dianna. Your encouragement, and conversation provided the emotional stamina to persevere when things were tough. You were never afraid to lend a hand, either in field work or scientific discussion. I love you, and I would not be here without you.

ACKNOWLEDGEMENTS

I would like to thank my committee chair Dr. Thomasson for his guidance, trust and support while performing this research. I would like to thank my Co-Chair Dr. Morgan for her guidance, and support; trusting me to get the job done and guiding me to be a better scientist. I would like to thank my other committee members Dr. Searcy and Dr. Rooney for their support throughout the course of this research.

I would like to acknowledge and thank Richard Epting for his help in design and fabrication of various parts for my research. Without his expertise and friendship this work would not have been as efficient or functional as it is.

I would like to thank my friends, who listened and asked questions and supported me through this work even when they did not understand what I was rambling on about. I thank you for your moral, physical and nutritional support.

Most importantly I would like to thank my wife, Dianna Bagnall, for her support and encouragement. I thank you for the many conversations, and questions which made me think and the support and encouragement to not only find the answers but to be able to communicate them well. I thank you for your willingness to put up with long hours or to rush to the field and help me put things back together when everything is blown apart.

CONTRIBUTORS AND FUNDING SOURCES

Contributors

This work was supervised by a dissertation committee consisting of Professor J. Alex Thomasson, and Professor Steve Searcy of the Department of Biological and Agricultural Engineering and by Professor Cristine Morgan of the Soil and Professor William Rooney of the Department of Soil and Crop Science.

The data analyzed in Chapter 2 was collected with the help of Tianyi Wang, and Chenghai Yang at USDA-ARS. The analyses depicted was conducted in part by Tianyi Wang, Xiongzhe Han, Chao Sima, and A. J. Chang. The data that was analyzed for Chapter 3 was provided by ABQMR Inc., and Brock Weers. The analyses depicted in Chapter 3 were conducted in part by Neha Koonjoo of the Athinoula A. Martinos Center for Biomedical Imaging, Radiology Department. The work in chapter 3 was published in 2020 with co-authors Neha Koonjoo, Stephen A. Altobelli, Mark S. Conradi, Eiichi Fukushima, Dean O. Kuethe, John E. Mullet, Haly Neely, William L. Rooney, Karl F Stupic, Brock Weers, Bo Zhu, Matthew S. Rosen, Cristine L. S. Morgan.

All other work conducted for the dissertation was completed by the student independently.

Funding Sources

Graduate study was supported by a fellowship from Texas A&M University and the UAV research was funded by Texas A&M AgriLife agency as a part of the

Unmanned Aerial Systems Project for Precision Agriculture and High Throughput Field Phenotyping research project.

The LF-MRI work was also made possible by the Advanced Research Projects Agency-Energy (ARPA-E), U.S. Department of Energy, under Award Number DE-AR0000823. Its contents are solely the responsibility of the authors and do not necessarily represent the official views of the United States Government or any agency thereof.

NOMENCLATURE

UAV	Unmanned Aerial Vehicle
MAV	Manned Aerial Vehicle
VARI	Visible Atmospheric Resistance Index
NIR	Near Infrared Radiation
DN	Digital Number
PA	Precision Agriculture
HTP	High Throughput Phenotyping
GPS	Global Position System
GCP	Ground Control Point
RGB	Red, Green, Blue
PVC	Polyvinyl Chloride
ELM	Empirical Line Method
AGL	Above Ground Level
AOI	Area of Interest
RMSE	Root Mean Squared Error
LF-MRI	Low Field Magnetic Resonance Imaging
HF-MRI	High Field Magnetic Resonance Imaging
MR	Magnetic Resonance
MRI	Magnetic Resonance Imaging
NMR	Nuclear Magnetic Resonance

RF	Radio Frequency
SNR	Signal to Noise Ratio
AUTOMAP	Automated Transform by Manifold Approximation
OD	Outside Diameter
AWG	American Wire Gauge
IFFT	Inverse Fast Fourier Transform
FFT	Fast Fourier Transform

TABLE OF CONTENTS

Page

LIST OF FIGURES

Page

LIST OF TABLES

Page

1. INTRODUCTION

For centuries humans have been working to improve their livelihoods and security by increasing crop yields through phenotypic measurements in plant selection and breeding programs [1]. Food security is still a major concern in the world today, with over 800 million people undernourished [2]. The underlying purpose of the research described in this dissertation is to provide solutions to food security problems by advancing the science involved in agricultural production and research. Specifically, this research addresses gaps in the areas of above-ground remote sensing and below-ground proximal sensing as methods of plant phenotyping.

The International Society of Precision Agriculture defines precision agriculture (PA) as “a management strategy that collects and analyzes temporal, spatial and individual data and uses this information to support management decisions” [3]. The goal of this strategy is to use technological advances such as global positioning systems (GPS) and variable rate technology to integrate spatial and temporal information to improve farming decisions involving economic and environmental considerations [4]. Historically PA technologies and processes have included the use of GPS [4], soil and plant mapping [5], and spatially and temporally variable applications of crop inputs like nutrients, seeds, pesticides and irrigation water [6]. PA often relies on proximal sensors such as yield monitors for estimating crop yield [7] and remote sensors such as satellites for monitoring crop stress [8].

Plant breeding, and specifically the area of phenomics, is an area of research that has used many of the sensors mentioned above. Phenomics is focused on the development and use of technologies that provide quantitative plant phenological data at a fine spatial resolution. The purpose of the growing investments in these types of technologies is to increase the speed of phenotyping, have reliable and repeatable measurements, and discover new measurements that can give insight into plant function. Field-based high throughput phenotyping (HTP) is a subset of phenomics that focuses on collecting spatially intensive phenotypic measurements of plant-breeding trials. HTP uses technological advances to phenotype larger numbers of plants, thus giving plant breeders quick access to acquired data sets for efficient selection of plants for the purpose of improving crop varieties. Strong correlations have been found between HTP data from remote sensing and those collected with more traditional methods [9]. Examples in the literature include grain yield production estimations from canopy reflectance [10] and comparisons between UAV and field phenotyping methods to assess yield and nitrogen use efficiency in barley [11] .

Sensing the above-ground portion of a crop is the most common use of sensors in precision agriculture and HTP. In remote sensing, plant properties are measured from a distance, commonly using reflectance in the visible and near infrared VIS/NIR [12] and/or thermal portions of the electromagnetic spectrum [13]. VIS/NIR bands have been used for crop monitoring, yield predictions, plant nutrient monitoring, and to understand general crop stress [14].

For farmers and plant breeders to make useful decisions with remotely sensed data, the error in the data needs to lie within an allowable range from the true value of the object of interest. For example, normalized difference vegetative index (NDVI) values, based on red and NIR reflectance, are often used for mapping crop stress across a field. Calibrating the sensor and the data helps reduce the error, providing more confidence in decisions based on the data. Remote sensing with Unmanned Aerial Vehicles (UAVs) is a rapidly growing means of data collection for HTP and PA, and as such it should also employ calibration methods to generate data that are accurate enough to be used for decision-making processes.

The below ground portion of the plant is equally important, but more difficult for field-based phenotyping. Roots provide support, biosynthesis of important hormones and are involved in functions occurring in the rhizosphere such as water and nutrient extraction. By being able to quantify plant rooting behavior, *in situ*, it is possible to select plants in order to optimize the soil ecosystem services for improving carbon sequestration, crop yield and provide for more sustainable agricultural ecosystems for improving crop production for the future [15]. Under nutrient-limiting conditions, increases in agricultural production are also thought possible by direct modification to root system architecture (RSA) [16] , which is known to be important for water and nutrient uptake, specifically in arid regions [17]. At the same time, RSA has been largely unrepresented in plant phenotyping and plant breeding [18].

HTP gives researchers and producers the ability to better understand crop responses to the environment the plants are growing in and help improve decision making. In this work two sensor systems and methods for HTP have been studied. One study involves an above ground UAV based radiometric calibration method to quantify the error associated with two multispectral camera exposure systems. The second study involves the development of a novel low field magnetic resonance imaging rhizotron for *in situ* root imaging. Both studies have focused on accurate, field-based, measurement of important plant phenotypes.

2. UAV RADIOMETRIC CALIBRATION: A COMPARISON OF AUTO EXPOSURE AND FIXED EXPOSURE SYSTEMS

2.1. Literature Review

The timing and amount of available information can have major consequences on agricultural business decisions, and the objectivity of the information is critical for making appropriate decisions [19]. Sensors can give agricultural producers the ability to better understand the environment their crop is growing in and improve their decision-making. One type of sensor data that can be gathered is images. Two main types of information can be collected from images: spatial information like object size, shape, position and texture (e.g., stalk thickness of sorghum plants) [20]; and spectral information like reflectance values at specific wavelengths, which has been used to indicate numerous crop stresses such as spider mite infestation [21], nitrogen deficiency and water stress [22]. Spectral information is often used in vegetative indices such as NDVI [23]. Having accurate reflectance data is a key factor for generating actionable information from remote sensing [24]. There is a relationship between the arbitrary digital number (DN) in an image, which is affected by the cameras adjustable parameters, and the reflectance of the target in the image. The error in calculating this relationship is reduced by including corrections for known distortions such as atmosphere, illumination, and camera properties [25]. The conversion from DN to reflectance is a critical step in generating reliable NDVI data [26]. These NDVI values must be generated from calibrated reflectance maps – i.e., images converted from DN to reflectance – or they are not comparable to other NDVI values [27] collected at different times or locations or by different sensors. To produce the most useful (i.e. low error) data from remote sensing platforms, calibration must be performed to generate a relationship between the DNs and reflectance values. Radiometric calibration is used to convert the DN output from the sensor to target reflectance, which can then be compared across dates, locations, and sensors.

Traditionally, researchers have conducted remote sensing surveys for PA and HTP using satellites and manned aerial vehicles (MAVs). Each has its own applications and limitations. Satellite sensors are calibrated before they are launched into space, but over time drift or other problems occur that result in the need for re-calibration. This calibration is performed by measuring objects on the ground and comparing their known reflectance to the digital number generated by the sensor. This post-launch calibration method is called invariant or vicarious calibration, and it is based on the relationship between the at-sensor radiance and the reflectance of ground-based, homogeneous, and commonly natural targets [28].

Satellites have been used for PA [29], studies in ecology [30], and evaluation of natural disasters [31] among other subjects. Satellites are a very stable platform [32] and are unique in being able to provide a single image that covers a large section of land, allowing (for example) monitoring of crop disease over large areas [33], and they have proven useful for measuring global chlorophyll fluorescence to estimate global CO_2 assimilation [34]. Satellites typically have relatively low resolution [35], with Landsat 4 thematic mapper having a resolution of 30 m for all bands except the IR band, which is at 120 m [36]. This low resolution is being improved as newer satellites are being launched, such as the WorldView-2, which has approximately 0.5 m resolution [37]. The cost may be prohibitive, though, with WorldView-2 data costing $17.50/sq. km for a single acquisition with a 25 sq. km minimum [38]. In addition to cost, one of the greatest problems with satellites for PA decision making is the time constraints associated with satellite data. For example, Landsat 8 passes overhead every 16 days [39], a span that can cause important phenological stages to be missed [35]. Also, if cloud cover obstructs the image on the day a satellite is overhead, the time span between data collection events doubles. It should be noted that the spatial resolution and period of newer satellites are improving all the time; for instance, the Pleiades constellation provides a period of 1 day and offers 0.5 m image resolution for 4-band multispectral imagery, at a cost of $25/km^2 with a 25 km^2 minimum [40].

MAVs have been used as remote sensing imaging platforms for many years. These are often relatively small single engine, propeller-driven aircraft, such as the Sky Arrow (Skyarrow, Lowcountry Aviation, Walterboro SC USA) [35], or the Cessna 205 (Cessna 205, Textron Aviation, Wichita KS USA) [41]. This type of platform served as the midpoint for many years between ground-based sensing platforms and satellites. With current cameras MAVs can achieve spatial resolution on the level of 5 cm, [42] and they are able to repeat surveys quicker than the typical satellite. However, there are some drawbacks that come with using MAVs. The cost associated with manned flights can often be prohibitive for surveys, particularly for applications that require repetitive flights. Turbulence and air traffic also can be a problem for completing surveys in a timely manner [32].

Unmanned Aerial Vehicles have become prevalent as imaging platforms in research studies because of their unique potential. They come in a variety of size classifications [30] typically and are able to carry a wide variety of sensors [43], with most UAVs in agriculture falling under the small UAS classification as provided by the United States Federal Aviation Administration [44]. Their ability to carry sensors at a low altitude and relatively low speed presents opportunities for even higher spatial resolution. The most common sensors used for both PA and plant breading applications have been multispectral cameras including standard red, green and blue (RGB) visible light cameras [29], color infrared and other multispectral cameras [45], and thermal cameras [46].

In one study, researchers performed a comparison of image data from satellites, MAVs, and UAVs over a 2.5 ha vineyard in Italy. The RapidEye satellite images were purchased pre-calibrated, while the MAV camera was calibrated with proprietary software by Terrasystem (Viterbo VT, Italy) and an atmospheric calibration was applied with ENVI software (Boulder, CO, USA). The UAV calibration was conducted by taking a white reference image pre-flight at ground level and measuring reflectance spectra of the white reference panel with a spectroradiometer. The reflectance spectra were used to convert the image DNs to reflectance. This study determined that the UAV had a higher NDVI range (0.08 vs. 0.04 for MAVs and 0.02 for satellites) as well as a larger standard deviation than the other two platforms [35], suggesting that the UAV captured more spectral variability due to its higher image resolution. Another line of investigation has been to use UAVs in conjunction with satellites. In an example of calibration in this type of work, an octocopter with a five-band multispectral camera (RedEdge, Micasense, Seattle WA USA) was used to collect images over a field that were stitched together into a mosaic. The UAV image mosaic was calibrated with 17-color ethylene vinyl acetate targets placed in the field based on the empirical line method. Exposure settings were not discussed in the article, but it is likely that the auto exposure (default) setting was used. It was found that the UAV data overestimated the reflectance when compared to ground-based measurements, the near infrared radiation (NIR) band calculated reflectance values being 15 to 18% higher than the measured values [47]. These results show that higher resolution data from UAVs can have inherent biases, thus calibration techniques need to be well understood and applied in order to generate quality data.

As researchers and producers investigate ways to use UAVs in agriculture, reducing the error by improving calibration continues to be an important area of investigation. Wang and Myint hypothesized that the standard empirical line method historically used for radiometric calibration produces errors that become more pronounced with the type of sensors typically used with UAVs. They used nine gray scale Masonite boards from 5% to 90% reflectance as field targets, and they flew a Spreading Wings S800 hexacopter (DJI Inc., Nanshan, Shenzhen, China) with a color infrared camera (Canon Rebel T4i, Canon, Ota City, Tokyo, Japan) to investigate the relationship between DN and reflectance. The targets were placed such that the full gray scale shows up in each UAV image and showed a relationship between DN and reflectance was exponential. By applying a logarithmic transformation, a linear regression equation with a high R^2 (~0.99) was produced for the green, red, and NIR bands, and referred to by the authors as the simplified ELM. The simplified ELM equations were then used to calibrate images only one gray calibration target in each image and the data was compared with spectroradiometer measurements of 10 points by conducting a Mann-Whitney U test. This test showed no statistical difference between the 10 ground measurements and the UAV calibrated reflectance [48]. The exponential response curve of the cameras plays a large role in determining the proper application of calibration equations such as the empirical line method and should be considered when designing a calibration system.

Pozo et. al. tested a vicarious radiometric calibration system for single images. A multispectral camera (Mini-MCA 6, Tetracam Chatsworth, CA USA), operating with fixed exposure settings, was used to investigate low-cost calibration targets and methods. In this instance, vicarious calibration is defined as using ground based (though man-made) targets with known (measured) reflectance to create the calibration equation that relates DN to reflectance. The calibration was only applied to individual images which had calibration targets present. Selected target areas inside each calibrated image were then compared to the measured reflectance, and a low error (~2%) was determined [49]. Iqbal et al. investigated a simplified calibration system for UAV images using five calibration targets that were placed in the field along with 20 pseudo targets, which in this context referred to targets with unknown Lambertian properties. A multispectral camera (Mini-MCA 6, Tetracam Chatsworth, CA USA), operating with fixed exposure settings, was flown on a multi-rotor UAV at solar noon. Each image had a pseudo target visible, and each image was calibrated individually. A simple linear relationship was found between the measured reflectance of the calibration targets and the DN from the images. Each target appeared in several images; to improve the calibration the DNs were collected from all images with the same target and used in creating the calibration equation. R^2 values from 0.97 to 0.99 were found for the camera's six spectral bands. The root mean square error (RMSE) values across all bands ranged from 2.5 to 6.3% reflectance [50]. The authors did not test the system over multiple flight days, so there is no indication of temporal stability of the calibrated measurements. The calibration methods put forth in [48], [49], and [50] all require a calibration target in each image. For large research fields or commercial agriculture, using a calibration target in each image would commonly require hundreds of targets and would be an impractical use of time and money.

Mafanya et al. investigated a calibration method for large-scale mapping at high resolution. The calibration procedure used six gray-scale Masonite boards for calibration with four gray targets at 20%, 40%, 60% and 80% reflectance, as well as a white and black target for high and low reflectance. The calibration targets were placed at a single location covered by the flight. Red, green, blue, black and white PVC boards were placed near the calibration targets, and the reflectance of each PVC board was measured with a spectroradiometer. These colored PVC boards served as assessment targets for calibration based on the gray-scale boards. An RGB camera (Sony Nex-7, Sony, Minato

City, Tokyo Japan) was flown on a custom built fixed-wing UAV at 160 m AGL. The simplified ELM, using a log transformation to create a linear relationship between DN and reflectance with a single calibration target in each image, put forth in [48] was used for radiometric calibration in this work. The measured reflectance of the five color targets was compared to the estimated reflectance from the UAV mosaic in each band, and the resulting regression line had an R=0.97. The RMSE values were 4%, 4%, and 8% reflectance for red, green and blue respectively, and the student's T-test showed no statistical difference between the mean DN of the assessment targets across the mosaic. By only placing the calibration targets in a single part of the survey area and then using information from that area post-mosaicking, the authors demonstrated that calibration points do not need to be in each image to generate consistent error across the mosaic [51].

Laliberte et.al. investigated an image processing method for radiometric correction of images from a 6-band multispectral camera (Mini-MCA 6, Tetracam Chatsworth, CA USA) and an RGB camera (Canon SD 900, Canon, Ota City, Tokyo, Japan). Both cameras were operating with a fixed exposure and gain settings. Two ground-based calibration targets (2% and 85% reflectance) were used as reference targets. Two ways of applying the ELM were tested. One method involved taking the information from a single image and then applying the ELM to all images pre-mosaicking. The other method involved mosaicking un-calibrated images and then applying the ELM to the mosaic. Each method was compared with ground measurements made with a field spectroradiometer. Applying the calibration post mosaic across all six bands resulted in a

2.2% reflectance RMSE, while applying the calibration to each image pre-mosaic produced a 5.6% reflectance RMSE [52]. The authors do note that the sensor correction such as vignetting are performed during the mosaicking step, and that the order of calibration steps is important for reducing error.

As remote sensing has progressed through satellites and MAVs to UAVs, the method of calibrating the sensors during image acquisition has been investigated as each new platform and sensor have been placed in use. Past work shows that each image can be calibrated with in-field targets, resulting in low error, but it would be cumbersome and expensive to place targets in each UAV-based image for production farming. ELM has been shown to work well in many instances where ground-based targets are used with fixed sensor settings, and when the sensor is known to have a generally linear response. As UAVs become more common, and sensors are being designed specifically for UAV platforms, auto exposure camera settings are being commonly used because they are easier and faster to set up. As these systems and operating methods gain traction, they need to be tested to understand the sensor and acquisition method's impact on the accuracy of the data. By extension the agronomic decisions that are being made with the data depend on such testing. Thus far little consideration and research have been published on the impact of auto exposure systems on radiometric calibration of UAV image mosaics.

It is hypothesized in this work that using a sensor with fixed exposure settings and ground-based reference targets for post-mosaic calibration will generate smaller errors when compared to a sensor with automatically adjusted exposure settings and single-panel pre-flight calibration image. Thus, the objective of this research was to collect UAV-based remote-sensing images with both methods and then compare both data sets to a single MAV image calibrated with the standard ELM, which was intended to serve as ground truth.

2.2. Material and Methods

2.2.1. Site Description

Flights were conducted between mid-August and late November of 2017 and involved two field locations at the Texas A&M AgriLife Research farm near College Station, Texas. Field 1 was a long and narrow field with rows running along the short side and total area of approximately 12.1 ha (figure 2-1A). It was bordered on one short side and one long side by perennial grass and row crops on the other two sides. It was broken up into several plots with row crops of soybeans, corn, wheat, and a weed research plot. Field 2 covered a 31.5 ha area, with a perennial grass border on all sides (figure 2-1B). It was planted mainly in cotton, with a small strip of energy sorghum approximately 100 ft long by 10 rows wide. Field 2 also had a center-pivot irrigation system that traversed it, and the field covered approximately 1/3 of the pivot circle. The cotton, soybeans, and winter wheat were all harvested at typical dates for central Texas (cotton, August; soybeans, September; winter wheat, June), but the corn was part of the weed study and was not removed until mid-November. After harvest each plot was tilled under and left as bare soil. The land cover changed from predominantly row crops to predominantly bare soil through the course of this experiment. The use of two fields over the course of several months enabled the study to include broad variability in land cover and range of reflectances. This factor was important in the comparison of calibration methods for UAV remote sensing.

Figure 2-1: A) Field #1 was long and narrow covering 12.1 ha with mixed land cover of crops, soil and weed research plots. B) Field #2 was 31.5 ha planted in cotton, and had approximately 1/3 of a center pivot irrigation system.

2.2.2. Equipment Description

A single RedEdge camera (Micasense, Seattle WA, USA; figure 2-2) was used for both UAV and MAV flights. It is a five-band multispectral sensor with discrete bands in the blue, green, red, red edge, and NIR spectral regions (table 2-1) and has a downwelling radiation sensor that allows the sensor to gather information about ambient light conditions. The RedEdge camera allows for two different exposure setting modes. The default mode is autoexposure, which adjusts the exposure time and gain settings for each band independently in real time. The second mode is fixed exposure, in which the user chooses from 15 exposure time settings and four gain settings, with each band being set independently.

Figure 2-2: The Micasense RedEdge camera used for both unmanned aerial vehicle and manned aerial vehicle flights

Table 2-1: Micasense RedEdge band information with band width reported as full width at half maximum

Band	Center Wavelength (nm)	Band Width (nm)
Blue	475	20
Green	560	20
Red	668	10
Red edge	717	10
NIR	840	40

A Cessna 206 (Textron Aviation, Wichita, KS, USA) was flown by the USDA Agricultural Research Service (USDA-ARS) Aerial Application Technology Research Unit as the MAV for this research. A Tuffwing mapper UAV (Tuffwing, Boerne, TX, USA; figure 2-3) was used for all UAV flights. It is a fixed wing UAV with a wingspan of 1.2 m and takeoff weight of 2.2 kg fully loaded. This UAV uses a Pixhawk on-board flight controller, and Mission Planner (Ardupilot, Canberra Australia) was used for the mission planning software. The RedEdge camera was mounted in the downward facing sensor port in the bodies of the UAV and MAV.

Figure 2-3: Tuffwing unmanned aerial vehicle flights. The orange panel can be removed to access the sensor payload.

Geographic registration is important for mosaicking images properly so that locations within mosaics can be accurately compared between image-collection methods and between flights. Ground control points (GCPs) served as geographic registration points for both UAV and MAV, and the particular GCPs used also served as radiometric calibration points for the fixed exposure UAV flights. The GCPs had two levels, one at 0.92 m above the ground and the other at 1.83 m (figure 2-4). Each level of a GCP had three radiometric targets painted dark gray, medium gray, and light gray, along with a lid to protect the tiles from the weather and sunlight when not in use. The radiometric targets had dimensions of 60.9 x 60.9 x 0.64 cm, were constructed from recycled rubber, and had a reflectance of approximately 6%, 25%, and 50%, respectively. For geographic registration a Trimble R7 (Sunnyvale, CA, USA) GPS base station was used along with a Trimble R8 rover, and post-processing kinematic correction was performed on the data after field collection. This GPS system and method results in position data with an accuracy of ±2 cm in the x, y plane.

Figure 2-4: The ground control points were constructed with two levels, with radiometric targets placed on both the top and the bottom. The gps information was collected from the front corners of the lower deck.

Four radiometric calibration tarps (Group 8 technology, Provo UT, USA) measuring 8 m x 8 m were also placed in the field prior to each flight for calibration of the MAV data. These tarps had reflectance of approximately 6%, 15%, 25%, and 40% (figure 2-5).

Figure 2-5: Aerial calibration tarps used in radiometric calibration of manned aircraft images

2.2.3. Data Collection

Flight missions and associated data collection were conducted on August 18, October 6, October 25, and November 30, 2017. Flights performed on dates 2 through 4 were on field 1, while the flight on the first date was conducted over field 2. Each day had a clear sky, and all flights were conducted in a time window of +/- 1.0 h of solar noon. On each flight day, two UAV flights with the two different exposure methods were conducted along with one MAV flight. The UAV was flown at 120 m AGL, producing a spatial resolution of approximately 7.6 cm. The MAV was flown at 1310 m AGL, giving 0.90 m spatial resolution, allowing the entire field to be captured in a single image.

The autoexposure setting allows the camera to change the exposure time and sensor gain immediately before each image is acquired based on incident light being reflected from the scene. The reflected light can change drastically from image to image depending on the dominant ground cover in the scene, so the exposure and gain can change drastically as well. The fixed exposure mode involves setting the exposure time and sensor gain pre-flight and maintaining those settings constant for the duration of that flight. Twenty preliminary flight tests were conducted to determine exposure settings for the fixed exposure mode. The UAV was flown over the calibration targets (6%, 25%, and 50 % reflectance) at 120 m above ground level (AGL) on a cloud free day near solar noon. The gain and exposure settings were systematically changed for each flight, and the DNs associated with the dark gray, medium gray, and light gray calibration targets were determined. The settings that maximized the dynamic range – i.e., the difference in

DNs between dark and light targets – without zeroing or saturating any pixels of interest were selected for each band. Based on these preliminary tests, exposure time settings of 0.44, 0.44, 0.44, 0.44, and 1.00 ms, and gain settings of 1x, 1x, 2x, 2x, and 2x, were selected for the Blue, Green, Red, Red edge and NIR bands, respectively. For the MAV flights, the camera had fixed exposure settings of 0.33 ms for all bands and a gain of 1x. These settings were based on the experience of the USDA-ARS flight crew in using this sensor on a manned aircraft traveling at comparable AGL and speeds to those used in this experiment. These preliminary tests were also used to determine if the response curve for the RedEdge camera was linear, and thus if the ELM was an acceptable equation for calibration.

The GCPs were placed in the field at the beginning of the growing season in April 2017 and secured in place with four metal posts per GCP until the end of the season. Eight GCPs were placed in Field 1, with one at each corner and two spaced evenly along the long edge of the field. Nine GCPs were placed in Field 2 and spaced fairly evenly around the perimeter but out of the way of the center-pivot irrigation system. For georeferencing, the GPS base station was placed at a previously surveyed point that had been established by setting up the base station to record position for 24 hr. To collect position data for the GCPs, the rover was placed on the front left and front right corners of the lower deck on each GCP.

On all four flight days the MAV was flown first, and the radiometric target data collection was usually started while this flight was being performed. After the MAV flight was finished, the RedEdge camera was removed and mounted on the UAV and the autoexposure flight was launched. After the autoexposure mission ended, fixed-exposure settings were set on the camera and the fixed-exposure flight was launched. Each UAV flight lasted approximately 20 minutes. This protocol allowed the completion of all three flights of the same field inside the 2 hr flight window centered on solar noon. At approximately the same time the MAV flight was beginning, a spectroradiometer (PSR+ 3500, Spectral Evolution, Lawrence, MA, USA) was used to collect ground truth measurements of the MAV calibration tarps and the UAV calibration targets. The PSR+ 3500 has an active sensor and shields the object it is scanning, making it insensitive to solar illumination, and it provides data output in reflectance. Each calibration target was measured at five points spread across the surface. The five readings of each target were then averaged to generate its final reflectance value for the given flight. During the flights on 10/25 and 11/30, ground based radiometric calibration readings were collected on all reflectance calibration targets with the spectroradiometer. For flight day 08/18, the target measurements were collected on 08/16. The measurements for 10/06 were not collected on a day close to the fight; instead the data for this flight day were interpolated from data collected on 6/06, 10/25 and 11/30, assuming that any reflectance changes over this period would be linear.

2.2.4. Image Pre-processing

Physical parameters of the RedEdge camera as reported by the manufacturer were stored as metadata in the image files and later used in image processing to provide corrections for dark current and vignetting. To generate the relationships between DNs and reflectance for the whole-field MAV image, the empirical line method (ELM) based on the spectroradiometer data from the four calibration tarps was used in ENVI software (Boulder, CO, USA). After calibration, the image was loaded into ARCGIS 10.2 software (Redlands, CA, USA) for geo-referencing, which was performed by locating the GCPs in the image and applying the measured GPS coordinates to the appropriate corners of each GCP in the image.

For the autoexposure UAV flights, the camera manufacturer's recommended methods were followed to generate a reflectance mosaic. This method includes using a single white calibration panel of 15 x 15 cm provided by the camera manufacturer. An image of the calibration panel was taken pre and post-flight by holding the aircraft over the panel and manually triggering an image, while being careful about certain considerations like light direction so as not to induce shadows. The raw flight data were loaded into Pix4D software (Pix4D, Prilly, Switzerland) along with the images of the calibration panel, and the albedo value for each band. Since the downwelling radiation sensor was used for these flights, that option was selected during the program set up. Pix4D uses the metadata imbedded in the images to create a rough layout of the mosaic. The user then applies the GPS information to the images containing the GCPs. The software then completes the mosaic and the calibration. The output was a geo-rectified, calibrated reflectance map of the entire field in which each pixel value was reported as percent reflectance.

Images from the fixed-exposure flights were loaded into Photoscan software (Agisoft, St. Petersburg, Russia), which created an orthomosaic. The reflectance data collected from the calibration targets were loaded into a custom software program that performs radiometric calibration of the mosaicked image based on ELM. The calibrated mosaic was then loaded into ARCGIS to apply GPS-measured position data to the GCPs and create a geo-rectified, calibrated reflectance map of the entire field. The reason for using a different mosaicking process with fixed-exposure images is twofold. First, Pix4D was the program recommended by the camera manufacturer to handle the changing exposures generated by the autoexposure setting, so Pix4D had to be used for the autoexposure images. On the other hand, Photoscan offers more control over image-processing procedures such as color smoothing, which was not desirable with the fixed-exposure images. Thus, Photoscan was more appropriate for the fixed-exposure data. Any differences in reflectance strictly attributable to the difference in software and processes used to create the orthomosaic were expected to be negligible.

2.2.5. Data Analysis

While the data were being evaluated it was observed that the red edge and NIR bands had unexpectedly large errors relative to the other bands regardless of exposure method. Several possible contributing factors to the large errors in the red edge and NIR were explored, including temperature during the flights, ground cover classification, mosaic quality problems such as stitching artifacts, and raw image quality problems such as pixel noise or image blurring.

Image reflectance data from the two UAV remote-sensing calibration methods were compared on each flight date and across flight dates in three ways: 1) band-by-band comparison across 31 areas of interest (AOIs) relative to “ground truth” (i.e., the single calibrated image captured from the MAV); 2) band-by-band comparison relative to the ground-based spectroradiometer measurements of the four radiometric calibration tarps placed in each field during the flight missions; and 3) by the spectral index, visible atmospherically resistant index (VARI), across the 31 AOIs relative to ground truth (i.e., the MAV VARI).

To extract pixel-level data from commonly located AOIs, the 40 reflectance mosaics (four image dates, two exposure methods, and five spectral bands) and 20 MAV reflectance images (four image dates and five spectral bands) were processed with custom code written in R. The code retrieved pixel reflectance values from 31 AOIs (figure 2-6) defined by a set of coordinates in the image space. These AOIs were selected with a stratified random sampling technique based on knowledge of each field so as to span the reflectance range and ensure each AOI was as homogeneous as possible. Each AOI used for the band to band comparison was approximately 10 m x 10 m, with the mean pixel value of each AOI being calculated by the R code. The AOIs allowed comparison of reflectance at the same position in the UAV mosaics and the MAV images as well as comparisons of the same area across dates.

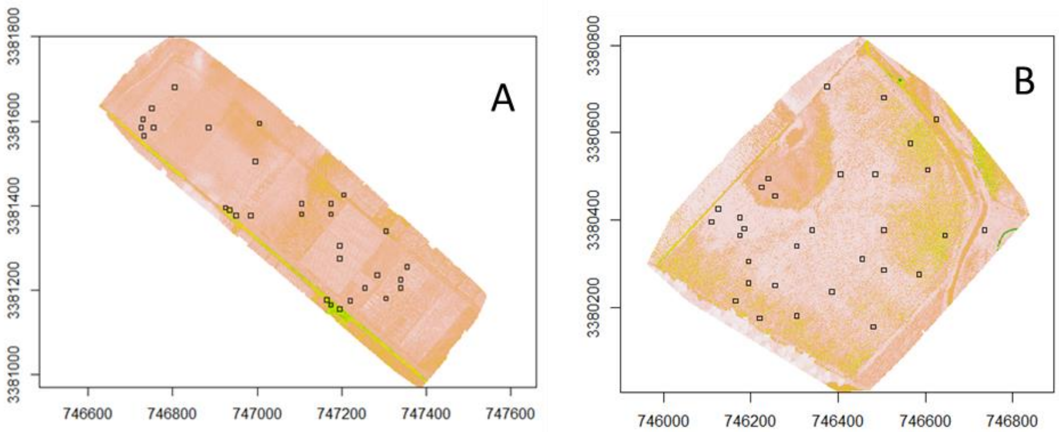

Figure 2-6: 31 area of interest (AOI) locations across the field used for comparing unmanned aerial vehicle and manned aerial vehicle images. The AOI's are laid out using coordinates in the x-y plane to insure the same geographical location is being compared across images. A) Field 1 used for flights on 10/06/2017, 10/25/2017, and 11/30/2017. B) field #2 was used for the flight 08/18/2017.

For the first comparison, plots of the mean UAV reflectances for each AOI vs. the mean MAV reflectances for each corresponding AOI were constructed for comparison of each band on each date and spanning all dates. Regression lines were determined and coefficients of determination (R^2) and root mean square error (RMSE) calculated. The closer the UAV data matched the MAV data, which was considered ground truth, the more accurate the method was considered. A perfect match would follow a 1:1 line, thus the RMSE of the data from each method was calculated with respect to the 1:1 line. A paired T-test was also conducted to compare the mean differences of the residuals between the UAV calibration methods. The null hypothesis of the paired T-test was that the means of autoexposure residuals and fixed-exposure residuals for the population of AOIs were not significantly different. Thus, if the null hypothesis could be rejected, the two calibration methods could be said to have different levels of accuracy.

For the second comparison, mean pixel reflectance values from the calibrated UAV mosaics were compared to the known reflectance values (as measured with the spectroradiometer) for the four calibration tarps (figure 2-4). As mentioned previously, these tarps had been used to calibrate the MAV data, but they were not used to calibrate the UAV data. The RMSE and bias relative to the 1:1 line were calculated for both UAV calibration methods.

For the third comparison, VARI was calculated from the mean RGB pixel values for each of the 31 AOIs based on the following equation.

$$VARI = \frac{Green - Red}{Green + Red - Blue} \qquad \text{Equation 1}$$

The mean AOI reflectance values in each of these bands was used in place of the corresponding pixel-level variables in the equation. The VARI for each UAV calibration method was then plotted against VARI for the MAV, and the RMSE was calculated. This comparison enabled a better understanding of how reflectance error would affect a common spectral index like VARI, considered to be a real-world application method for this type of data.

As mentioned previously, most users of agricultural remote-sensing data use vegetative indices as principal metrics in their decision-making processes, so the difference in reflectance error between autoexposure and fixed exposure is important not just in a theoretical sense but also in a practical sense. Vegetative indices are most often used in a local context, and it is thus difficult to use values of one field to aid in decisions for a field 20 km down the road, for example [53]. These vegetative indices are classified into management zones based on the available management methods, with different management zones being created for the application of inputs like nutrients, irrigation water, and pesticides. This process is well described in [54], where NDVI maps were broken into four classifications or zones for cotton plants and four more for all non-cotton regions of a 218 ha of field.

To demonstrate the effect that each calibration method's error would have in practical usage such as with the application of vegetative indices, we created a simulation that mirrors actual field usage that was reported in the literature and commercialized as a means of applying insecticide to a cotton crop at appropriate variable rates to control the insect, tarnished plant bug [54] [55]. In those studies, NDVI was used as a means to classify a field according to vigor level. The insects tend to thrive in high-vigor field areas, so it was assumed in our simulation that the full rate of insecticide would be applied in high-vigor areas, half rate in medium-vigor areas, and zero insecticide in low-vigor areas. For this simulation VARI was used instead of NDVI due to the limitations of the data collected. Each data point represents an arbitrary size in the field, which in the real world would be matched to the spatial resolution of the variable rate spray system.

The accuracy of a simulated insecticide prescription maps based on the two different UAV image calibration methods was tested with a Monte Carlo simulation. In this simulation a ground truth vector was created for the red, green, and blue bands, with each band having 10,000 data points. Each vector was generated with the rnorm function in R (R: A Language and Environment for Statistical Computing, R Foundation for Statistical Computing, Vienna, Austria), which creates a vector of random numbers such that the values of the vector fit a normal distribution with a specified mean and standard deviation. In this case the mean and standard deviation were set to match those measured by the MAV (Table 2-2).

Table 2-2: The manned aerial vehicle mean value and standard deviation for the blue, green and red bands which were then used in the Monte Carlo simulation for creating the ground truth simulation data.

Manned Aerial Vehicle		
	Mean	SD
Blue	5.14	6.14
Green	8.60	7.88
Red	11.34	9.46

The same random number generator was used to generate two error vectors using the means of the residuals and the standard deviation of the residuals which is the RMSE for the fixed exposure and autoexposure methods (table 2-3).

Table 2-3: The mean of the residuals from the unmanned aerial vehicle autoexposure and fixed exposure systems along with the root means squared error values. These values were used to create the Monte Carlo simulation error data for each exposure method.

	Autoexposure		Fixed exposure	
	Mean of residual	RMSE	Mean of residuals	RMSE
Blue	-2	2.6	0.52	1.7
Green	-2.6	3.3	0.09	1.8
Red	-3.59	4.5	1.29	2.5

The ground truth vector and error vectors were combined to create two simulated data sets, one for each calibration method, of values in the RGB bands. These data were then used to calculate VARI for the ground truth, autoexposure and fixed exposure. The ground truth, autoexposure and fixed exposure VARI data were then classified into three management zones, and comparisons were made between the MAV classification and the auto exposure and fixed exposure classifications, with the percent correct classification being reported. This simulation was conducted 10,000 times with varying randomized data, so the classification comparisons are based on 10,000 iterations of 10,000 data points.

When autoexposure is being used, the exposure time and gain setting for one image can conceivably be different for all adjacent images. The unique pairs of exposure and gain settings require unique equations to convert DNs to reflectance. These equations are calculated in Pix4D automatically based on the specific exposure time and gain settings and data from pre-flight calibration panel, the downwelling light sensor, and internal camera corrections (vignetting, dark current, etc.). The equations are applied to the raw image data during the orthomosaicking process. Furthermore, the tendency of autoexposure to change the exposure and gain settings from image to image calls into question how the data are initially digitized by the camera. The RedEdge camera used in this study has 16-bit (commonly 0 to 65,535) DN representation but actually uses a dynamic range for DN of 1 to 65520. An analysis of the exposure and gain variability with the autoexposure method was conducted to better understand how often the system changed the exposure and gain settings and the effect this had on the DN. The exposure time and gain were extracted from the metadata of each autoexposure raw image, and a bubble plot was created for each band and flight date so that the overall variability could be observed. The number of times the system changed exposure and gain was also found for each band and flight date. Select raw images from two regions of field #1 were also used to compare the dynamic range of DNs between the autoexposure and fixed-exposure methods. Two images each were selected from flight days 10/06/2017 and

10/25/2017 that contained AOI #A (figure 2-7), and one image each was selected from flight days 10/06/2017 and 10/25/2017 that contained AOI #B (figure 2-8). For this dynamic range comparison, the two AOIs covered an area of 26 m x 66 m. These new AOIs were chosen to have consistent land cover of perennial grass, providing reflectance levels expected in agricultural crops, based on a knowledge of the field conditions at the time of flight. The mean, minimum, and maximum DNs for the AOIs were then determined and used to calculate the portion of the camera's dynamic range used by the autoexposure and fixed exposure methods. For agricultural surveys, it is ideal for the plant reflectance to occupy the largest portion of the dynamic range, because this provides for high spectral resolution in the region of interest and the greatest amount of information about small changes in plant reflectance, which may relate to various stresses. The exposure time and gain of the selected images were determined, and the DNs from AOI #A and AOI #B were collected. The DN range was calculated for both auto exposure and fixed calibration methods. The range of values from the AOI was divided by the possible dynamic range of the DNs to provide a percentage of the dynamic range related to green vegetation.

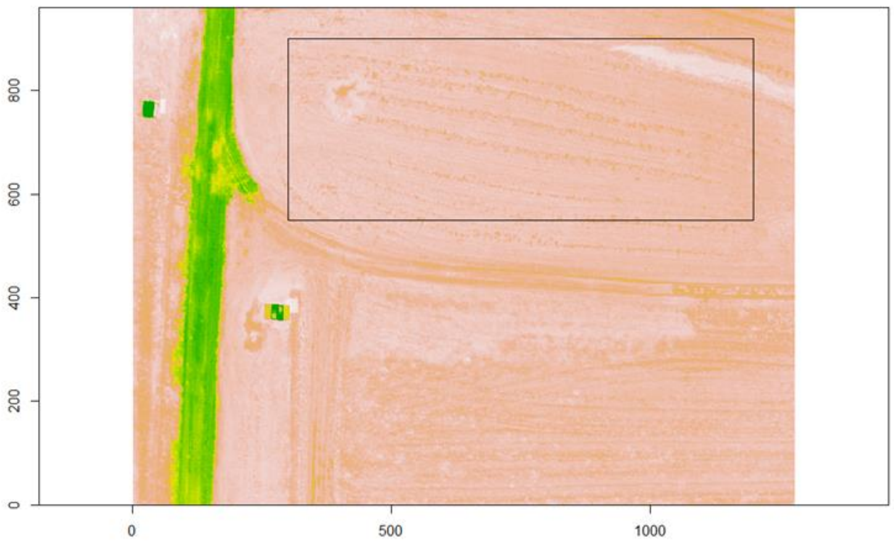

Figure 2-7: Raw image showing Area of Interest #A used to investigate the digital numbers of auto exposure. The black box shows the area of interest that the digital numbers were collected from.

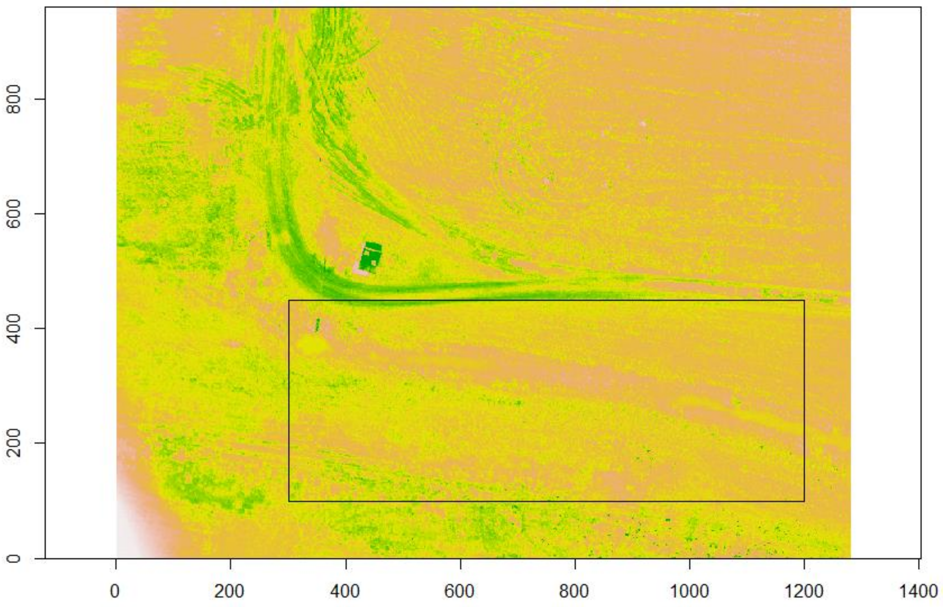

Figure 2-8: Area of Interest #B used to investigate the digital number dynamic range of autoexposure. The black box shows the area of interest that the digital numbers were collected from.

2.3. Results and Discussion

It is informative to consider how the reflectance in the field changed over time. From the first image on 08/18/2017 to the last image on 11/30/2017, the ground cover in the field moved from predominantly green vegetation to predominantly bare soil. This change was expected to have an impact on the reflectance being measured during a flight. Figure 2-9 includes six AOIs chosen from the MAV data that have land cover of perennial grass and are on the edge of both fields. The reflectance of each is plotted according to flight date. As the more reflective elements in the field (i.e. plants) are reduced in number and vigor throughout the season, the reflectance range became more compact and the values lower. The solar angle also changes from 72 degrees to 37 degrees between August and late November. The cumulated effect is a reduced reflectance range at the end of the season.

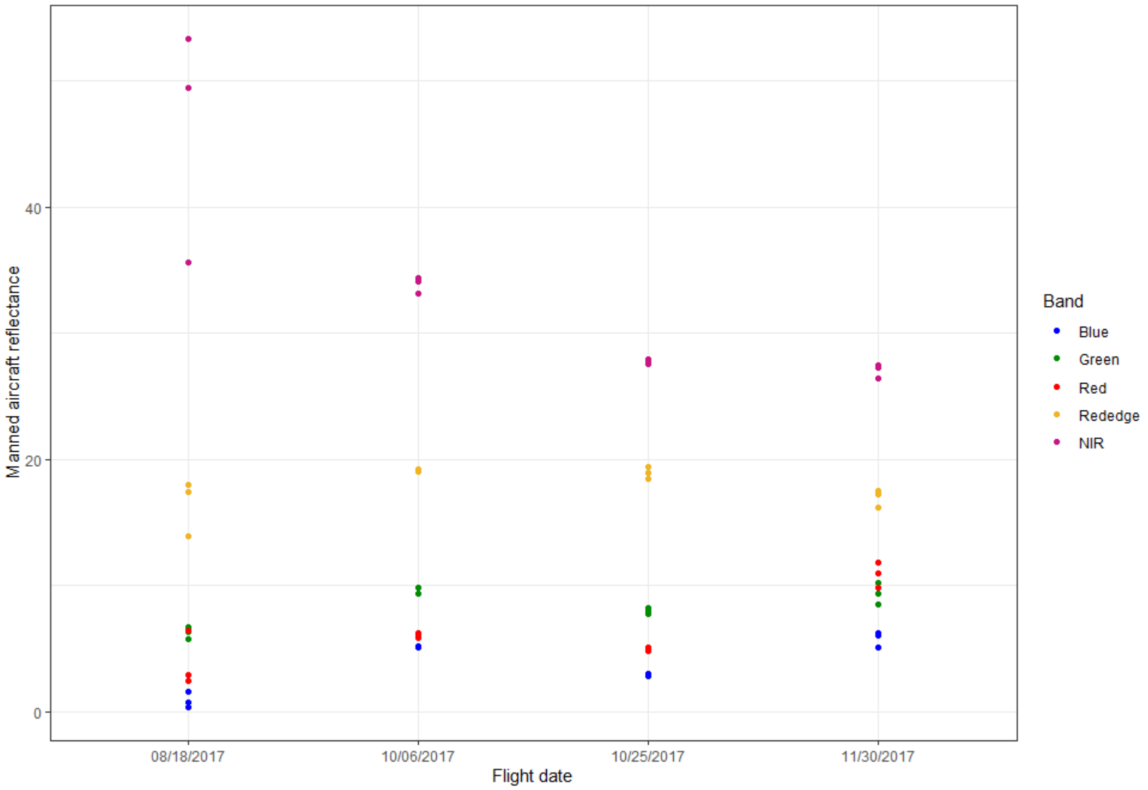

Figure 2-9: Reflectance from AOI's from the manned aerial vehicle system plotted against the flight data. This demonstrates the expected trend in reflectance as it progresses through time.

While performing the data analysis we found that the red edge and NIR bands displayed unexpectedly large error. To investigate where this error might originate, we plotted the reflectance residuals vs. ambient temperature in Celsius for both UAV calibration methods (figure 2-10). Autoexposure is shown in the left column and fixed exposure in the right, spectral bands are separated by row, and flight days are indicated by color. Trends for the autoexposure method were the same as for fixed exposure, and the spread of the residuals was also approximately the same on each flight date. A distinct increase in residuals as temperature increased would be expected if temperature were a significant contributing factor to error. While there is greater variation in residuals for the red edge and NIR bands, the residuals are flat or decreasing with increasing temperature, indicating that temperatures was likely not a major source of the error in the red edge and NIR bands.

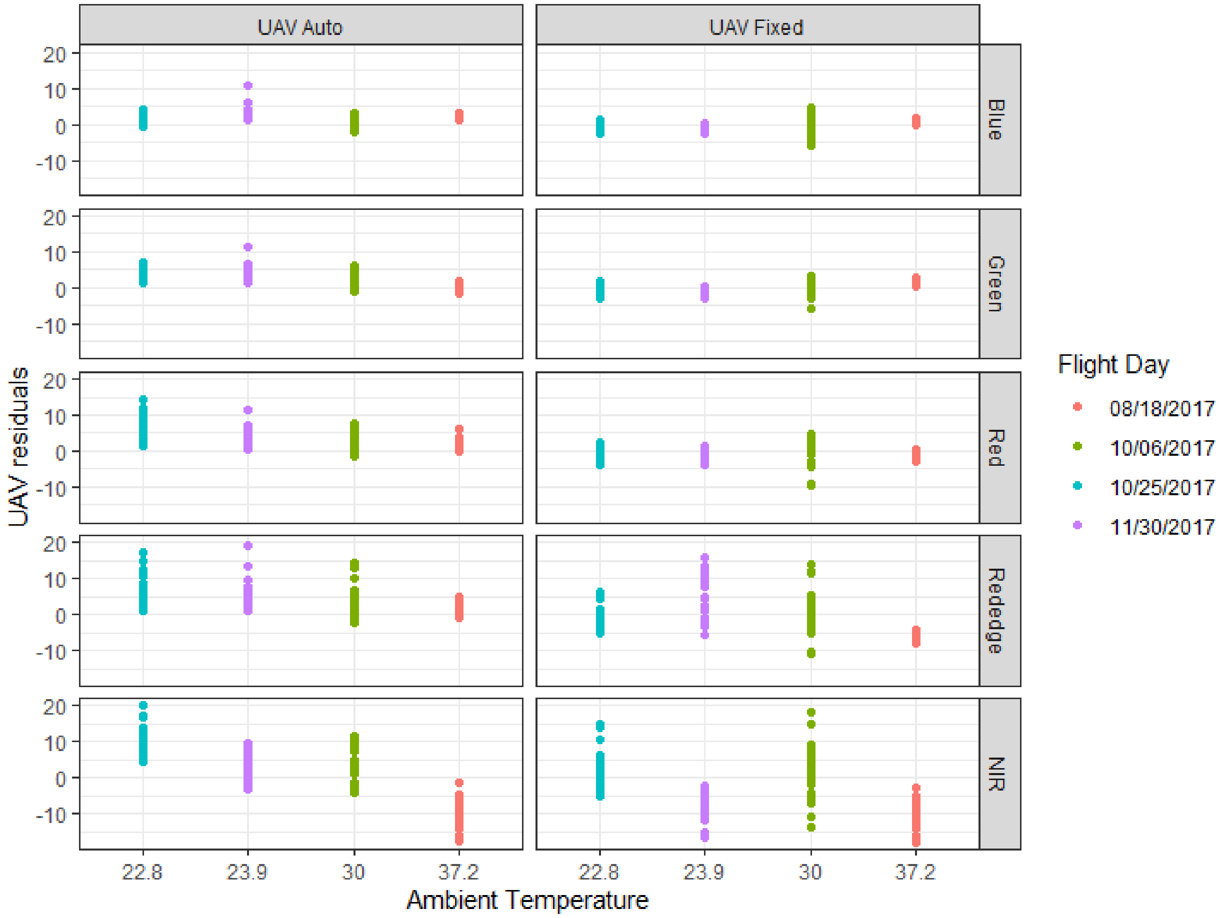

Figure 2-10: This is a graph of Temperature in Celsius vs. unmanned aerial vehicle residuals. The left column shows the Temperature vs residuals of the auto exposure system, and the right column shows the Temperature vs residuals of the fixed exposure system. Each row shows the bands, and color depicts the flight day.

Inspection of the red edge and NIR mosaics did not show any significant blurring or image artifacts. However, visual inspections of the raw images show some possible image speckling (figure 2-11) was present in all of the fixed exposure flights as well as the autoexposure flights on 08/18/2017, and 10/06/2017, but no noticeable speckling on

10/25/2017 or 11/30/2017. It is interesting to note that the speckling was present in the fixed exposure mosaics, but not present in the autoexposure mosaics (for flight days 08/18/2017 or 10/06/2017). During flights for other projects using the same equipment similar problems were noted, however the camera was destroyed during a hard landing making it impossible to have the sensor checked by the manufacture. The observation noted above suggests that the red edge and NIR detectors on the camera were not functioning properly at the time of the flights and led to a focus on the RGB data in this work.

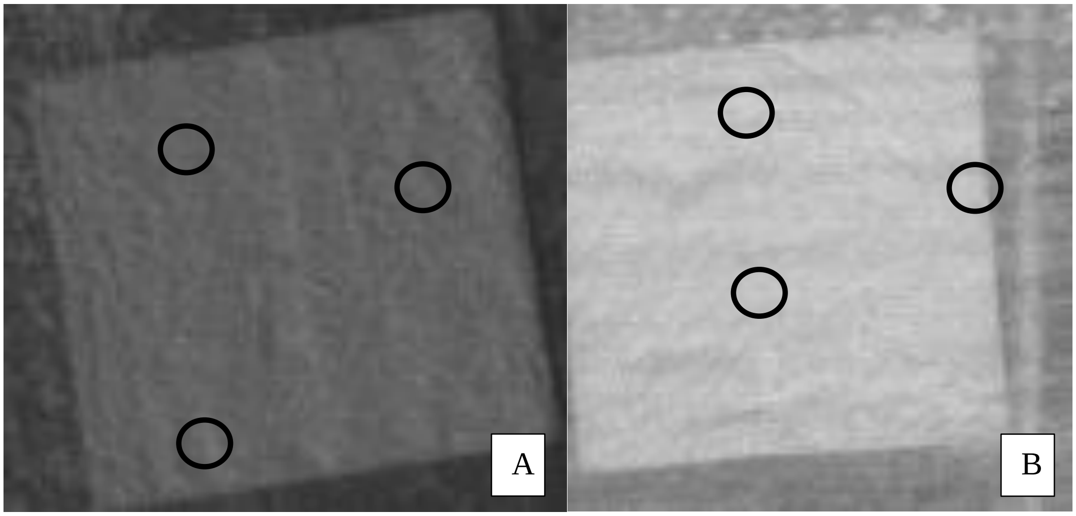

Figure 2-11: The raw images were visually inspected for noise. A) Shows the red edge band from a fixed exposure flight on 10/06/2017. B) Shows the near infrared band from autoexposure on flight day 08/18/2017. The black circles demonstrate positions of possible speckling noise which could be the cause of the unexpectedly high error in the red edge and near infrared bands.

Plots of UAV vs. MAV reflectance by band, flight day, exposure method, spectral band, and AOI type are shown in figure 2-12. Each flight day is shown as a different column, along with each band as a different row. The data point shape denotes UAV calibration method, while the color denotes AOI classification. The RGB bands have consistent groupings by AOI type along the 1:1 line, with the autoexposure method having slightly more scatter than fixed exposure. The RGB bands are also consistent across time, with similar scatter for a given calibration method and AOI classification. The red edge and NIR bands however have much more scatter about the 1:1 line, with little temporal consistency. The AOI types fall in different places as the season goes on for both red edge and NIR. For example, the crop and soil class had high NIR reflectance on 08/18/2017, but low NIR reflectance on 11/30/2017. Red edge and NIR reflectance of some AOI classes moved across the 1:1 line from one flight date to the next. This lack of consistency between flight days for red edge and NIR but not for RGB further suggests an error problem with the NIR and red edge data.

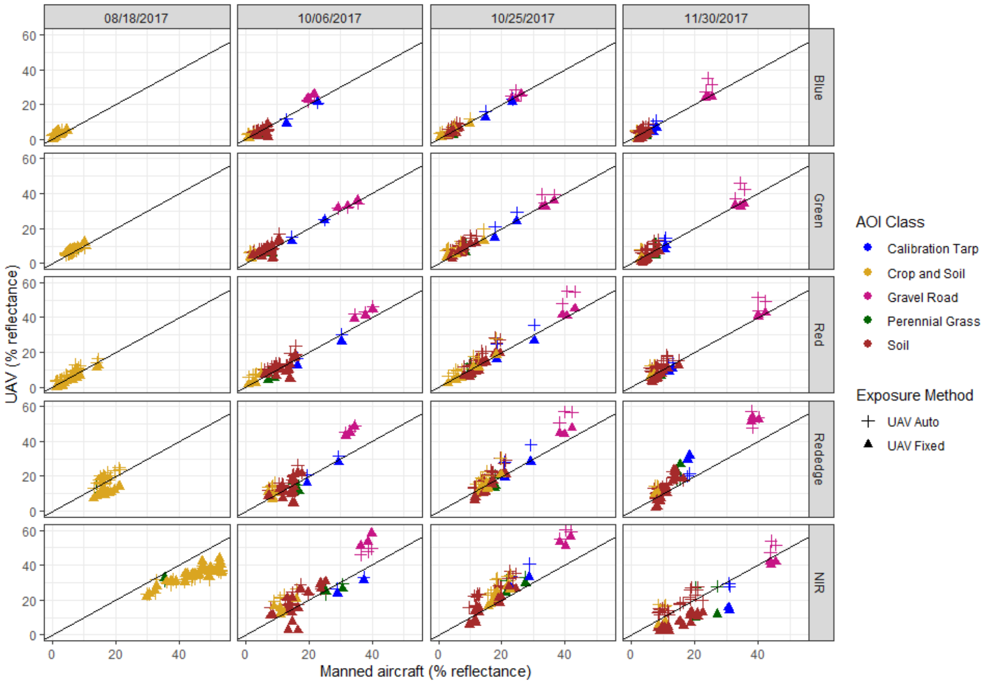

Figure 2-12: The unmanned aerial vehicle reflectance vs. the manned aerial vehicle reflectance with each column representing a flight day, while each row represents a specific spectral band. The color of the data points indicates the area of interest land cover classification and the data point shape indicates the exposure system used.

The band to band comparison of the AOIs between autoexposure and fixed exposure methods across all dates is shown in figure 2-13, where reflectance values from the two UAV calibration methods are plotted against reflectance values from the MAV image. The left column of plots represents autoexposure and the right represents fixed exposure, with each row corresponding to a different spectral band. The regression line plotted on each graph has a slope of one and an intercept of zero, marking where perfect agreement between UAV and MAV data would be. The shapes of the data points signify different flight days, while the colors indicate the different AOI types (e.g., soil or perennial grass) and therefore different expected reflectance. A clear trend can be seen in the RGB bands for both auto and fixed exposure methods. Autoexposure points are mostly above the 1:1 regression line, with increased scatter as the reflectance value increases. Autoexposure data also have more variance between flight days. The fixed exposure scatter is smaller and lies along the 1:1 line with little to no increase in variance at different reflectance values and across flight days. As mentioned previously, the red edge and NIR bands were observed to have unexpectedly large errors with both the autoexposure and fixed exposure methods. For both methods the error for the red edge (RMSE auto=5.75; fixed= 5.67) and NIR (RMSE auto=9.06; fixed=8.11) bands was roughly double that of RGB error (RMSE auto_{avg}=3.45; $\text{fixed}_{\text{avg}}$=1.97). Both the red edge and NIR bands also showed greater variability between flight days in terms of AOI classification reflectance compared to the RGB bands (figure 2-13).

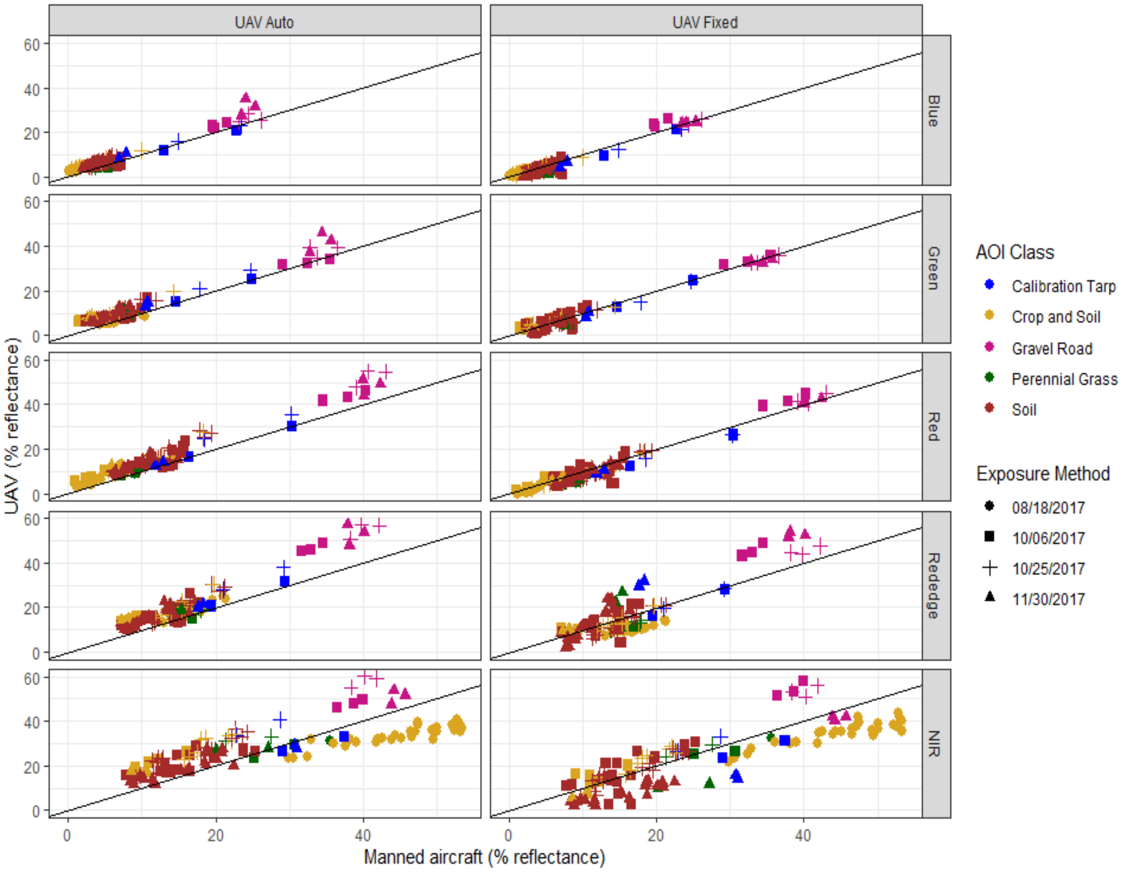

Figure 2-13: The unmanned aerial vehicle reflectance vs. the manned aerial vehicle reflectance for the auto exposure system (left column) and fixed exposure system (right column). Each row shows an individual band, while the data point shape indicates the flight day and the color indicates the type of ground cover for that area of interest.

The RMSE about the 1:1 line in figure 2-13 is given for each band across the four flight dates in table 2-4. For the RGB bands, the autoexposure RMSE was 2.6 to 4.5% reflectance, roughly twice as high when compared to the fixed exposure, which had RMSE of 1.7 to 2.5% reflectance. It is worth pointing out that the red edge and NIR RMSEs were almost double that of the RGB bands, and autoexposure had higher RMSE than fixed exposure for these two bands as well. High R^2 values (table 2-4) indicate that the relationship between reflectance data from both UAV calibration methods and reflectance data from the MAV was strongly linear across the reflectance range, indicating that ELM was a reasonable method to apply to the fixed exposure for converting DNs to reflectance. The paired T-test on the residuals of autoexposure and fixed exposure data showed a significant difference at the 0.01 confidence level (table 2-4), indicating that the RMSE differences in the band to band comparison are significant, establishing the clear superiority of the fixed exposure method in the RGB data accuracy.

Table 2-4: The RMSE of the UAV exposure systems to the 1:1 line. The R^2 values are for a linear regression of the unmanned aerial vehicle onto the manned aerial vehicle for each band. The paired T-test compares the auto and fixed exposures systems on an area of interest basis.

	RMSE		R^2		Paired T-test	
Band	Auto	Fixed	Auto	Fixed	P-value	Mean of the Difference
Blue	2.6	1.7	0.94	0.94	2.69×10^{-37}	2.58
Green	3.3	1.8	0.94	0.95	1.24×10^{-19}	2.70
Red	4.5	2.5	0.96	0.96	6.27×10^{-51}	4.88
Red edge	5.8	5.7	0.91	0.77	3.20×10^{-28}	5.17
NIR	9.1	8.1	0.61	0.72	1.38×10^{-17}	5.11

The comparison between autoexposure and fixed exposure of the calibration tarps for all flight dates is shown in figure 2-14. The UAV exposure method is shown by the shape and while the red, green, and blue bands are shown by the color of the data points. The regression line shown is the 1:1 line, showing where perfect agreement between the UAV and ground measurements would lie. The autoexposure tends to overestimate the reflectance of the calibration tarps and has more scatter compared to the fixed exposure for all three bands. The scatter for both exposure methods does increase as the reflectance values increase, and the reflectance values for the bands becomes more distinct. The RMSE of the auto exposure data was higher than that of the fixed exposure data with the difference ranging from 0.5 % reflectance to 2.5% reflectance (table 2-5), with the largest difference between the methods found in the red band. Table 2-5 also shows the bias relative to the 1:1 line for UAV reflectance vs. tarp reflectance. The bias for the autoexposure method was more than double the fixed exposure bias for each of the RGB bands. These results confirm the aforementioned results with the AOIs, which showed fixed exposure reflectance data to be more accurate than autoexposure data.

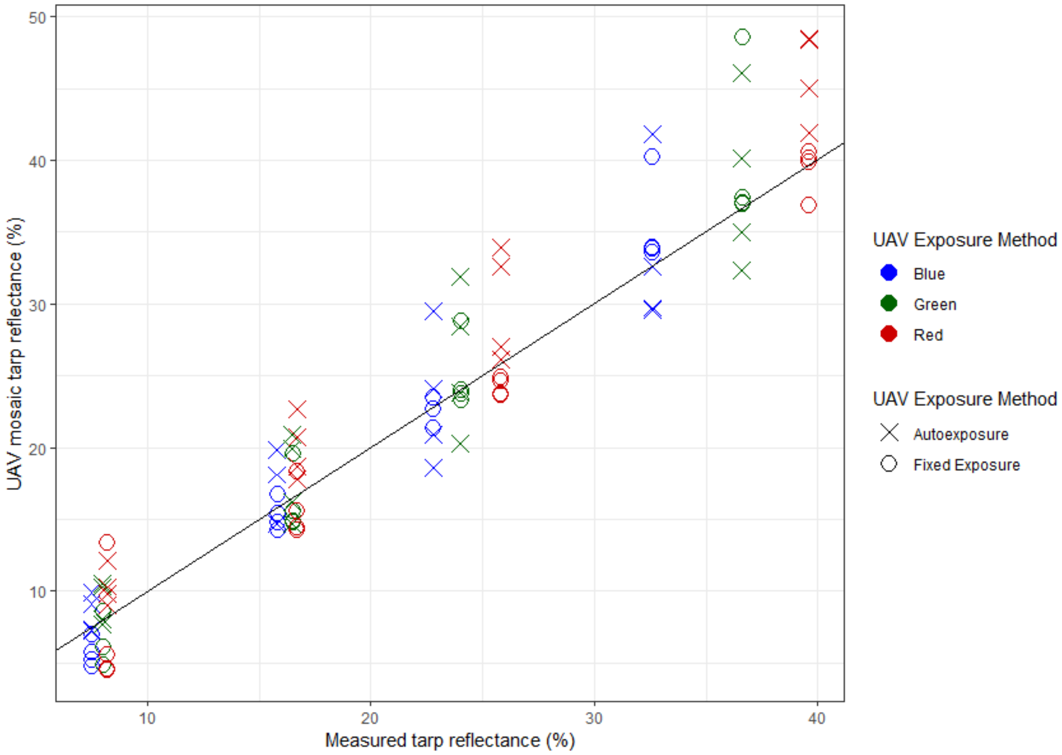

Figure 2-14: Reflectance for measured tarps reflectance plotted against the unmanned aerial vehicle mosaic tarps reflectance for RGB bands, for all four flight days.

Table 2-5: The RMSE and bias calculated from the comparison of the unmanned aerial vehicle mosaic reflectance and the measured tarp reflectance.

	Tarp RMSE to 1:1 line		Tarp Bias to 1:1 line	
Band	Auto Exposure (% reflectance)	Fixed Exposure (% reflectance)	Auto Exposure	Fixed Exposure
Blue	3.6	2.3	-0.80	-0.09
Green	4.1	3.6	-1.61	-0.56
Red	4.9	2.4	-3.96	0.98

The VARI spectral index comparison on the AOIs between autoexposure and fixed exposure methods across all dates is shown in figure 2-15. The auto exposure and fixed exposure methods are the left and right plots, respectively, while the shape and color of the points indicate the flight date, and the 1:1 line is shown to indicate the position where perfect agreement between UAV and MAV VARI would lie. VARI is a ratio of combined like variables, and as such it has no units and thus is reported simply as a number. The auto exposure data had greater scatter, and at the high end of index values, the error was very high. There also was a large amount of variation in the UAV vs. MAV VARI trends from one flight day to the next for the auto exposure method. The auto exposure method had a higher RMSE (0.44) than fixed exposure (RMSE = 0.23). Also, while the MAV data had a VARI range of -0.62 to 0.59, autoexposure had a much higher range (-0.66 to 2.79), and fixed exposure also had a higher range (-0.69 to 1.15) but more in line with the MAV data. These results indicate that when calculating a vegetative index from reflectance values, the error levels in the original data are important, and fixed exposure produces results with approximately half the error of autoexposure and is more consistent across flights. As mentioned previously, most users of agricultural remote-sensing data use vegetative indices as principal metrics in their decision-making processes, so the difference in reflectance error between autoexposure and fixed exposure is important not just in a theoretical sense but also in a practical sense.

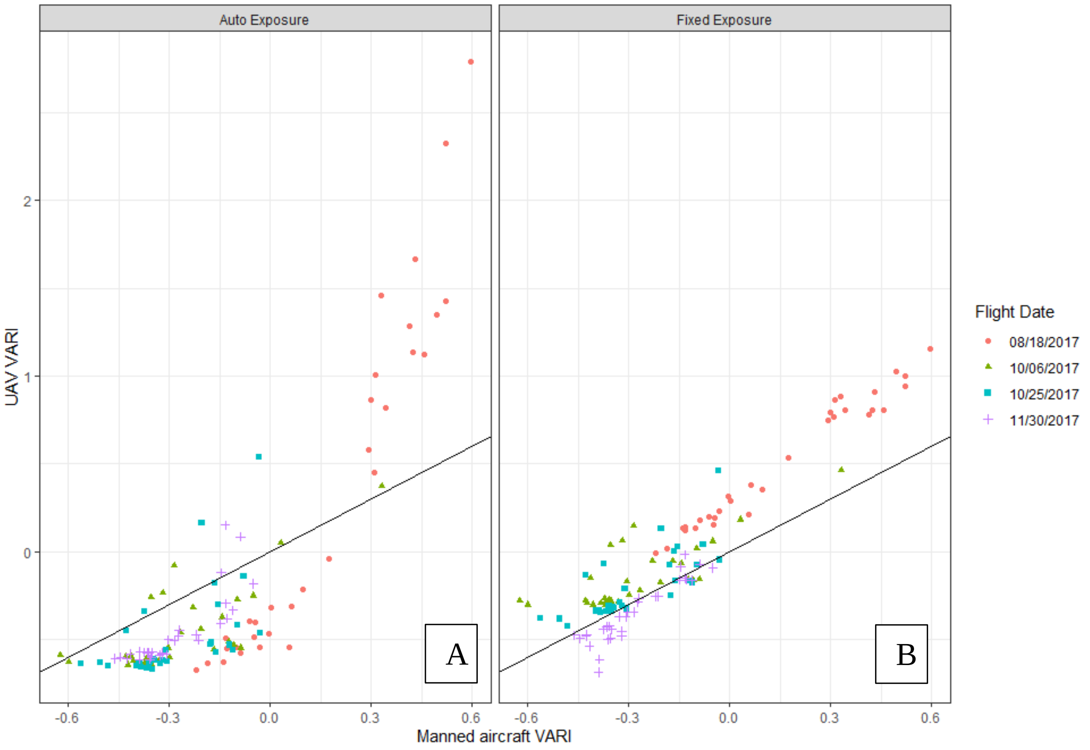

Figure 2-15: The Visible atmospheric resistance index (VARI) data for the unmanned aerial vehicle systems plotted against the VARI data from the manned aerial vehicle system. A) is the auto exposure system. B) Shows the fixed exposure system.

When the Monte Carlo simulation was conducted to compare the effects of reflectance error between the two calibration methods on classifications into three VARI classes, it was determined that the autoexposure method enabled correct classifications 67.7% of the time, while the fixed exposure method enabled correct classification 82.2% of the time. Essentially, the autoexposure method enabled 100% improvement in accuracy compared to a random guess, which would produce an accuracy of 33.3%. The fixed exposure method, on the other hand, enabled 147% improvement.

To visualized the difference between the impact of the autoexposure error and fixed exposure error, figures representing an agricultural field were created from the classification data, such that green represents correctly classified management zones and red represents misclassified zones due to the addition of the error (figure 2-16). The upper figure (A) shows results of the simulation based on autoexposure error, and the lower figure (B) shows results of the simulation based on fixed exposure error. The Monte Carlo simulation showed that if these zones were used to apply pesticide to cotton, the fixed exposure method would result in significantly higher revenue by enabling correct application of pesticide on 15% more of the field than the autoexposure method.

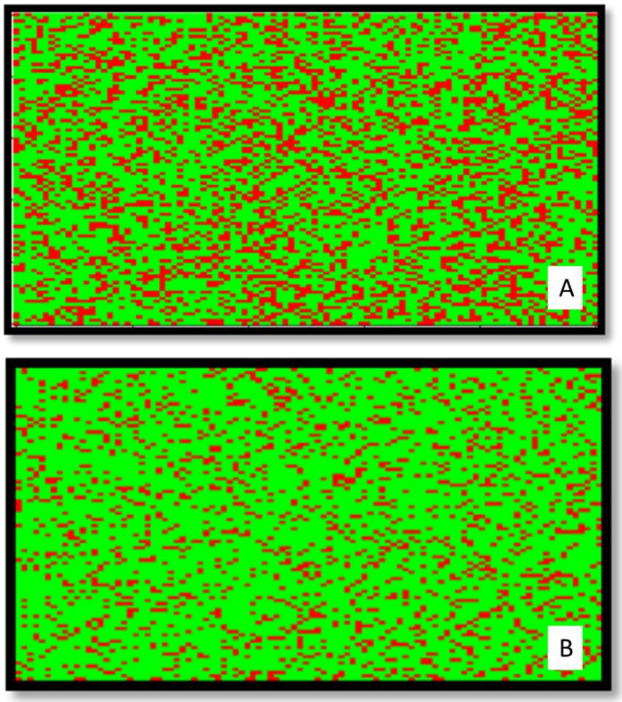

Figure 2-16**:** The Monte Carlo simulation is displayed graphically with the green squares representing a unit that is correctly classified and the red squares representing a unit that was mis-classified due to the presents of error. A) Shows the visible atmospheric resistance index (VARI) calculation when the error present in the autoexposure method is used, resulting in 67% correctly classified and 33% classified incorrectly. B) shows the VARI calculation using the fixed exposure error, showing 82 % correct classification and 18% classified incorrectly.

When exposure times and gain settings of the autoexposure method were considered, it was observed that exposure time changed often. The minimum number of times exposure time changed during a flight was 79 (red edge band, 10/06/2017), out of 268 images (table 2-6). The maximum number of times was 120 for the NIR band, which on Nov. 30 was almost half the number (267) of images collected. These numbers mean that between 29 and 44% of the images in any mosaic had a different exposure time than adjacent images.

Table 2-6: The number of times the auto exposure time changes for each flight by band.

Number of times exposure values change						
Flight day	Images per flight	Blue	Green	Red	Red edge	NIR
8/18/2017	346	104	104	104	82	64
10/6/2017	268	94	88	81	79	108
10/25/2017	394	115	91	80	83	120
11/30/2017	267	115	91	80	83	120

Table 2-7 shows the number of times the gain setting changed for each flight day and spectral band. The smallest number of changes was for the green band on 08/18/2017, with only 4 changes in 346 images. The largest number was 61 for the blue band on 11/30/2017. These numbers mean that between 1 and 22% of the images of a mosaic had a different gain setting than adjacent images.

Table 2-7: The number of times the gain settings for the auto exposure system change for each flight day on each band.

Number of times gain value changes in each set						
Flight day	Images per flight	Blue	Green	Red	Red edge	NIR
8/18/2017	346	48	4	40	38	22
10/6/2017	268	28	22	30	38	54
10/25/2017	394	50	22	35	37	62
11/30/2017	267	61	50	50	42	49

A bubble plot of exposure time vs. gain setting is given in figure 2-16. The size of each bubble indicates the number of individual exposure and gain pairs at that point. Each graph encompasses one flight day and one spectral band. Figure 2-16 includes two plots indicative of the extremes from the data set. Figure 2-16A shows the exposure and gain pairs from 10/06/2017, and it can be seen that the exposure range is roughly from 0.5 to 2.0 ms with two gain settings (1, 2). Figure 2-16B shows three gain settings (1,2,4) and exposure times of roughly 1.0 to 2.0 ms. This trend of increased gain values and exposure times is found throughout the data as the date moves from earlier in the season to later in the season. The reflectance decreases as the season progresses, and the exposure times and gain settings also increase as autoexposure appears to adjust for low reflectance in the field by increasing the sensitivity of the system, most likely to produce a visually pleasing image. Bubble plots for the rest of the flight days and bands can be seen in Appendix A.

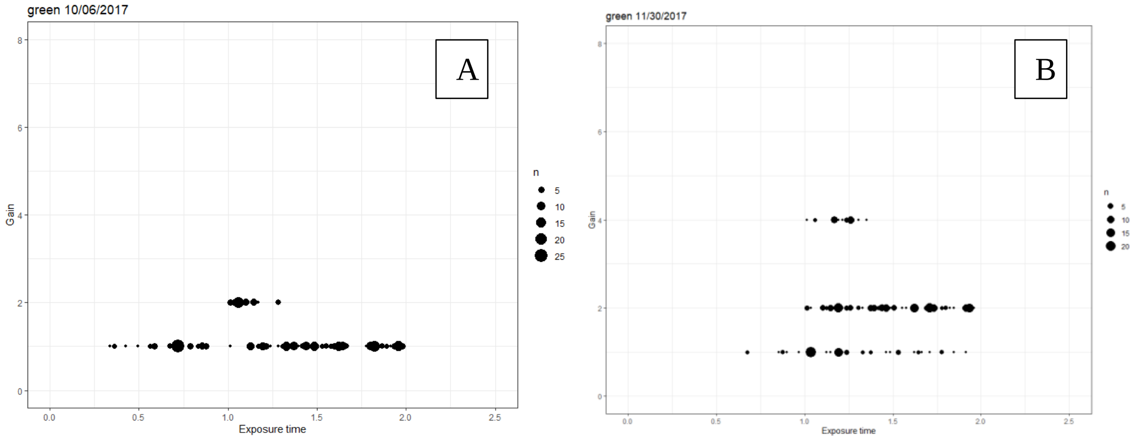

Figure 2-17: The bubble plot shows a distribution of exposure time and gain settings for the auto exposure system. The larger bubbles indicate more images sharing the same gain/exposure settings. A) Shows the bubble plot for the green band on 10/06/2017. B) Shows the bubble plot for the green band on 11/30/2017.

When the dynamic ranges of the autoexposure and fixed-exposure methods were compared with respect to green vegetation, the auto exposure DNs covered a larger percentage of available dynamic range than the fixed exposure DNs (table 2-8). The autoexposure DNs actually covered between 40 and 80% of the available dynamic range on average, while the fixed-exposure DNs covered between 10% and 40%. Because fixed exposure and autoexposure data were produced with the same camera, any digitization error should have been consistent on a per-DN basis across both systems. Since the autoexposure DNs covered a larger amount of the dynamic range, the autoexposure data should have had more precision in digitization of object reflectance. Yet the error was significantly greater with autoexposure, so it appears likely that the majority of the error in the autoexposure data was introduced in the conversion from DN to reflectance.

Table 2-8: The range of the DN for the chosen area of interest of perennial grass, shown as a percent of the dynamic range possible given the nature of the sensor.

	Auto Exposure System % of Dynamic Range					Fixed Exposure System % of Dynamic Range				
Image name	Blue	Green	Red	Red edge	NIR	Blue	Green	Red	Red edge	NIR
1_10062017	42.8	50.7	43.7	42.7	81.8	22.4	28.6	41.4	26.5	65.2
2_10062017	43.1	23.8	67.1	65.5	78.9	13.6	18.4	25.7	18.9	49.5
3_10062017	84.2	79.7	57.6	80.0	80.9	33.1	37.7	25.3	30.2	55.7
1_10252017	65.6	55.7	57.6	58.7	82.3	14.5	21.9	25.3	23.5	47.9
2_10252017	80.9	76.4	64.3	23.1	67.9	11.5	19.1	24.4	21.1	47.0
3_10252017	65.3	80.9	87.0	77.7	81.4	18.4	21.8	28.7	19.9	45.2

The difference in error between the calibration methods might have several sources. One possible source of error with the autoexposure method comes from how the calibration panel is used. The process involves a single high-reflectance target, which means the reflectance values and DN relationships must be extrapolated from that single point, likely resulting in more error than interpolating between a low and high point as was done with fixed exposure. The autoexposure method collects an image of the calibration target under relatively unstructured conditions at ground level pre-flight, while the images that are collected during the flight mission are collected at altitude (120 m AGL), meaning calibration is not performed under the same lighting circumstances as image collection during the mission, so parameters that are based on this calibration step likely have inherent error.

Furthermore, the fact that images can have many different exposure time and gain settings can potentially lead to two more sources of error. First, an additional mathematical step is required to relate the raw images parameters to the calibration image parameters before being converted from DN to reflectance. This relationship may be erroneous. Second, the actual exposure and gain achieved at different settings could be inconsistent or different than the setting values. Another possible source of the error with autoexposure is the order of the data processing operations. Because each image can have a different exposure and gain, the images must be calibrated before the mosaic can be constructed. Laliberte et al. showed that even when using fixed exposure, images calibrated pre-mosaic resulted in higher radiometric error [52].

Fixed exposure, by contrast, has in this case three calibration targets of low, medium, and high reflectance that span the majority of the reflectance range of interest. Allowing interpolation between points to generate the relationship between reflectance and DN likely results in a lesser error than extrapolation. Because the images all have the same parameter settings, the data processing order allows the mosaic to be constructed before the calibration step, again reducing error, as found by [52]. Once the mosaicking step has been completed the calibration equation can be applied to all areas of the image mosaic with a single calibration equation for each band.

2.4. Conclusions

While red edge and NIR data were not evaluated in detail in this study due to error issues with the camera, results with the RGB reflectance data from agricultural fields were conclusive and showed that calibrated UAV mosaics of images collected with fixed exposure typically produced approximately half the error produced by their auto exposure counterparts. The difference in error between the two methods is statistically significant at a confidence level of 0.01. The higher accuracy with fixed exposure was present when data were compared to AOIs with different land cover types and when compared to calibration tarps in the field. When the RGB bands were used to calculate the VARI index, the error in the VARI index was again found to be roughly twice as great in autoexposure as in fixed exposure. We demonstrate that the impact of this error on management decisions making is improved by 15% when the fixed exposure is used for 3 classification zones.

The source of the greater error associated with autoexposure is not completely clear, but it does not appear to be attributable to digitization error. More likely it is mainly a result of errors introduced in the conversion of DNs to reflectance. Autoexposure changes the image parameters often, requiring a different calibration equation for each unique set of image parameters. Because the image parameters are different the autoexposure method must be calibrated pre-mosaic, which has been shown in other work to increase the error. The autoexposure method also uses an image of a single calibration panel, which is collected with image parameters that are potentially different than the parameters found in the survey causing additional calculations, and because a single calibration point is used the DN to reflectance relationship must be extrapolate to estimate reflectance. The combination of these sources of error are most likely the main drivers in producing the larger error and the larger bias reported in this work. By comparison the fixed exposure method is calibrated post-mosaic requiring a single calibration equation for each band, and uses interpolation between a high and low calibration point, simplifying the process and reducing the error and the bias.

3. LOW-FIELD MAGNETIC RESONANCE IMAGING OF ROOTS IN INTACT CLAYEY AND SILTY SOILS*

3.1. Literature Review

Analysis of plant root system development and architecture in structured field soils is challenging. Technology that enables *in situ* root system measurement and analysis would improve our understanding of the development, architecture, and responses to environmental variation, and improve root models, breeding for ideal root structures, and management decisions that focus on carbon sequestration in soil [17] [16]. While many tools have been developed for laboratory-based measurements [56] [57] [58], no current technology is capable of in-field, *in situ* measurements of root systems across a variety of agricultural soils. This paper presents a proof-of-concept of a system capable of imaging plant roots *in situ* growing in agriculturally relevant soils.

The most common method for quantifying root systems is by excavation, washing and imaging the cleaned roots, often called “shovel-omics”. Trachsel et. al (2011) gives an example of this method, in which the roots are excavated and visual metrics are used to describe the roots in ways that advise plant breeding applications [59]. Newer methods that have varying adoptions by researchers include 2-D flatbed optical scanners [60], X-ray computed tomography [61], [62], [63], and magnetic resonance imaging

---

* Reprinted with permission from “Low-field magnetic resonance imaging of roots in intact clayey and silty soils” by Bagnall, G. C., Koonjoo, N., Altobelli, S.A., Conradi, M.S., Fikushima, E., Kuethe, D. O., Mullet,J. E., Neely, H., Rooney, W. L., Stupic, K., Weers, B., Zhu, B., Rosen, M. S., Morgan, C.L.S. 2020. Geoderma. 370, 114356, 2020 by G. Cody Bagnall.

(MRI) [64], [65], [66], [67]. Flatbed optical scanners are useful for imaging roots after removal of soil but are not suitable for *in situ* measurements. X-ray computed tomography is a high-resolution technique that is useful in a laboratory setting, but safe field deployment is difficult. Several researchers have used MRI in laboratory settings to image plant root architecture in re-packed soil and engineered potting media and soil mixes. Laboratory based plant root system morphometric analysis is useful; however, these systems do not accurately reflect the root system architectures found in field soils [16].

Magnetic resonance imaging can be categorized based on the magnetic field strength operational range, with high field MRI (HF-MRI) typically performed in the range of 1-10 T (Tesla) and low field MRI (LF-MRI) operating below 1 T. The source of the signal in the MRI experiment in both cases is nuclear magnetic resonance (NMR) inductive detection of precessing nuclear magnetic moments in a magnetic field. Spatial encoding is obtained by phase and frequency modulating the detected signal using the application of magnetic gradient fields to the system. Systems of precessing nuclear magnetic moments can be characterized by their NMR properties. In particular, the time for spin systems to revert to their thermal equilibrium polarization is known as the spin lattice relaxation time (T_1) and the time for precsssing magnetization to become dephased is the spin-spin relaxation time (T_2). In MRI, time constants T_1 and T_2 can be used to provide image contrast, and differences in these values allow a target material to be separated from the background material surrounding the desired target [68].

Magnetic resonance imaging, as performed in this work, images ^{1}H nuclear spins which in the case of soil and roots, are found in the form of water. The amount of water that is found in soil changes with the amount of silicate clay in the soil matrix as well as the relative soil moisture content. Soil water has been found to have short T_2 relaxation times [68], and is dependent on soil type [68], [69]. The soil-dependent T_1 and T_2 influence the imaging strategy which requires the relaxation time to be measured for each soil [70]. In the case of root imaging in soil, the greater the difference between the soil water relaxation time and the root water relaxation time, the easier it is to distinguish roots from soil.

To differentiate between soil water and water located in the roots, we need to understand the relaxation times of each. Rogers and Bottomley (1987) discovered a clear distinction between soil water and root water relaxation times and conclude that soil texture and water potential need to be considered for future use of MRI systems in soils-based research. In that work, fava beans were grown in eight natural soils with a range of clay contents, and eight potting media. The samples were placed in a 1.5 T field to measure soil water and for root imaging. Natural soils with more than 4% paramagnetic material did not produce usable images at 1.5 T. The images produced from soils with less than 4% paramagnetic material, such as some of the manufactured potting media and some of the natural soils, produced mixed results with some generating clear root images and others, such as the Houston Black clay, producing distorted images [71]. Since most soils are described in terms of soil texture instead of paramagnetic content, Pflugfelder et.al. (2017) used some of the findings from Rogers and Bottomley to test six soils and two manufactured media for MRI suitability. The study was conducted at 4.7 T, while also making note of the water holding capacity, soil texture, and ferromagnetic particle content for each soil. Two of the four soils tested had high ferromagnetic particle concentrations (11.7 and 25.3%) and also had the highest clay content (~ 25% and 45%, respectively). Clay content was directly related to the ability to image either seminal roots or lateral roots. In those soils with greater clay content, larger seminal roots, but no lateral roots were distinguishable [72]. At low clay content, however, MRI performs quite well. Dusschoten et al. (2018) successfully performed a quantitative analysis of three crop roots using a 4.7 T magnet in a sandy loam with 4% clay content and less than 0.2% ferromagnetic particles by mass [73].

In all the experiments described above, the researchers used a HF-MRI unit in a laboratory setting to determine the extent an MRI could image roots in the soil. The higher magnetic field produces a higher spin polarization in the material being studied, which may result in a detected signal with a higher signal-to-noise ratio (SNR), but also will produce image artifacts due to the presence of soil with relatively high magnetic material content. To avoid this issue, researchers created artificial soils with low magnetic material (< 4% by mass) which correlates with relatively low clay contents (~ 10% or less).

We hypothesize that the operation of an MRI in a low magnetic field regime (LF-MRI) will reduce or remove image distortions, while preserving the ability to use the difference in relaxation times between soil water and root water as a contrast mechanism to allow the separation of their signals. It will enable scientifically useful images to be obtained in agriculturally relevant soils. We describe four specific experiments that answer the critical questions concerning the implementation of a LF-MRI for root phenotyping.

1) The determination of the NMR properties of soil water and root water at low magnetic fields.
2) The development and testing of a small-scale MRI system operating at 47 mT in four soil types.
3) Determination of the relationship between LF-MRI signal-to-noise-ratio (SNR), image resolution and scanning time at 47 mT field strength for roots in soil.
4) Evaluation of a deep neural network approach (AUTOMAP) to improve SNR and image quality for plant root imaging with LF-MRI

3.2. Material and Methods

3.2.1. Field Sample Collection

TX08001, a bioenergy sorghum hybrid (*Sorghum bicolor* (L.) Moench.), was planted on May 30th, 2018 at the Texas A&M AgriLife Field laboratory in Burleson County, Texas USA. Sorghum was planted to a depth of 2.5 cm with a row spacing of 76 cm in two soil types, a Weswood silt loam, (a Udifluventic Haplustept, 25 % clay, mixed minerology) and a Belk clay (a Entic Hapludert, 49 % clay, mixed minerology) and has a high coefficient of linear extensibility. Standard agronomic practices were employed for fertilization and cultivation. Soil cores containing sorghum roots were collected roughly 120 d after planting from the two field sites.

A hydraulic soil probe (Giddings Machine Company, Inc., Windsor, CO., USA) mounted on a 1-ton pickup truck was used to collect soil cores with a diameter of 5.7 cm. The probe had a polyethylene terephthalate (PETG) sleeve insert allowing the collection and easy removal of the soil core from the probe. The probe was pushed into the ground adjacent to the crown roots on the inner-row side of the sorghum plant to a depth of 30.5 cm. The plastic sleeve was then removed from the metal core with the soil and roots contained inside and marked to indicate the core’s orientation to the plant stalk. Two cores were collected on either side of a given plant stem, between the rows in both the Weswood silt loam and the Belk clay on each collection day. Each core was cut into a 0-to 7.5-cm and a 7.5- to 15-cm depth section, for a total of four cores representing one plant for each soil type. The cores were treated for fire ants and shipped overnight to ABQMR, Inc., (Albuquerque NM) for laboratory-based LF-MRI imaging where the cores were refrigerated at approximately 8 C between imaging sessions.

3.2.2. Greenhouse Sample Collection

To test the system in a broader range of soils, rhizotrons (26.1-cm diameter, 75-cm long) were filled with dried ground soil. Either a Houston Black clay soil (52 % clay, smectitic minerology, an Udic Haplusterts) which has a high coefficient of linear extensibility, or a sandy loam soil (5 to 10% clay) purchased from a nearby landscaping supply store was used. Sorghum was planted in the rhizotrons, with cores being collected starting at roughly 90 d after planting. A 6.4-cm diameter soil core was collected to a depth of 37.5 cm. The full core was then cut into five 7.5-cm long sections for imaging and comparison.

3.2.3. NMR Properties of Soil and Roots

While it is not the goal of this paper to give an in depth description of the physics of an MRI system, we recognize that more background information may be helpful to understand the methods put forth in this paper. The following publications are excellent introductions to the basics of MRI [74] [75] [76] [77].

Soil and root image contrast is determined by the water NMR relaxation times (T_1, T_2) in the target material (roots) and the surrounding background material (soil). In the application of MRI, T_1 determines the maximum rate of repetition of the imaging pulse sequence, while T_2 determines the maximum time after the initial radio frequency (RF) pulse that the signal can be obtained. Our imaging strategy for the root vs soil discrimination is based on the differences in T_2 relaxation time, and therefore measurements of these parameters under realistic conditions is critical.

We used an inversion-recovery sequence with a Carr-Purcell-Meiboom-Gill (CPMG) [75] read out to measure T_1 and T_2. A custom built 267 mT NMR scanner was used on eight soil samples to explore the usefulness of LF-MRI in soils while the 47 mT scanner (which is discussed later) was being constructed. After construction of the 47 mT system was completed, six soil samples were re-tested to verify that relaxation values were similar between the two systems. A range of clay contents (8 to 65 %) with seven different water contents (0.05 to 0.35 kg kg^{-1}) were explored. To obtain the range in water content, the soils were air dried, passed through a 2-mm sieve, and wet by weight (with an oven-dry correction). Fifty inversion times from 10 to 100 ms were evenly spaced on a log scale. The repetition time was 200 ms, and 150 echoes were generated at an echo spacing of 120 µs. Depending on moisture content, the number of averages ranged from 4 to 64.

A second experiment was conducted to measure T_1 and T_2 in three samples of approximately 2-mm diameter sorghum roots. The soil was washed off and the roots were placed in a glass container for scanning. We used 40 inversion times from 500 µs to 5 s evenly spaced on a log scale. The repetition time was 10 s and there were 64 echoes with echo spacing of 10 ms and 4 signal averages.

3.2.4. 8-cm Bore MRI System

An MRI system was designed and built to test the hypotheses that operation at low magnetic field would allow the generation of root images in agricultural soils. A 47 mT electromagnet (corresponding to water NMR frequency of 2 MHz) with an 8-cm bore and 30 cm in length (figure 3-1A) was used to image each soil core. The magnet was wound on an 18-cm outside diameter (OD) nylon cylinder. An electromagnetic system was chosen based on the long-term plans for field deployment, where we believe it is advantageous to be able to switch the magnet on and off for safety reasons. The electromagnet main solenoid and end corrections coils were energized by separate power supplies (Hewlett-Packard 6012B) which were operating near their (kw) capacity. This operational capacity was a driving consideration for choosing 47 mT.

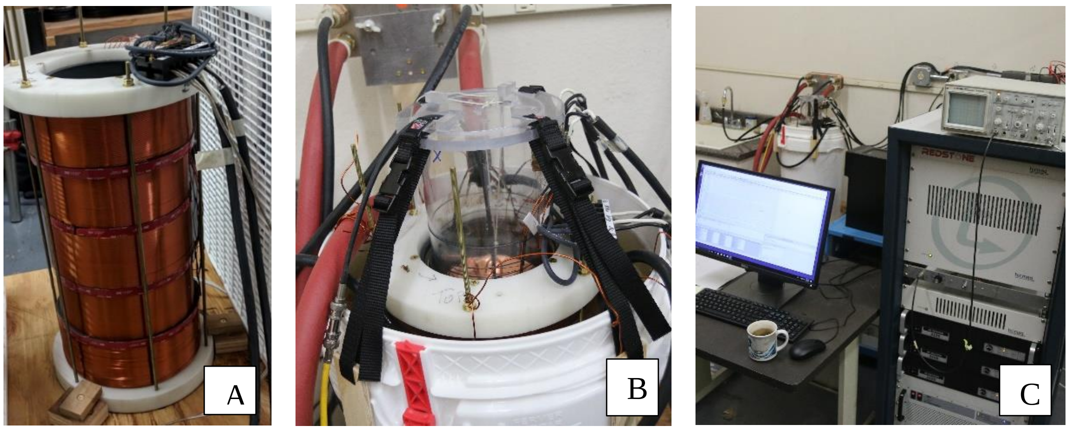

Figure 3-1: Image 1.A is the 8-cm bore electro magnet. Image 1.B shows the magnet, RF coil, and gradient coil placed in the cooling oil. Image 1.C shows the Techmag Redstone along with the computer that controls the system.

An in-house manufactured gradient coil was wound on a 12.5-cm OD polycarbonate cylinder, which was used to spatially encode the roots in a 2-D *k*-space. The 1 kW of heat generated in the 16 AWG wire of the magnet's main windings and end windings was removed by using recirculated hydraulic oil and an oil-to-water heat exchanger (figure 3-1B). A transmit-receive radio frequency saddle coil was wound on a 11.5-cm OD polycarbonate cylinder and was used to apply the RF pulse and then receive the magnetic resonance signal from the sample. Three AE Techron model 2105 amplifiers (Audio Electronics, Inc., Elkhart IN) were used to drive the three gradient coils, and a single Tomco RF amplifier (Tomco technologies, Stepney, South Australia) was used to generate the RF pulses used to flip the nuclear spins. A Tecmag Redstone console (Tecmag, Houston TX, USA) was used to control the pulse programmer, RF transmitter and receiver, and the gradient system (figure 3-1C). After the construction of the 47 mT scanner, six soils from the above experiment were tested to verify that the relaxation values at 47 mT approximately agreed with those found with the 267 mT scanner.

To demonstrate that a LF-MRI system can be used for visualizing roots in soils, 2-D projection images were acquired from cores collected from two different sources. The field soil cores collected from the Weswood silt loam and Belk clay were used as well as the Houston Black clay and sandy loam rhizotron cores. For these images, a CPMG [75] sequence was used where each echo is acquired with the same phase encode and read out gradients. This approach allows all of the echos to be averaged to improve the SNR. In this work, we leave the third dimension unresolved. Two approaches to the 2-D imaging are reported here, both use the pulse sequence shown in figure 3-2. The first sequence uses eight sequential spin echoes, with an echo spacing of 7 ms and a 2-D projection image acquisition time of 1 hour. The second sequence uses sixteen sequential spin echoes with an echo spacing of 7 ms; fewer signal averages were used, so the image acquisition time for each 2-D projection in this experiment was 15 minutes. For both methods a 0.5 second repetition time was used, along with a field of view of 80 mm. For both approaches, the RF-pulses were rectangular (or “hard”) pulses [77] in time (figure 3-2). Each echo (either eight or sixteen) acquired the same line in *k*-space such that the data were averaged for improved signal-to-noise ratio. These sequences parameters were chosen to produce the best SNR for the system. The timing implies that soil water signals (T_2 <4ms) were heavily suppressed while the root water signals (T_2~100ms) were only slightly attenuated, resulting in root images that are T_2-weighted.

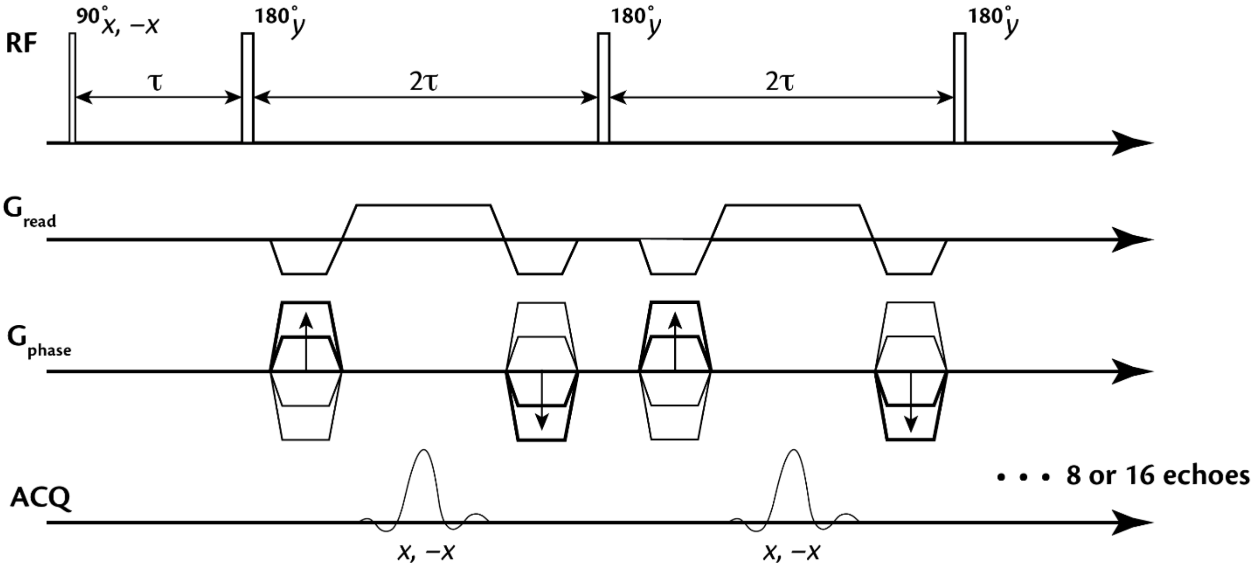

Figure 3-2: Pulse sequence for image generation uses CPMG pulse sequence that is fully rewound, both for phase encode and frequency read out. The subscripts refer to the phase of the RF transmit, data acquisition. τ and 2 τ are RF pulse spacing. Depending on the experiment either 8 or 16 echos are acquired and averaged together for each phase encode.

The time domain *k*-space data was appended with zeros (known as zero -filling) to create an interpolated image of a standard size regardless of the pixel resolution. For the experiments described here, the acquired *k*-space matrix sizes which range from 48 x 48 to 92 x 92 (the second number is the number of phase encode steps) being zero filled and transformed to create images that are 128 x 128 pixels. The images were reconstructed from *k*-space using the conventional Inverse Fast Fourier Transform (IFFT), or with AUTOMAP.

3.2.5. SNR, Resolution, Scanning Time

To explore the relationship between image resolution, image acquisition time and signal-to-noise ratio (SNR) one Weswood silt loam core and one Belk clay core were imaged six times each. For both soil types, two sets of 2-D projection images are generated with a fixed field of view of 80 mm. For the first set of experiments, the scanning time was fixed and the resolution was changed from 1.74, 1.25, and 0.625 mm pixel^{-1}, which causes the image SNR to change in response. For the second set of experiments the images were acquired at the same spatial resolutions as before; however, the image acquisition times were increased accordingly to deliver a nearly constant SNR. The data were zero filled as described above, resulting in images that are 128 x 128 pixels.

3.2.6. AUTOMAP

Low field MRI generally suffers from low SNR due to the intrinsically low Boltzmann spin polarization. As a result, relatively long acquisition times are needed to accommodate the additional signal averaging required to attain sufficient SNR. Zhu et al. (2018) have recently described a deep-neural-network-based approach for image reconstruction known as Automated Transform by Manifold Approximation (AUTOMAP). It leverages data-driven learning of the low-dimensional manifold representations of real-world data that are robust to corruptions, such as noise, and have been shown to improve imaging performance. This method is applied to the raw data in *k*-space and is used to transform the MRI data to image space.

We assessed the performance of AUTOMAP reconstruction to improve the imaging quality of the LF-MRI system. The image SNR was used to compare

AUTOMAP reconstruction of the same 2-D LF-MRI data with the more conventional inverse fast fourier transform reconstruction method. Six images corresponding to three soil types were reconstructed at resolutions of 1.67, 1.11, and 0.83 mm pixel^{-1}.

AUTOMAP was trained on the Fourier forward-encoding model using a training corpus assembled from 55,000 2-D synthetic roots images. These root images were generated using a 3D root system growth model implemented in MATLAB- called RootBox (Dunbabin et al 2013). Random additive white gaussian noise was applied to each image in the training set to expedite manifold learning during training. To produce the corresponding *k*-space representations for training, each noise-corrupted image was Fourier Transformed with MATLAB's native 2-D FFT function. The neural network was trained from the noise corrupted *k*-space encodings and target 'noise-free' images to learn an optimal feed-forward reconstruction of *k*-space domain into the image domain. The network architecture described in Zhu et. al. 2018 was used in this experiment. The raw 2-D *k*-space datasets from all samples were stacked and multiplied by a scalar so the range of signal intensities lies within that of the corresponding training models. The stacked *k*-space datasets were then reconstructed with the trained model. The signal magnitude of each 2-D dataset was normalized to unity to enable fair comparison between both reconstruction methods. SNR was then computed by dividing the signal magnitude by the standard deviation of the noise.

3.3. Results and Discussion

3.3.1. NMR Properties of Soil and Roots

A large difference was seen between the NMR T_2 relaxation times of soil water in the eight soils tested (figure 3-3) and in roots. An increase in the relaxation time corresponds with an increase in the water content for all soils tested; however, the rate of increase with water content is dependent on soil type. Relaxation times of soil water are strikingly short when compared to free water or root water, leading us to conjecture a relaxation mechanism where the ^1H nuclei interact with paramagnetic ions in the soil. As soil water content increases, the soil surface area is unchanged, leaving increasing amounts of free water in the soil matrix. Hence surface-bound water becomes a smaller fraction of the total soil water. This indicates that in this system, the water relaxation is dominated by the surface bound water interacting with soil paramagnetism. This results in the relaxation time for water in a soil increasing as the amount of soil water increases; however, proving this hypothesis requires further research. The measured T_2 relaxation in soil water as a function of soil water content is plotted in figure 3-3.

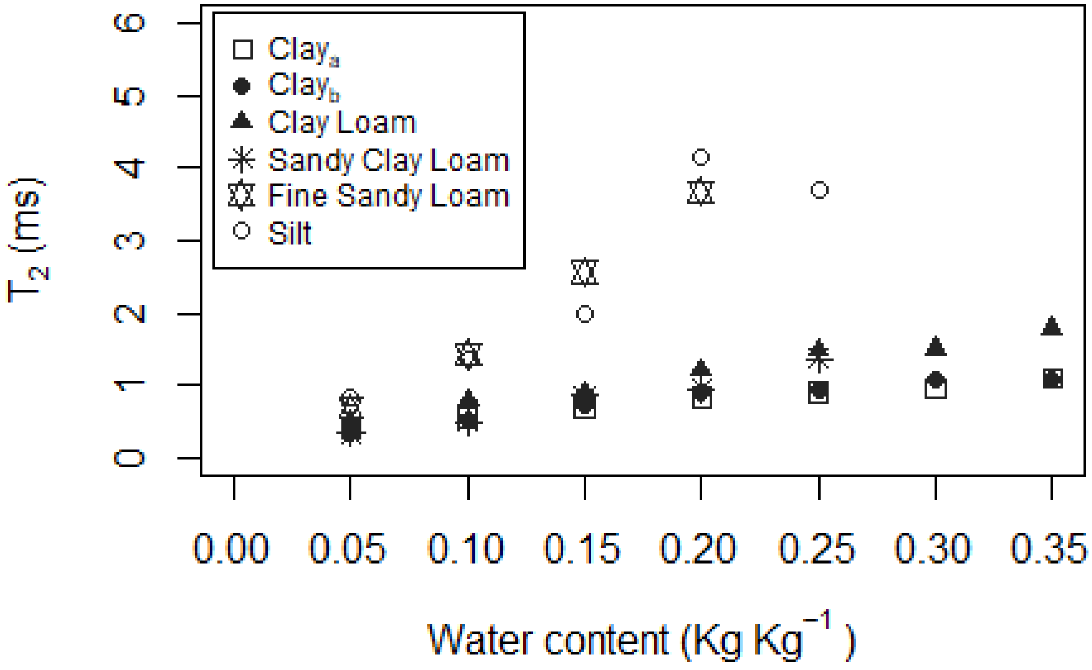

Figure 3-3: Measured soil water T2 versus water content for six soils with different texture classes. As water content increases, the relaxation times also increase. T2 also varies between textures.

The T_2 relaxation time for the soil water across the tested soils ranged from 0.33 to 4.14 ms, and T_1 ranged from 0.51 to 9.54 ms (table 3-1). Soil water contents ranged from permanent wilting point to field capacity for each soil, as a representative range of possible water contents in the field. In contrast, the T_1 relaxation time for water in bare roots was between 0.7 and 1.2 s, and the T_2 relaxation time of water in bare roots ranged from 85 to 140 ms. By adjusting the NMR echo time in the LF-MRI pulse sequence such that it is long in comparison to T_2 of soil water and short in comparison to T_2 of root water, we are able to image the root water without signal contamination from soil water.

Table 3-1: A summary of the soil particle size distribution for nuclear magnetic resonance relaxation times (T1 and T2). N/A represents a soil water content that was not achievable because it is beyond the liquid limit for that soil.

	Particle size distribution			Relaxation times at 0.1 kg kg^{-1} water		Relaxation times at 0.25 kg kg^{-1} water	
Texture class	**Sand**	**Silt**	**Clay**	**T_1**	**T_2**	**T_1**	**T_2**
	%			ms			
$Clay_a$[†]	3.1	33.5	63.4	0.98	0.55	1.61	0.90
Silty Clay	3.0	44.3	52.7	0.88	0.47	1.60	0.88
$Clay_b$[†]	8.6	39.4	52.0	0.74	0.52	1.31	0.94
Clay Loam	32.5	34.0	33.5	1.3	0.77	2.46	1.47
Silty Clay Loam	15.2	56.1	28.7	1.32	0.70	2.37	1.31
Sandy Clay loam	55.7	14.5	21.8	1.3	0.49	3.95	1.37
Fine Sandy Loam	69.8	20.4	9.8	2.37	1.42	N/A	N/A
Silt	3.0	89.1	7.9	3.01	1.37	7.97	3.7

[†] *$Clay_a$ has mixed mineralogy; $Clay_b$ has smectitic mineralogy.*

3.3.2. Imaging System

A critical step for this work is the development and testing of a LF-MRI system capable of producing images of roots in agricultural soils. Figure 3-4 shows 2-D projection images, acquired in the 8-cm bore system, of field-collected, intact cores. Figure 3-4A shows roots in the Weswood soil (25 % clay), and figure 3-4B shows root in a Belk clay (49 % clay). Both images are 2-D projections of cores that are the top 0 to 7.5 cm depth. The images have a resolution of 0.8 mm $pixel^{-1}$ using a scan time of 1 hr. The roots shown here are nodal roots of sorghum that are between 1.5 and 2.0 mm in diameter. In this projection image some of the brighter pixels represent one or more roots crossing each other.

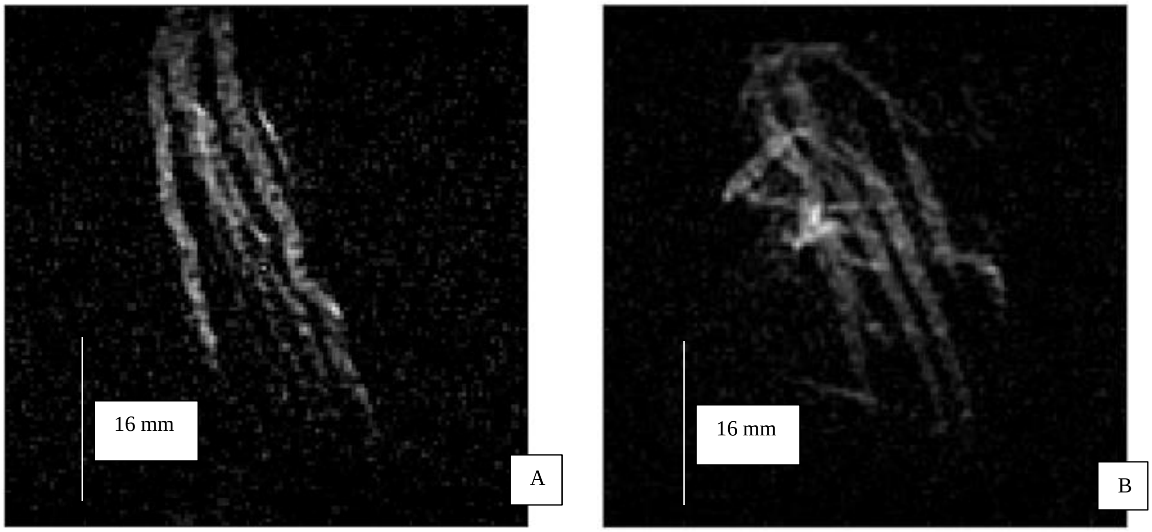

Figure 3-4: Energy sorghum root images acquired in the 8-cm LF-MRI scanner. Roots shown in this image are nodal roots that are 1.5 to 2.0 mm in diameter. Both images are of intact soil cores collected at 0 to7.5 cm depth, have a resolution of 0.8 mm, and an acquisition time of 1 hour. Image A) is a Weswood silt loam and B) is a Belk clay; both are collected adjacent to the plant.

2-D projection images acquired in the 8-cm bore LF-MRI scanner of soil and root cores from the rhizotrons are shown in figure 3-5. These images were acquired with a 15-min scanning time and pixel size of 1.74 mm. Figure 3-5A shows a full root crown in a Houston black clay rhizotron. Figure 3-5B shows a similar root crown grown in a sandy loam rhizotron. When figures 3-5A and 3.5B are compared, one can see different rooting structures that are likely the result of soil type, as all other environmental factors were similar. The apparent blurring in figure 3-5 is due to the relatively low image resolution combined with the visualization of 3-D information in a 2-D projection image.

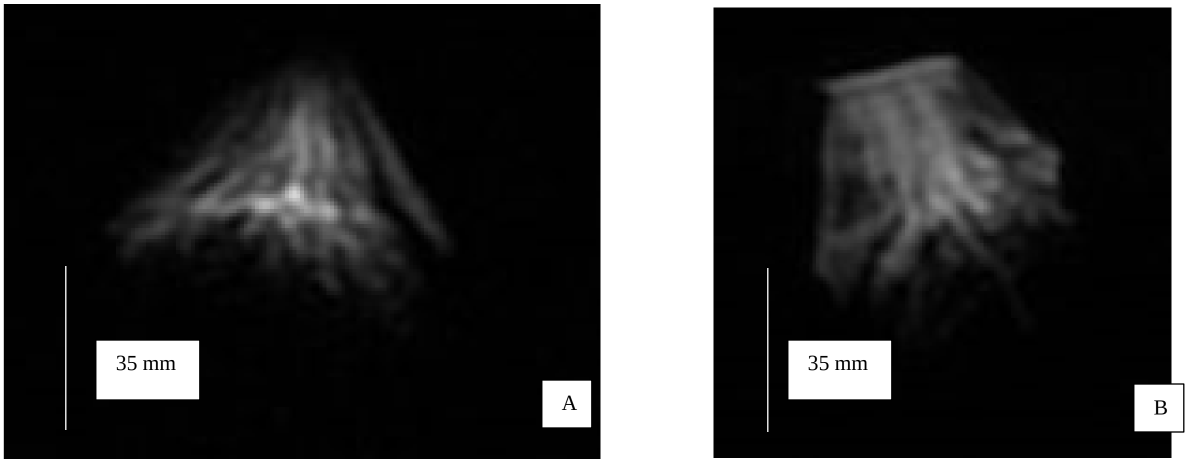

Figure 3-5: A) LF-MRI of the root crown from a rhizotron-grown greenhouse sorghum in a Houston Black and B) manufactured sandy loam soil. The plants were harvested approximately 90 days after planting. The roots seen in these images are 1.5 to 2.0-mm in diameter.

Experimental results in figures 3-4 and 3-5 demonstrate that we can generate 2-D projection images of roots with a diameter of 1.5 mm or larger, in moderate to heavy clay soils using this LF-MRI system with relatively short image acquisition times of 15 to 60 minutes. Increased signal averaging obtained through longer acquisition times generates higher SNR and will allow smaller roots to become visible in the images. The images presented in figures 3-4 and 3-5 are reconstructed using the IFFT method.

3.3.3. SNR, Resolution, Scanning Time

To develop a successful imaging protocol, the relationship between SNR, image acquisition time, and resolution must be determined. Figure 3-6 (A-C) shows an image collected of a Weswood silt loam core, with nodal roots ranging from 1.5 to 2.0 mm in diameter. While holding the image acquisition time constant at 30 minutes and setting the image pixel size at 1.74, 1.25, and 0.625 mm pixel^{-1}, the SNR changes in response. The resulting SNR becomes smaller (worse) as the pixels become smaller, making it harder to identify roots in the image. Figures 3-6(D-F) show the same roots, but here the SNR is held constant as the resolution is changed from 1.74, to 1.25, and 0.625 mm pixel^{-1} and the acquisition time is increased from 0.5 to 4 hrs.

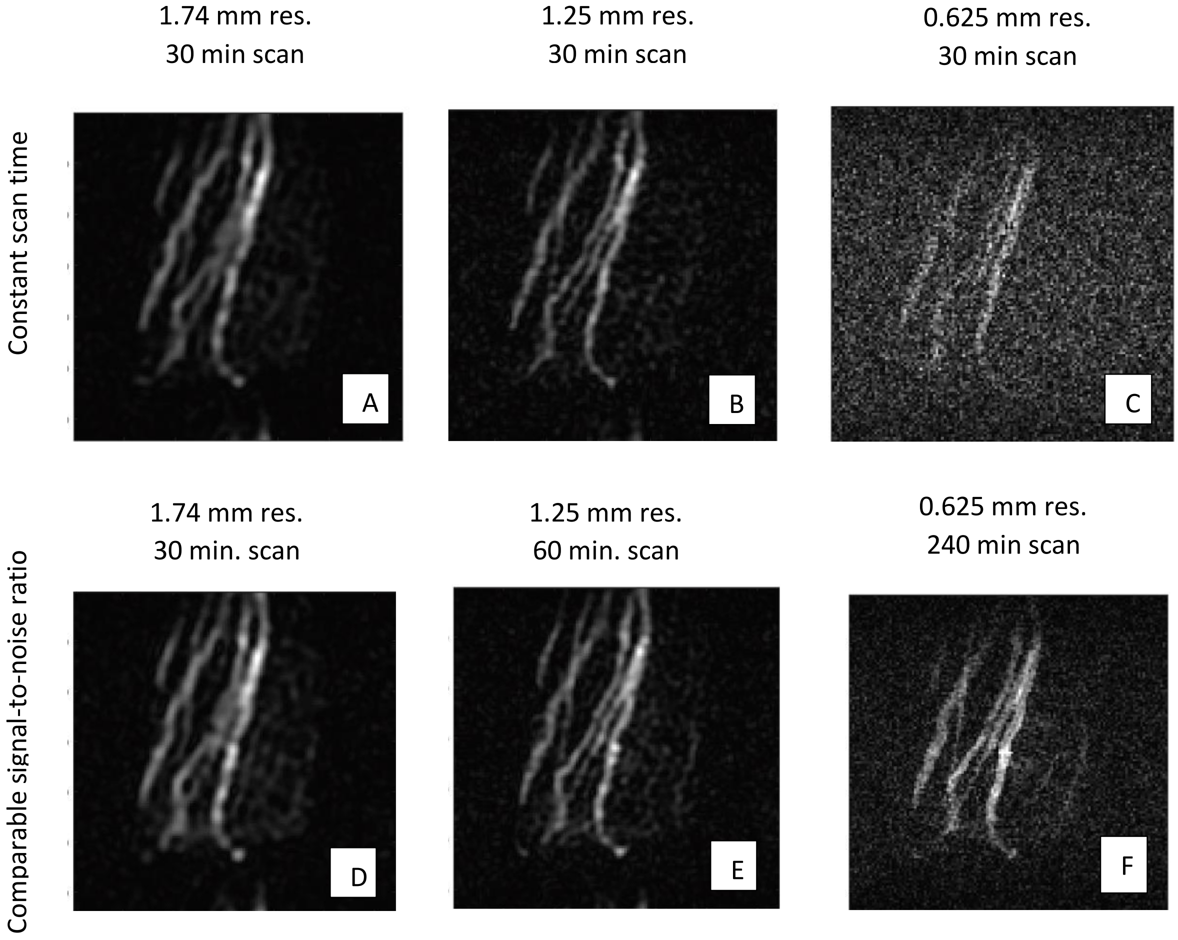

Figure 3-6: LF-MRI images of sorghum roots in a Weswood silt loam soil core, all with a fixed FOV of 80 mm. Images (A-C) were acquired in 30 min, with the indicated image resolution, leading to differences in image SNR. Images (D-F) were acquired with acquisition

Figure 3-7 shows a similar relationship for a Belk clay soil core, confirming the conclusion that the resolution and SNR are inversely related for a constant scan time. Likewise, resolution and scan time are inversely related for a constant SNR, and none of these properties are related to the soil texture. These experiments indicate that for a successful imaging sequence we will need to balance resolution, SNR, and image acquisition time to create a practical field-based imaging system that creates useful images in a reasonable time frame.

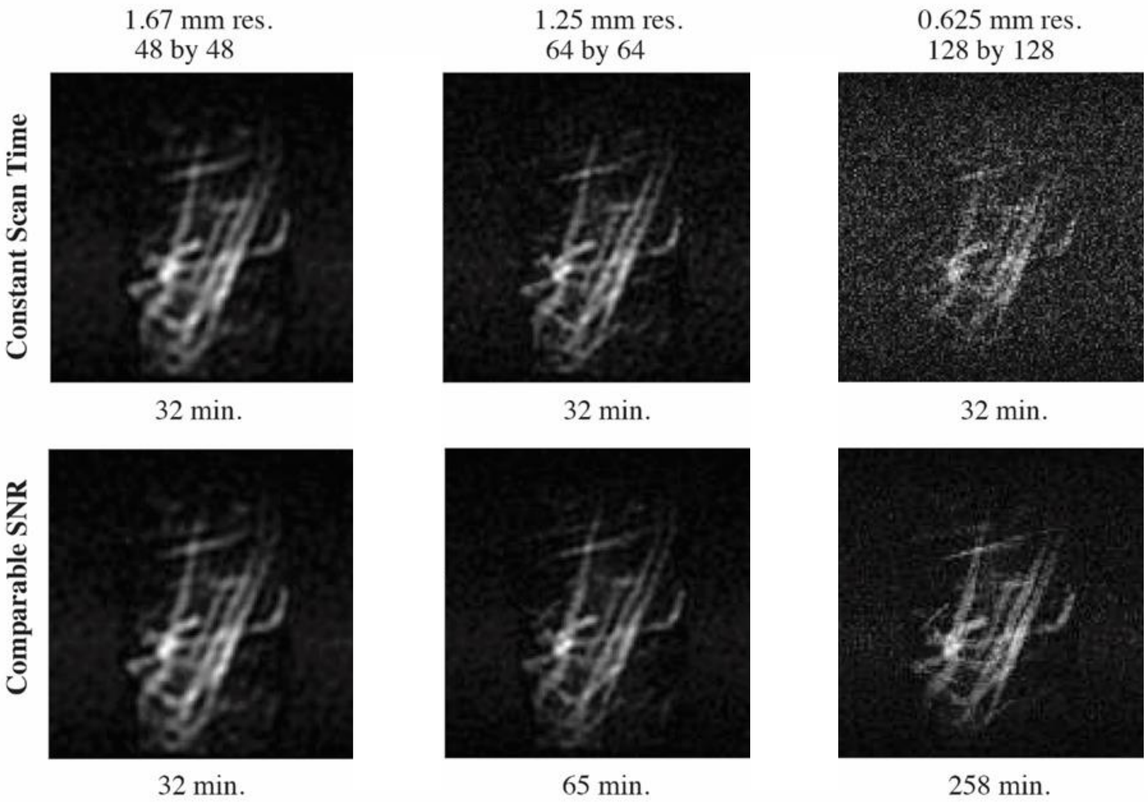

Figure 3-7: LF-MRI images of sorghum root in a Belk clay soil core, all with a fixed FOV of 80 mm. Images (A-C) were acquired in 32 minutes, with the indicated image resolution leading to different SNR. Images (D-F) were acquired by selecting image acquisition time for each improvement in image resolution.

3.3.4. AUTOMAP Image Reconstruction

AUTOMAP reconstruction versus conventional IFFT reconstruction method of roots images is shown in figure 3-8 for two Belk clay soils. Images acquired with a matrix size of 48 x 48 (spatial resolution of 1.67 mm) showed an improvement in the mean SNR of 69% and 29% compared to the standard IFFT method. The noise levels in these images are lower by more than 30%, giving the roots architecture better contrast with the MR signal from the soil.

For the 72 x 72 matrix size (1.11 mm spatial resolution) root images from Houston Black clay (figures 3-8 E - F) and from the sandy loam (figures 3-8 G and H), where the SNR of the standard IFFT image was high, showed improvements of 161 and 148 %, respectively.

For the 96 x 96 matrix size (spatial resolution of 0.83 mm) root images collected from Houston Black clay (figures 3-8 I and J) show a mean SNR improvement of 171%. The same images shown in figure 3-8 (K and L) with a lower window level, reveal the significant noise floor reduction when the data is reconstructed with AUTOMAP.

For the 128 x 128 matrix size (spatial resolution of 0.63 mm), the root images reconstructed with AUTOMAP not only show an improvement of 88% in mean SNR but also the removal of spike artifacts (figures 3-8 M and N). As seen in the windowed images in figure 3-8O and 3-8P, the RF leakage artifact (horizontal streak near bottom) was significantly eliminated with AUTOMAP reconstruction.

The improved contrast in roots, reduction of noise, and spike artifact elimination indicate the utility of AUTOMAP. The lowering of the noise floor, and the improvement to the SNR allows the user greater latitude to adjust the scanning time, resolution or SNR by providing a greater range post hoc.

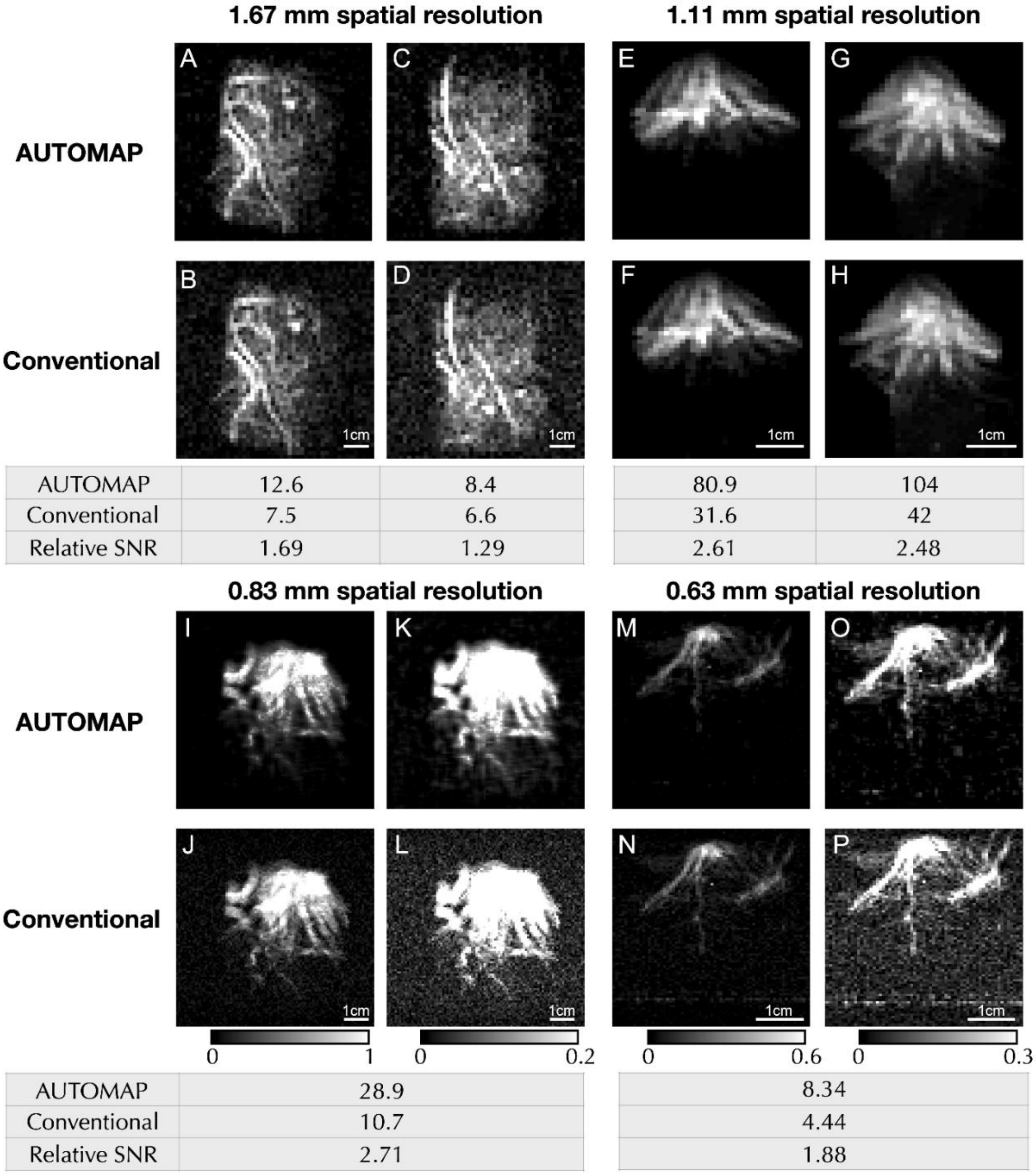

AUTOMAP	12.6	8.4	80.9	104
Conventional	7.5	6.6	31.6	42
Relative SNR	1.69	1.29	2.61	2.48

AUTOMAP	28.9	8.34
Conventional	10.7	4.44
Relative SNR	2.71	1.88

Figure 3-8: AUTOMAP versus Conventional IFFT reconstruction method of roots images – Four spatial resolutions are shown – 1.67 mm pixel size (A - D), 1.11 mm pixel size (E - H), 0.83 mm pixel size (I - L) and 0.63 mm pixel size (M - P). For each set of spatial resolutions, the top images were reconstructed using AUTOMAP and the bottom images were reconstructed using the conventional IFFT method. Images (I and J) were windowed to a lower level in images K and L respectively, to show the decrease in noise. Likewise, the images (M and N) were windowed to a lower level in images (O and P) respectively, to show the noise reduction and spike elimination. For each figure, image intensities are displayed in a windowed range of intensities (from 0 to 1), as indicated on the legend. The table indicates the image SNR for both reconstruction approaches and tabulates the fractional SNR enhancement seen with AUTOMAP.

3.3.5. Conclusion

Visualization and measurement of root structure *in situ* would aid in understanding the function of roots and how roots behave under different environmental conditions. We have demonstrated that low field MRI can allow scientists to detect and visualize roots through intact, natural soils and collect spatial information to aid in understanding root morphology, architecture and development. While previous studies have shown the difficulty of using high field MRI and soils with high clay content (>10%), these issues are less problematic when using low field MRI.

We have demonstrated that the soil water signal relaxation time T_2 is much shorter than root water signal (4 ms *vs*. 120 ms), allowing soil water signals to be suppressed, resulting in images of roots in the soil. We have measured the clay content and have shown that LF-MRI is still successful in situations with moderate to high clay content. We have shown that images can be collected in soils with more than 10% clay content. The images shown in this paper demonstrate that there is a balance of scanning time, SNR, and resolution to be optimized. We have also demonstrated that AUTOMAP can be used to improve the SNR (by 29 to 148%) and lower the noise floor during the image reconstruction stage, allowing for more flexibility in the application of a LF-MRI system.

The next step in our research is to develop an LF-MRI system that can be deployed in the field. It is ideal to be able to image lateral roots that have smaller diameters in addition to the larger diameter nodal roots. For imaging smaller roots, we will need to improve the SNR, which will be done by further improvements to the hardware, software, and by continuing to explore the use of AUTOMAP. To continue this research in the field, the system will be scaled up. It is our goal to increase the linear size of the magnet by a factor of three; we expect to be able to generate a 1.5 mm resolution image in approximately 25 minutes.

4. LOW FIELD MAGNETIC RESONANCE IMAGING OF SORGHUM ROOTS IN THE FIELD

4.1. Introduction

In situ root measurements for the purpose of crop improvement are difficult due to the opaque nature of soils. The process of measuring roots in natural soil is typically labor intensive and often requires digging out the roots and washing soil away before measurements can be acquired. Plant breeding, and root phenotyping in particular are developing crop phenotypes to address drought resilience [78] [79], nutrient recovery [80] and to increase rooting depth and biomass to enhance soil organic carbon storage [81]. In this work we explore the availability of tools and techniques for root phenotyping, and build upon a previous design [82] to develop a novel field based Low Field Magnetic Resonance Imaging (LF-MRI) Rhizotron for root scanning.

Root systems architecture is the spatial configuration of the roots [17]. It is well established that root system architecture plays an important role in plant growth and productivity [79] [83] [84] [85] [86] [87]. It is also understood that the most aspects of the environment, such as soil ph, temperature, and salinity effects the root system architecture [88] and are therefore important elements in the plant breeding process.

Root phenotyping can be subdivided under two categories: The first, laboratory-based phenotyping, tends to rely on controlling all aspects of the environment which allows meticulous experiments to be constructed. But these methods also tend to do a poor job of replicating the plants natural environment such as plant-to-plant interactions, light and temperature fluctuations, soil structure and natural soil heterogeneity to name a few. Laboratory experiments often employ techniques such as hydroponics [78], clear gel growth media [89] or aeroponics [90] to study root structure. These systems allow the roots to be measured and inspected more easily, but at the cost of the environmental impact of the natural soil environment thus limiting the phenotypic data available. When natural soils are used in laboratory settings the soil is often ground and packed into pots or rhizotrons. This method homogenizes the soil and removes the natural preferential pathways associated with soil structure. Thus, changing the rooting environment from those found in natural soils. The rhizotron edges also restrict rooting structure resulting in edge effects soon after the plant emerges.

The second category is in-field root phenotyping, which provides researchers the chance to investigate plant-to-plant interactions, soil interactions, and other environmental and management impacts. However, field-based root phenotyping tends to have less sophisticated tools for measuring root architecture because of agricultural environmental factors such as moisture, heat, dust, and vibrations from surrounding equipment. Additionally, working with in-tact soils, especially those with silicate clays in them is difficult. A lack of tools suitable for field-based root phenotyping is a significant impediment to root phenotyping [79]. Therefore, root phenotyping technology that can be operated in the field and can capture the interaction between genetics, environment and management (G x E x M) expressions is needed.

One common field-based method is the excavation and washing of the roots (shovelomics). After excavation, the roots are then either scored visually [59] or a newer approach uses an image processing platform to measure the root metrics [91] [92]. This method allows the quantification of many root traits, is low tech (high usability) and can be used for high throughput. But shovelomics is very labor intensive, the true root system architecture cannot be known once the soil is removed, and it is difficult to know how much information is lost from disturbing the root system. Shovelomics tends to work well for cores root metric information such as nodal root length or root crown size. Other field-based methods include mini-rhizotrons [93], electrical root capacitance [94] [95] and soil coring [79] [96]. The mini-rhizotron method provides information on timing and abundance of root growth but does not provide useful root architecture data because the roots will tend to preferentially grow around the rhizotron tubes. Electrical root capacitances can provide estimates of root biomass, and because the plant does not have to be destroyed can provide root biomass growth information over time. However, this method lacks the ability to give root length, diameter, or architectural information. Collecting soil and root cores allows root diameters to be correlated with depth and sometimes distance from the plant. But this method does not provide root architecture information, or root growth over time since the plant is destroyed during sampling.

As computing has improved in speed and size, and as machine learning algorithms increase in popularity, data-heavy imaging systems have become more common place for root phenotyping as well. Systems such as 2-D optical scanners [60] and X-ray computer tomography (CT) [57] [97] have been used. The 2-D optical scanners work well for small seedlings in a laboratory setting but roots quickly run out of room as they grow and the system requires that the roots are pressed between two surfaces to be imaged resulting in relatively simple 2-D root structure. X-ray CT systems are effective for imaging root system architecture, but these systems are currently only suitable for laboratory imaging due to safety and infrastructure requirements.

Magnetic resonance imaging systems have been tested and used for both above ground plant phenotyping and below ground root phenotyping. High field MRI systems (ranging from 1-10 T) have been used to measure soil water relaxation times, finding that each soil type has a different relaxation time, making a universal calibration method difficult [68] and making the type of soil used with an MRI experiment quite important [98]. High field MRI have also been used to show that it is possible to differentiate between the soil water and root water [71] when using a suitable soil. But magnetic material found in some soils tends to create distortions in the images. When operating at high field in soil with more than 10% clay content [72], or more than 4% paramagnetic material by weight [73], these distortions become significant or even severe. High field MRI systems are capable of creating high-quality three-dimensional root system architecture images and generate root phenotyping data [99] [100] [98]. However, the above soil constraints, coupled with high power demands and the sensitivity of the MRI to environmental noise result in MRI systems not been widely used for root imaging.

When an MRI is used for root imaging sandy soils are used in under laboratory conditions with a high field MRI.

Bagnall et al. demonstrated the use of a low field MRI (LF-MRI) system in a laboratory setting that allows roots to be visualized in soils with greater than 10% clay content, allowing the use of this technology in agriculturally relevant natural soils [82].

Root systems contribute to the overall health and robustness of the plant, and therefore are of major interest to plant breeders. The root system is impacted by the environment (planting density, nutrient availability, soil heterogeneity etc.) and thus the environment should be considered when phenotyping. However, there is a lack of tools that are capable of *in situ*, nondestructive root mapping for phenotyping. This paper presents outcomes of our overall goal to develop a field-based LF-MRI Rhizotron system. A field-based system must work in a hot, humid environment of a crop field and work in agricultural soils. Using the results of Bagnall et al. we will demonstrate in this work that by using a low field system and spin-echo pulse sequence it is possible to collect *in situ* root data in the form of root biomass estimations and root system architecture images under agricultural field conditions. We address this goal through the following specific objectives,

1. Design and construct a field deployable Low Field Magnetic Resonance Imaging Rhizotron system,
2. Measure root biomass using the above LF-MRI Rhizotron in the field, and
3. Demonstration of root image collection for root system architecture analysis.

4.2. Material and Methods

4.2.1. The Low Field Magnetic Resonance Imaging (LF-MRI) Field Rhizotron System

One goal of the LF-MRI Rhizotron design was to produce a system that could be operated in, and moved between, the typical agricultural research plots. This requires that the system works in hot and humid field conditions and it must have portable power supply. This requirement also places upper bounds on the size, weight, and power consumption constraints for the LF MRI Rhizotron. Additionally, the Rhizotron needed to be large enough to capture enough of the root system architecture to be useful in root phenotyping, which was estimated to be 25 cm diameter and 25 cm deep.

Figure 4-1 is a schematic of the field equipment layout of the LF-MRI Rhizotron system. Field equipment included generators, an air-conditioned trailer, and other items to support the Magnet and data acquisition. The trailer contained the LF-MRI electronics and computing equipment and was powered by the two generators. The water chiller and the oil pump worked in tandem to keep the LF-MRI electromagnet within operating temperatures.

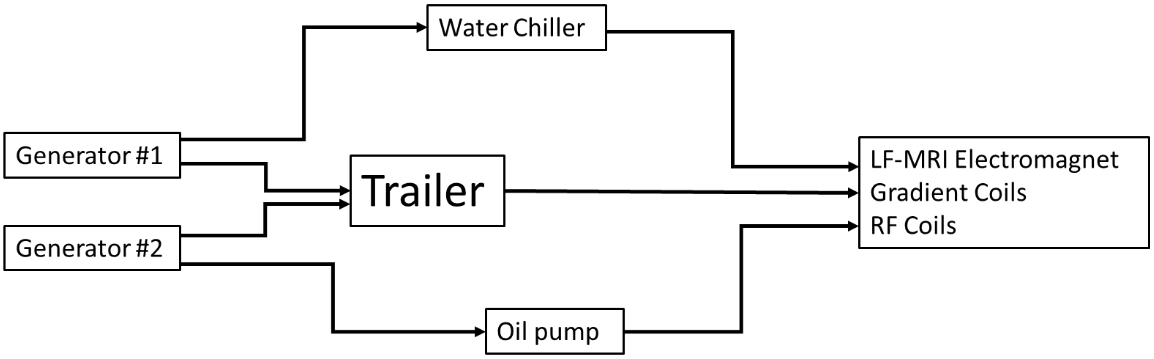

Figure 4-1: Schematic of the Low Field Magnetic Resonance Imaging (LF-MRI) Rhizotron equipment layout for field data collection. Two generators powered the trailer, water chiller, and oil pump. An air-conditioned trailer housed the LF-MRI control electronics, which is connected to electromagnet.

4.2.2. LF-MRI

The in-field LF-MRI Rhizotron is comprised of both off-the-shelf equipment and specially fabricated equipment. Because the LF-MRI Rhizotron must be mobile, a 3.6 x 1.5 x 1.5 m box trailer was used to keep some equipment cool and protect it from rain and dust. The trailer was outfitted with a heating/cooling unit and housed a commercially available NMR (nuclear magnetic resonance) spectrometer, radio frequency (RF) amplifier, gradient amplifiers, and electromagnetic power supply. The trailer was wired with two electrical panels; each panel was powered by a single 220v AC (alternating current) gasoline-powered generator (XP12000EH, Duromax, Ontario CA, USA; 12.5 kw, Generac, Waukesha WI, USA) (figure 4-2). The generators were placed in the opposite side of the trailer from the electromagnet, 12 m from the trailer to abate acoustic noise and minimize RF interference (see field equipment layout above, figure 4-1).

Figure 4-2: The generators used to power the LF-MRI system. The right (Duro) and left (Generac) units have ratings of 12 kW and 12.5 kW, respectively.

The trailer contained the electronic and computing equipment for the Rhizotron system. This equipment included an MRI console (Redstone, Techmag, Houston Texas, USA) as a system controller for the LF-MRI Rhizotron. The console controlled the RF receiver, RF transmitter coils, magnetic gradient coils and the conversion of AC current to DC current for the system (figure 4-3A). The RF transmitter coils, magnetic gradient coils and electromagnet are all housed together, with the RF transmitter coils placed inside the gradient coils, which are then placed inside the electromagnet (figure 4-3B)

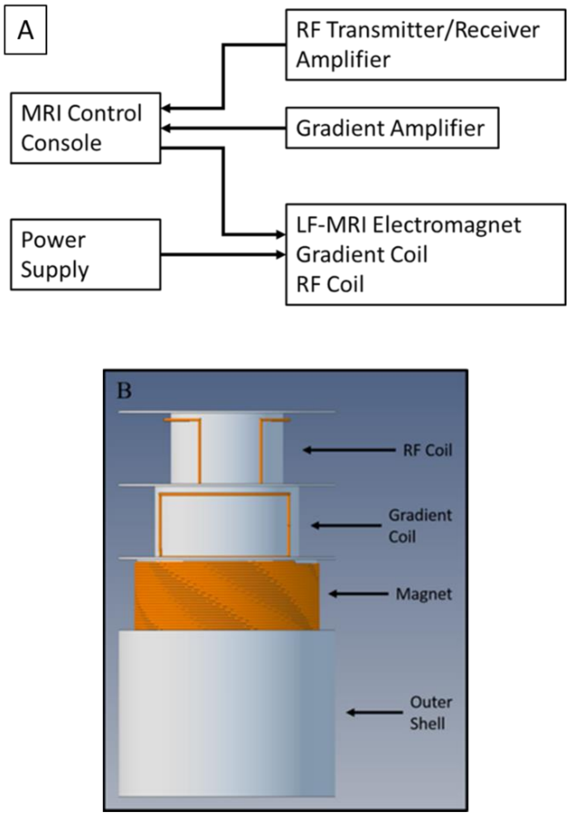

Figure 4-3: A) A Schematic showing how the Low Field Magnetic Imaging (LF-MRI) Rhizotron components are connected. B) Shows a schematic of how the components of the electromagnet assembly are assembled.

Three amplifiers (model 2105, AE Techron, Elkhart IN, USA) were used to drive the gradient coils (figure 4-4A). A forth amplifier (BT-0100 Alphas S-T, Tomco Stepney, SA, Australia) (figure 4-4B) was used to operate the RF transmitter coils. Three switching power supplies (6032A, Hewlett-Packard, Palo Alto CA, USA) were used to power the main electromagnet windings and end windings. Interior LED lighting, a desktop computer, and an air-cooling system were also housed and operated inside the trailer.

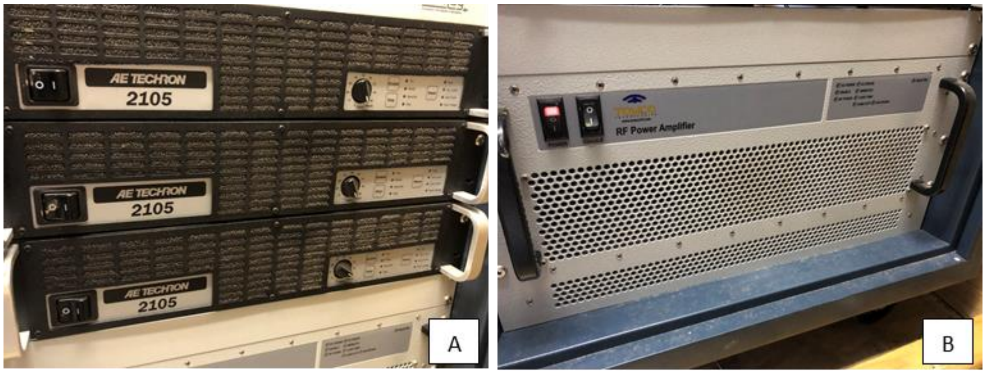

Figure 4-4: The amplifiers used for the LF-MRI system. A) The three gradient amplifiers B) the radio frequency amplifier.

Outside the trailer were the cooling system and magnet. The magnetic field was created by an electromagnet with a solenoidal main coil and two end correction coils, all of which were wound on a stainless-steel bobbin (figure 4-5). The static field (B_0) was produced using the main coil, a 300-kg winding of 16 AWG heavily enameled copper wire (Essex-Brownell, Indiana). The bobbin was made from 300-series stainless steel; the winding was 81-cm long and had an innermost diameter of 40.6 cm. There were 26 electrically independent layers of wire wound with the same helicity, creating neat, closely packed coils. The 26 layers were wired as 13 units in parallel, with each unit composed of two layers in series. This winding was operated at 26 A with a warm voltage drop of 50 V, corresponding to 2.0 A in each wire. The series-parallel configuration was selected to provide an appropriate load to the power supply; however, this configuration has an additional benefit of having most layer-to-layer voltages being nearly zero.

Figure 4-5: The magnet was constructed on a stainless-steel bobbin, wound with copper wire. The gray plastic polyvinyl chloride (PVC) housing holds in recirculating oil to cool the magnet.

To create a more uniform magnetic field, end windings were also included in this design. The magnetic field was calculated along the solenoid symmetry axis, and the length and number of turns of the end correction windings were chosen to eliminate the 2nd and 4th axial derivatives at the center of the imaging volume. The resulting electromagnet is a "sixth-order" design where the first non-vanishing axial derivative is the 6th derivative.

The three HP 6032A switching power supplies (figure 4-6) were used to power the electromagnet. Two of the power supplies were used in series to power the main magnet solenoid. The third power supply provided power to the end correction coils. The total power of roughly 2 kW appears as heat in the windings and is removed by coolant oil.

Figure 4-6: Three switching power supplies used for powering the magnetic field. Two were used for the main coil and one was used for the end correction coils.

The magnetic field gradient coils allowed spatial information to be encoded in the MRI signal and provided a method to improve the magnetic field uniformity with small linear increases to the field in the X, Y, and Z planes (also called shimming). For this system, the gradient coils followed the design of [101]. These coils provided better linearity than a simple Maxwell pair (for z gradient) and Golay coils (for x and y gradients) and were made from 18 AWG enameled wire. The transverse coils were laid-out on a thick polyethylene sheet with grooves to hold the windings. The flat coils were epoxied and baked in an oven. The eight flat assemblies (four each, for x and y) were curved to fit onto a 35.56-cm outside diameter (OD) polyvinyl chloride tube (PVC); the coils were epoxied in place after z gradient coils were wound directly onto the PVC (figure 4-7). All gradient coils were secured by winding the assembly with epoxied nylon webbing, and the assembly was housed on the inner surface of the electromagnet bobbin. The coils produced 100 μT A^{-1} cm^{-1}, yielding adequate gradient strengths with currents under 10 A. Active cooling of the gradient coils was not needed.

Figure 4-7: The gradient coils for the LF-MRI magnet. The z gradient coils were wound directly onto the plastic polyvinyl chloride (PVC) pipe, while the x and y gradient coils were constructed using a form and attached later. The gradient coils are located between the magnet and the radio frequency coil.

The RF coils have a quadrature-coil design with an x-directed saddle RF coil and a y-directed saddle coil. By driving the two at 90-degree phase difference, a rotating field is generated. Compared to linear polarization, the 90-degree phase difference results in a 3-dB improvement in received signal-to-noise ratio (SNR) and a 41% increase in RF field strength (B_1) for a given transmitter power. The coils were wound on 28.9 cm OD PVC using 0.635 cm copper refrigeration tubing. Where the coils crossed, one was flattened against the PVC (figure 4-8) and the other was flattened to the opposite side so that, despite overlapping, the coils were the same diameter. Resonating capacitors consisted of polyester film units that were hand selected to bring the two coils (x, y) to the same resonance frequency to within 2 kHz. The two saddle coils were constructed and mounted perpendicular to each other to avoid coupling. One turn of each resonant coil was connected to a coaxial driving cable using capacitive coupling.

Figure 4-8: The radio frequency coil was constructed using a quadrature design with x and y direction saddle coils and was wound on 28.9 cm plastic polyvinyl chloride (PVC) pipe.

The oil pump and water chiller were situated close to the magnet and were used in tandem as a cooling system for the electromagnet. Figure 4-9A shows the water chiller (CFT-75, Thermo Neslab LLC., Waltham MA, USA) used to circulated 20 °C tap water using a 0.635-cm diameter copper refrigeration tubing wound around the electromagnet and resting in the hydraulic fluid. The hydraulic fluid that was used as a cooling oil was circulated around the main and end windings of the electromagnet using the oil pump (figure 4-9B).

Figure 4-9: A) The Neslab CFT-75 water chiller was used to remove heat from the electromagnet oil bath. B) The oil pump was used to recirculate the oil to ensure that the electromagnet did not overheat.

The last piece of equipment used in the LF-MRI rhizotron system was a quadrature combiner/splitter, which was used to drive the quadrature RF coils. The combiner/splitter was constructed in-house from lumped inductors and capacitors (figure 4-10) and placed in-line between the Redstone console and the RF coils.

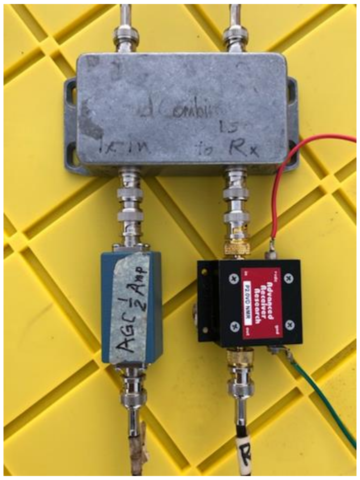

Figure 4-10: The combiner/splitter is used to drive the quadrature radio frequency coils.

4.2.3. LF-MRI Magnet Lift System

Two considerations during the design phase for the LF-MRI Rhizotron were the size and mobility of the electromagnet unit in the field. The operating weight of the electromagnet assembly (electromagnet coil, RF coil, Gradient coil, and coolant) was approximately 453.6 kg. To meet the mobility requirement, a lift system was designed to safely lift the electromagnet assembly for moving around an experimental site, and to precisely set the electromagnet assembly into an annular hole of removed soil around an intact column of soil and roots (figure 4-11).

Figure 4-11: The LF-MRI electromagnet assembly is placed in the annular shaped hole around the green plastic polyvinyl chloride (PVC) pipe, which is centered around a sorghum plant.

Two 92-cm long, 0.635-cm right angle guide rails were each welded to a steel rectangular tubing. These rails supported a 101-cm long I-beam which laid perpendicular to the guide rails and rested upon four 10-cm cast iron v-grove wheels -- two mounted at either end of the I-beam (figure 4-12). A tractor with a front-end loader system fitted with forks was used as the platform for the lift system, with the forks sliding into the rectangular frames supporting the guide rails. A one-ton I-beam walker was fitted on the lower flange of the I beam (figure 4-12A). The walker enabled the suspended electromagnet assembly to be moved left and right by pulling on the chain, so that the electromagnet assembly could be securely centered above the annular hole. Additionally, a one-ton chain hoist was attached to the I-beam walker to allow the electromagnet assembly to be raised and lowered by pulling a second chain. The chain hoist was secured to the electromagnet assembly by connecting eight nylon lifting straps to the end of the chain hoist (figure 4-12B).

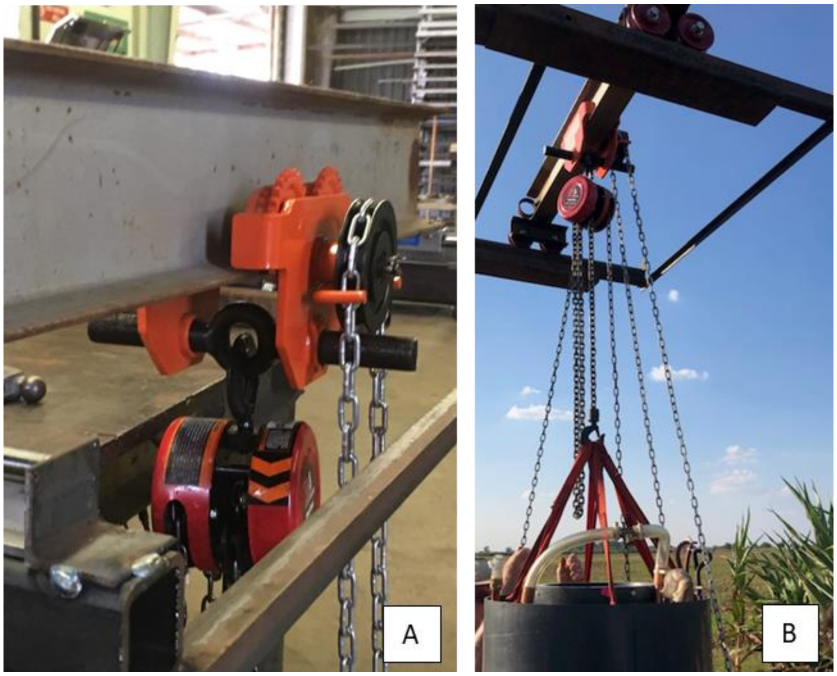

Figure 4-12: The MRI lift system utilized a chain hoist mounted on an I-beam walker. The I-beam was mounted on a set of rollers. This allowed the lift system to place the MRI anywhere inside an 8000 cm^2 area.

4.2.4. Field Data Collection

Field data collection was conducted at the Texas A&M AgriLife Research Field laboratory in Burleson County, Texas, USA. A bioenergy sorghum hybrid (TX08001, *Sorghum bicolor* (L.) Moench.) was planted to a depth of 2.5 cm with a row spacing of 76 cm in two soil types. A Weswood silt loam, a Udifluventic Haplustept with 25% clay and mixed minerology and a Belk clay, an Entic Hapludert with 49% clay and mixed minerology. Standard agronomic practices were employed for fertilization and cultivation. The root scans were collected at approximately 140 days after emergence.

The experimental phase of this work started in August with the image collection being conducted in late November of 2020. The time span for in-field measurement allowed the system to be tested under a range of maximum daytime temperatures (37.8 to 0.5 °C), along with the typical humidity, dust, and rain associated with field conditions.

The LF-MRI Rhizotron design requires that once the plant becomes taller than roughly 0.5m the above ground portion will have to be cut off, making most of the data collection a destructive test. The LF-MRI Rhizotron was designed to be used in two basic arrangements. For the *in situ* arrangement the sorghum plant is cut off at the soil surface, the electromagnet assembly was placed in an annular-shaped hole with the soil and root core in the center. For *ex situ* arrangement, the electromagnet assembly was placed on the ground while the sorghum plant was cut off at the soil surface and a sample core was collected and placed in the imaging zone.

For both configurations, a 25.4-cm diameter PVC pipe was pushed into the soil while centered around a sorghum plant. A hydraulic soil probe (Giddings Machine Company, Inc., Windsor, CO., USA) mounted on a one-ton dual wheeled pickup truck was used to push the PVC into the soil. The truck was anchored into the ground with two 20.32-cm diameter land screws that were 182.88-cm in length. For the first configuration, an annular shaped hole was excavated around the PVC pipe using a 66-cm diameter core constructed in-house, with an offset of the kelly-bar by 25.4 cm to allow a connection to the Giddings probe (figure 4-13). The probe was then used to cut a core centered on the PVC pipe, creating an annular hole around the 25-cm column of

PVC to a depth of 72 cm. The electromagnet assembly was inserted into the annular hole using the lift system described above.

Figure 4-13: The annular core was constructed of 16 gauge steel, with 1 in cold rolled steel supports. It was designed to be attached to a Giddings probe.

For *ex situ* root-scanning, the PVC is pushed into the soil using the hydraulic probe to a depth of 25.4 cm, and the PVC plus soil core was excavated. The core was left in the PVC and placed in the electromagnet assembly for data collection. Using this configuration, twelve cores were pulled and scanned in the field. The cores were then washed and the fresh root weight was recorded. The roots were dried at 96 °C for 48 hr and then weighted again, allowing a calculation for root water.

4.2.5. Imaging Sequence

After the electromagnet assembly and sample were positioned, three types of sequences were run. A Carr-Purcell-Meiboom-Gill (CPMG) [75] spin echo pulse sequence was used to measure T_2, and signal strength (M_0) for 0-D, 1-D, and 2-D scans. The spin-echo sequence used sixteen sequential spin echoes with an echo spacing of 7 ms; again, the timing was CPMG (figure 4-14). After each echo, any phase encoding gradient and frequency encoding gradient were rewound. Thus, each echo obtained the same line in k-space. The echoes were then averaged to improve the SNR.

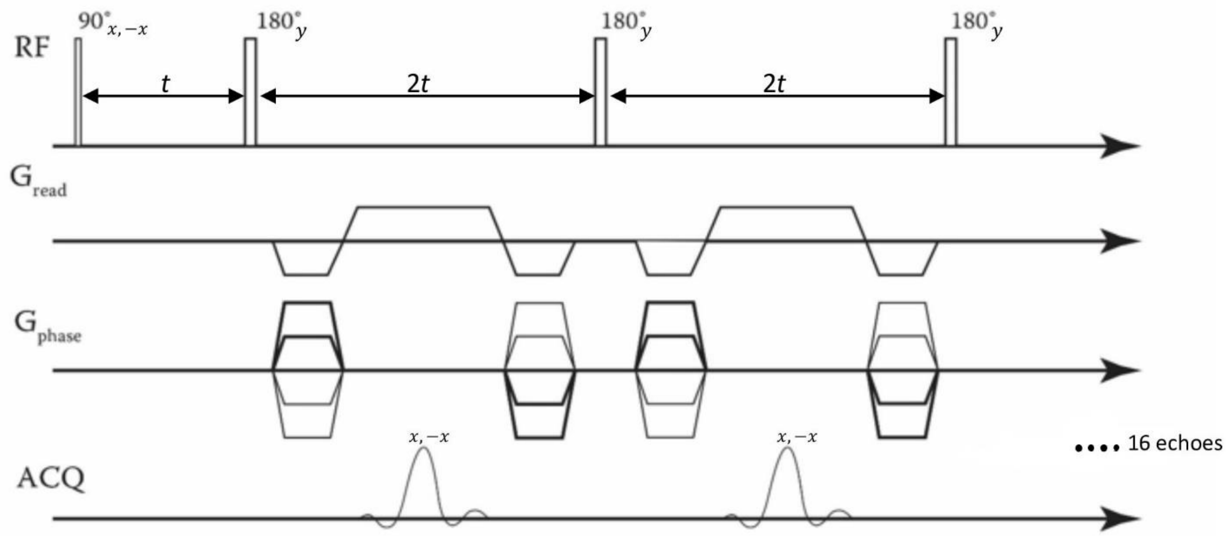

Figure 4-14: Pulse sequence for image generation uses Carr-Purcell-Meiboom-Gill (CPMG) pulse sequence that is fully rewound, both for phase encode and frequency read out. The subscripts refer to the phase of the radio frequency (RF) transmit, data acquisition. τ and 2 τ are RF pulse spacing. 16 echos were acquired and averaged together for each phase encode.

The first sequence used was a 0-D imaging sequence. For this sequence the signal strength M_0, which is proportional to the amount of hydrogen nuclear spins (^1H) present as water in the root sample, is collected with the gradients turned off. Thus, there is no spatial information. The 0-D image provides a measure of the root water present in the imaging zone.

The second sequence was a 1-D imaging sequence. This sequence provides an estimation of root water that is present down the soil profile using the z-gradient to provide the vertical spatial information. The 0-D and 1-D imaging sequences each took approximately thirty seconds to complete.

The last set of data collected was a series of 2-D image projections. For the 2-D image sequences, both the vertical and horizontal gradients were engaged to spatially encode the root water in the imaging zone, producing a 2-D projection image where all roots present in the imaging zone were projected onto a 2-D plane. In this sequence, eight 2-D projection images were collected, with each sequential image rotated by 22.5 degrees. This provided a full 180-degree view of the root system, chopped up into eight images. Because these images are 2-D projections, the images were then inverted to acquire the “back” 180 degrees, giving a full 360-degree visualization of the root system broken up into 16 individual images. Two hours and 16 minutes are required to acquire all eight 2-D projections.

After field data were collected, a system calibration scan was developed to convert pixel intensity to a known amount of water present in that pixel. To perform this calibration, a 1.27-cm inner diameter (ID) PVC pipe, 1-m long, was filled with 750 ml of tap water. The PVC pipe was placed inside the electromagnet imaging zone, and standard system parameters were set for a 2-D projection image. Data were collected using the same sequence mentioned above but with an increased last delay of 1s due to the longer T_1 of tap water. The output of this sequence was a single 2-D image projection. This 2-D projection displayed the pixel intensity produced for a measured amount of water placed in the PVC pipe. The calibration image was then scaled so that a pixel intensity of 1 was equal to 10 mm of fully relaxed water which is perpendicular to the image plane. Thus, the calibrated root water was calculated using the following equation with a calibrated LF-MRI data set;

$$Pixel\ water\ volume = pixel\ value * 10mm * pixel\ area\ (mm) * 0.001$$ Equation 2.

The calibration was then applied to the LF-MRI Rhizotron 1-D data set.

4.3. Results and Discussion

The *ex situ* Rhizotron scanning configuration was used to collect 0-D and 1-D data of eleven sets of root systems. We expected the 0-D and 1-D signal strength (M_0) to be colinear and a strong correlation between root water content and M_0. We also expected the T_2 relaxation times to be similar for 0-D and 1-D signal. Table 4-1 shows 0-D, 1-D, T_2 relaxation times, and calculated root water for sample number 2 to 12. Scans of Sample 1 were removed because of equipment errors. Root water was calculated by subtracting root dry weight from fresh weight. We expected that as root water increased the M_0 would also increase; however, the expected relationship was not consistent (table

4-1). Instead some samples, such as silt loam 4, had relatively low M_0 and high root water. While other samples, such as the clay 11, had a relatively high M_0 and small root water. It is worth noting that the high root water and low M_0 is the more common outcome.

Table 4-1: The tabulated results of the 0-D and 1-D signal strength, T_2 relaxation time, and calculated root water.

Sample Name	0-D signal strength (M_0)	T_2 for 0-D (ms)	1-D signal strength (M_0)	T_2 for 1-D (ms)	Root water (g)
Silt loam 2	23071	229.5	15939	204.0	462.0
Silt loam 3	13292	220.3	6356	133.4	376.6
Silt loam 4	11141	211.9	7928	185.4	332.2
Silt loam 5	10933	305.1	10047	313.3	154.5
Silt loam 6	16425	214.2	12934	200.7	223.9
Clay 7	9715	235.9	7541	216.5	161.0
Clay 8	20597	237.7	18654	223.5	248.1
Clay 9	36278	182.9	28825	182.1	399.4
Clay 10	18387	197.4	15945	189.9	246.8
Clay 11	47179	203.5	40217	200.7	182.2
Clay 12	12375	197.3	9477	191.3	525.7

The results found in table 4-1 are displayed graphically in figure 4-15. The plot of M_0 vs the root water shows only a weak relationship. There are several possible reasons, the first is an error in equipment set up. If the frequency of the electromagnet, which is set and controlled using the Redstone MRI console by adjusting several other parameters, is not adjusted correctly the RF coil will not collect the true signal and thus introduce some error to the system. A second possibility is that a portion of this error could have been due to environmental noise that is introduced into the system because of a reduced effectiveness in the electronic shimming of the magnetic field. During the boot-up procedure of the LF-MRI Rhizotron, the magnetic field must be shimmed. In a laboratory setting, this system shims quite well; however, in the field the process became more difficult because of environmental noise. As a result, the shimming was of lower quality and the signal was noisier. Future work in this area requires an experiment comparing root 0-D M_0 in a laboratory setting and an in-field experiment, which would allow a differentiation between the error introduced by the user (via poor settings) and environmental noise.

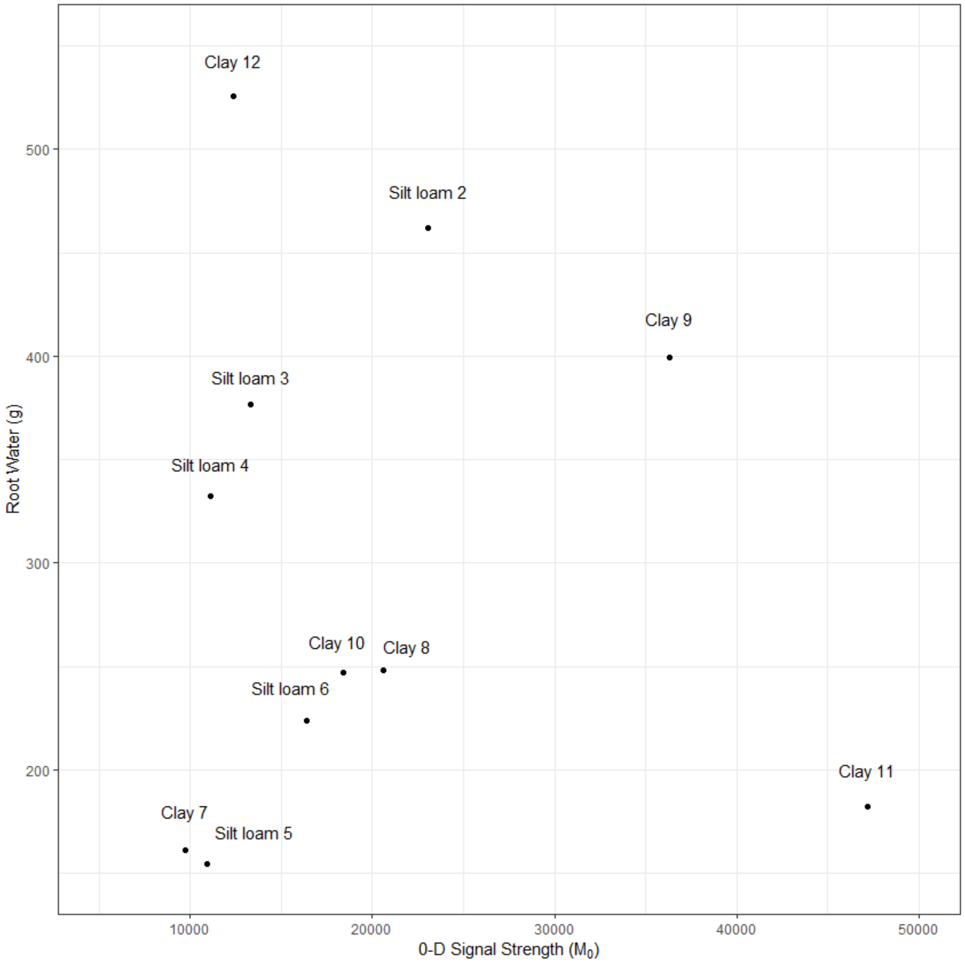

Figure 4-15: A weak relationship is displayed in this graph of 0-D signal strength vs. root water.

As with the 0-D, we expected a strong relationship between the 1-D M_0 and the root water. We also expected to be able to map the root water by depth using the z-gradient. We did find the 1-D and 0-D to be co-linear as expected, with the 1-D signal being smaller (figure 4-16B). The 1-D M_0 is only weakly related to the M_0, just like the 0-D results, with likely similar sources of error. Figure 4-16A shows the signal strength variation by depth. Figure 4-16A shows the vertical distribution of root water; however, because there is not a strong relationship between signal strength and root water content, we cannot turn this information into the vertical distribution of that root water or root biomass.

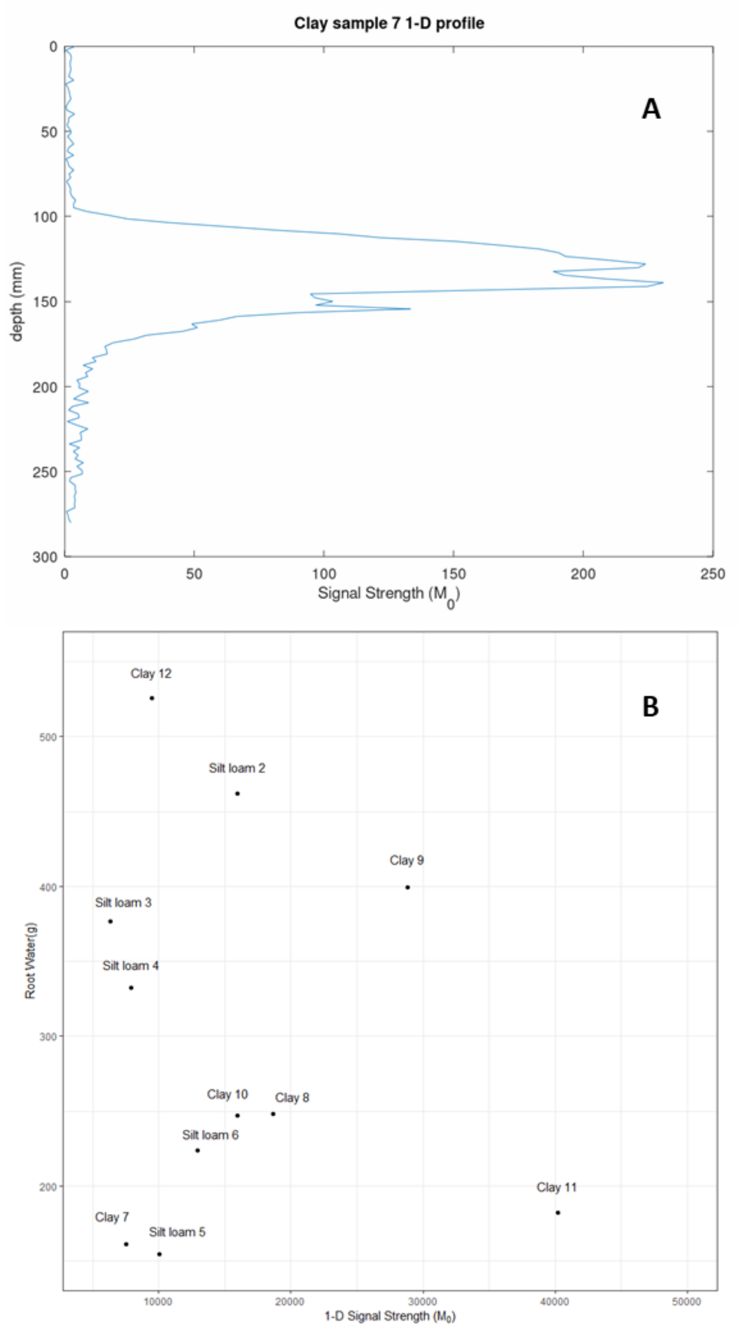

Figure 4-16: A) The root depth plot shows the root water signal by depth in cm on the y-axis, were the soil surfaces are at the top of the graph and the x-axis shows the 1-D signal strength (M_0). B) The plot of 1-D signal strength (M_0) vs the root water with each data point labeled by sample name.

We attempted to improve the relationship between M_0 and root water by calibrating the LF-MRI signal. The calibration used the 2-D image sequence and produced a calibrated and scaled image (figure 4-17) such that a pixel value of 1 represents 0.04 ml of water. We found that when we applied the calibration to the 0-D and 1-D data the calibration did not improve the relationship between M_0 and root water.

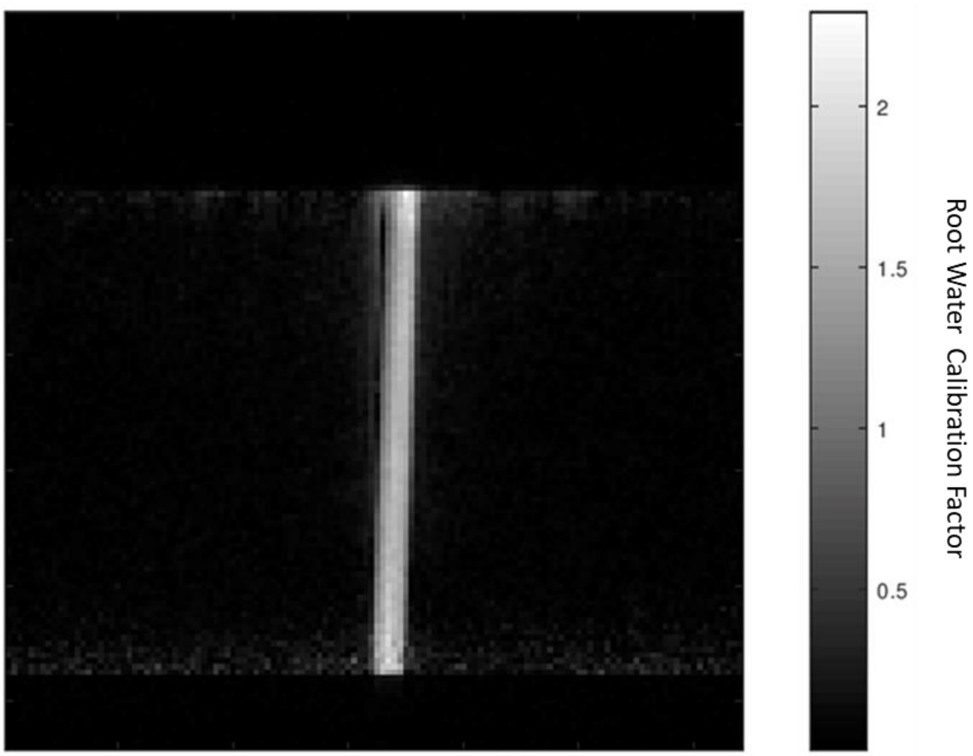

Figure 4-17: The calibration image of a PVC pipe filled with 750 ml of water. The pixel calibration factor multiplied by 10 * pixel area gives the water present in that pixel.

In addition to root biomass estimations, root system architecture is also of interest to root phenotyping. The 2-D projection images (figure 4-18) demonstrate the type of root system architecture that can be currently captured using the LF-MRI Rhizotron. These 2-D projection images were collected using the above ground LF-MRI Rhizotron configuration and took approximately 16.5 minutes per image, or 2 hours and 10 minutes to collect the 8 projections needed to create 360-degree view of the root system architecture. Figures 4-18A and 4.18B show samples # 4 and #6 from the Weswood silt loam soil while figures 4-18C and 4.18D show sorghum roots in the Belk clay using samples #8 and #10, respectively. In all cases, the image is the first in the series of 8 projection images. The FOV for these images are 280 mm x 280 mm, with an original matrix size of 128 x 128. The image matrix was then zero filled to 256 x 256 and is the size presented here. These 2-D images demonstrate that root architecture such as rooting angle, and root density at different depths is possible using this tool under field conditions.

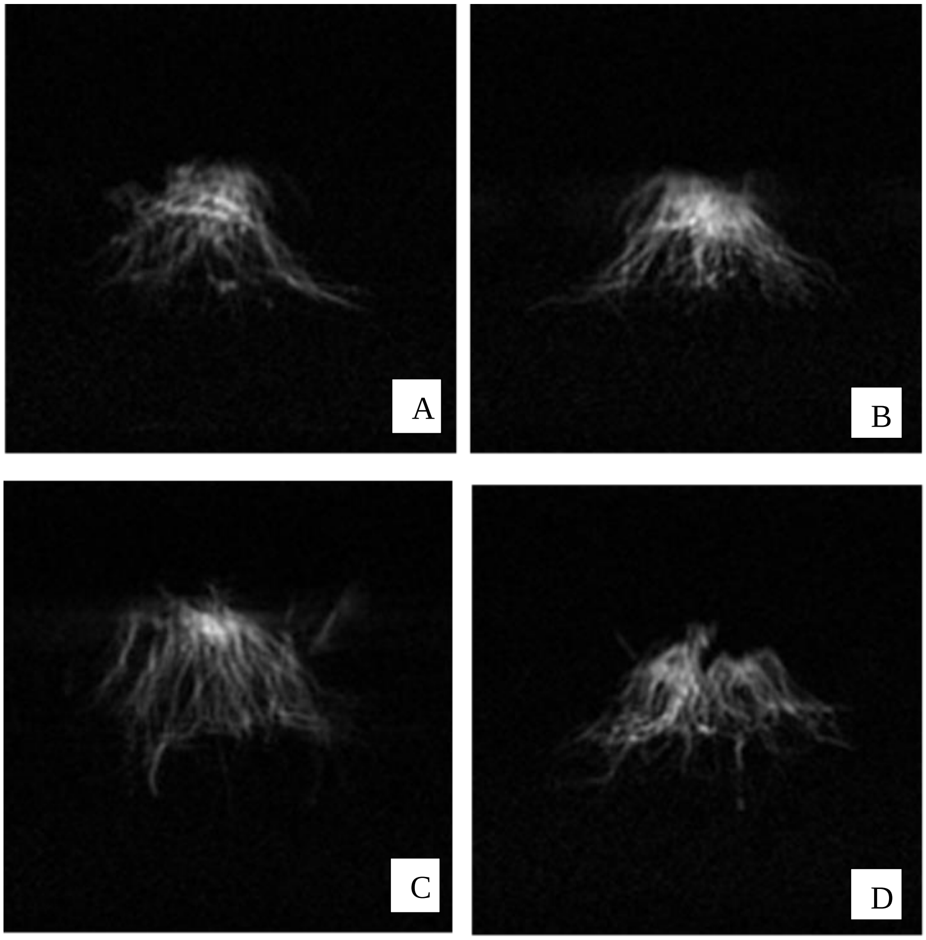

Figure 4-18: 2-D image projections of sorghum roots. This image has an in-plane resolution of 1.1 mm and each image takes approximately 16 minutes to complete. A) Is Weswood sample #4. B) is Weswood sample # 6. C) Is Belk clay sample #8, D) Is Belk clay sample #10.

We tested the LF-MRI Rhizotron using the in-ground configuration as well. However, when using the in-ground data collection method we found noise in the data from an unknown external source. This signal noise translated to artifacts and distortions in the image after image re-construction. Our best guess was that the noise was traveling through the ground and was produced by an electromagnetic source nearby. Because the goal of this method is to place the Rhizotron *in situ* (in the ground), and the *in situ* configuration requires a column of soil to be inside the electromagnet assembly, this effectively places the noise inside the RF coil with no obvious way to shield the system from this noise. We discovered that the noise was transient in the frequency space, and that by post processing the signal we were able to filter out some of the noise. The image sampling scheme was changed to reduce the number of replications of each line of data, and only produce four of the eight projection images at a time. A computer program was written in Octave [102] to compare each set of the four repeated measurements and remove any signal that was not found in all four replicates. This program operates on the theory that if a signal spike is present in all four replications, this spike is most likely to represent the true signal, if on the other hand that signal spike only shows up in few replications of the data then this event is most likely the noise signal and can be removed. After the MRI signal is cleaned the image can be constructed as before (figure 4-19). These images do have more noise present when compared to the data taken using the above ground configuration, indicating that the post processing needs more refinement.

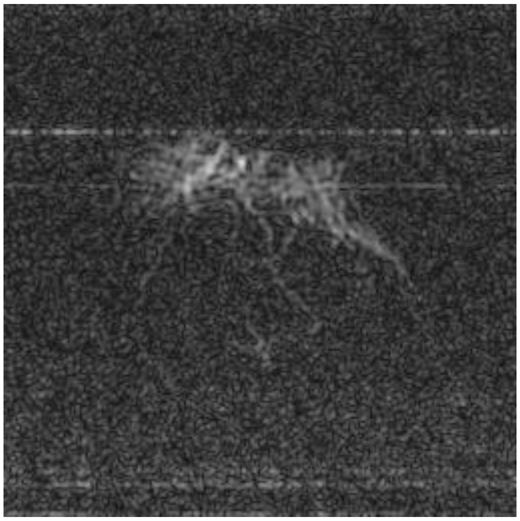

Figure 4-19: Root image collected in-ground from a Belk clay. You can see artifacts as well as random noise, but also still see some of the root structure.

After collecting the data, we attempted to measure the root length from the 2-D projection images. Typically, getting root length from images would require thresholding the image to convert the image to a binary, black and white, image. Then a segmentation is performed and the binary pixels are separated to create two images, one of the foreground (roots) and one of the background. After the thresholding and segmentation steps, a number of algorithms have been designed to measure root length. We attempted the thresholding and segmentation steps using several programing packages (EZ-Rooting, Dynamic roots, Image J, GIARoots, DART) and found that these programs could identify the total root mass easily using both an automatic thresholding or user defined methods. However, the dense root population due to the background roots and foreground roots being in the same plane, and the coarse image resolution made identifying individual roots to trace for root length not possible (figure 4-20).

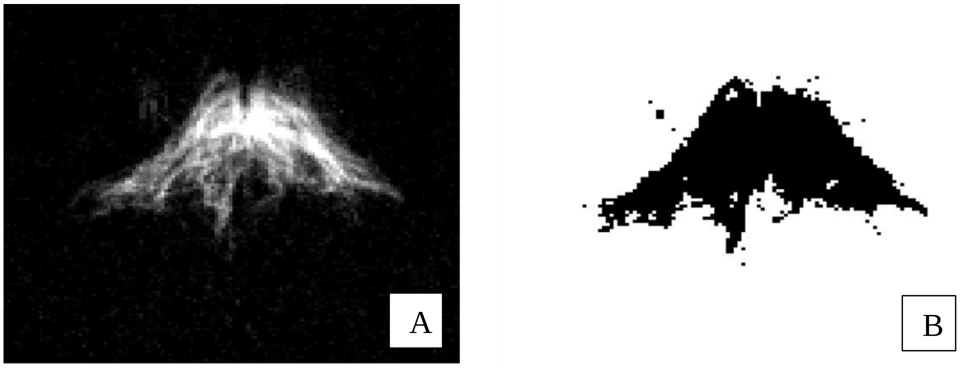

Figure 4-20:A) The 2-D projection image from Clay sample #9, B) The processed 2-D projection image after image thresholding and segmentation

4.4. Conclusions

We have demonstrated in this work the design and deployment of a low field magnetic resonance imaging rhizotron that is suitable for in field scanning in an agricultural field setting. The low field system allows the MRI to operate in high clay soils and is capable of generating root data in the field either by pulling large cores and imaging them above ground or by excavation and placing the LF-MRI in the ground around a plant. The system is light enough to be moved around the field and uses two portable power supplies. Using both the *in situ* and *ex situ* sampling configurations we demonstrated the ability to collect root system architecture images for root metric analysis. The 0-D, and 1-D data collected in this experiment for measuring root metrics displayed unexpectedly weak relationships. The lack of relationship between LF-MRI M_0 and the measured root water is likely caused by a combination of user error and poor magnetic field shimming. This demonstrate that more work needs to be accomplished to make this LF-MRI system user friendly and available for a plant breeding application.

We have developed a clear path forward that includes different root-water calibration methods for segmentation of the signal into root biomass, 3D imaging, and replacing the current resistive magnet with a superconducting magnet.

The first track in continuing this work is in creating a systematic tuning procedure for the LF-MRI Rhizotron and to improve the model of the relationship between the signal and root biomass. The LF-MRI is tuned each time it is turned on or a new type of scan is conducted. The parameters for tuning this system under field conditions (magnet frequency, shim, RF gain, P90, P180) are not well understood. A systematic study of known volume of water under similar field conditions will be used to create a user guide to tune the system and better repeatability. We know that a relationship exists between signal strength and root water (see Appendix B) under laboratory conditions. We believe that by incorporating the T_2 relaxation time information we can improve M_0 and root water relationship for field scans to measure root biomass. This will help create a repeatable system, allowing image data to be compared over-time and to other MRI systems.

The second track for improvement is to develop an in-sample calibration system to convert the signal information to concrete units that can be compared with other systems easily. By developing a calibration technique that uses a known amount of water that is placed in or near the sample before the scan (known as a fiducia). We propose that using a vial of water with a known volume and relaxation time, can be placed in the sample to fill this role. We believe this method will be more robust than the calibration presented in this work by providing each sample with its own fiducia, making each sample complete and independent of any other scans.

The third track is to further develop the in-ground post processing system to improve the SNR and artifact removal. This will allow a broader range of experiments to be explored such as scanning the same plant multiple times through its development stages in natural soils.

The fourth track is to improve the quality of the information by changing the resistive magnet for a super conducting magnet that uses liquid nitrogen cooling. This change allows the magnet assembly to be lighter, operate at higher magnetic field strength. This translates to faster scans, or higher resolutions. Preliminary work with a super conducting magnet shows 3-D scans can be conducted in approximately 1 hour. 3-D imaging gives expanded flexibility to data processing and visualization in approximately.

We believe that addressing system set up, calibration, in-ground scans, and magnet design will broaden the range of applications that the LF-MRI Rhizotron can perform and will solve the issues that arose during the research presented here.

5. SUMMARY

Field phenotyping allows researchers and producers to make plant-breeding and agronomic decisions based on plant characteristics of importance. The goal of the research presented in this dissertation has been to develop and improve measurements of specific above- and below-ground plant characteristics. Specifically, the methods concern radiometric calibration methods for UAV remote sensing of plant reflectance and a novel system for in situ root imaging.

5.1. UAV Camera Calibration

Regarding UAV remote sensing, a fixed exposure camera calibration method with in-field calibration targets was compared to autoexposure calibration using a single calibration target. The comparison demonstrated a significant difference between the two methods. The fixed exposure method produced significantly less error based on a band to band comparison (~50% lower) and also less error when those bands were then used to create the vegetative index, VARI (~50% lower). The autoexposure method, however, did use a larger amount of the camera's dynamic range in this study. A Monte Carlo simulation was constructed to understand how the difference in error would affect management decision making using either of these systems. The results showed that the fixed exposure correctly classified management zones 82% of the time, compared to 67% for the autoexposure. This study showed that using in-field calibration targets along with fixed exposure settings provides much more accurate reflectance data, a finding that is important for decision making by both researchers and producers.

5.2. LF-MRI Rhizotron

Regarding *in situ* root imaging, two systems were developed and tested. The 8cm bore LF-MRI system was designed and constructed to test the technology's ability to image roots in moderate to high clay soils. Preliminary work showed that soil water and root water relaxation times were sufficiently different to allow a good contrast for root detection and visualization. With this information, an 8cm bore laboratory LF-MRI system was developed and tested across three soil types (Weswood silt loam, Belk clay, Houston black clay), producing 2-D projection images at three different resolutions (0.625, 1.25, 1.74 mm), and in all three soils.

A field deployable 28-cm bore LF-MRI Rhizotron was designed to be utilized under field conditions. The system was tested in the field in two soil types, Weswood silt loam and Belk clay. Two LF-MRI Rhizotron scanning configurations were tested, the first was an *ex situ* scan using 25 cm diameter by 25 cm long cores. The results of this configuration demonstrated that data collection and visualization are possible in the field. The second scanning configuration required an annular hole to be dug and the LF-MRI Rhizotron to be placed *in situ.* The results of this configuration showed significant noise in the measurement signal resulting in image artifacts. By modifying the data collection approach to compare data replications and remove information that is not present in all four replicates, we were able to reconstruct an image of the roots. While the new procedure does allow visualization of the root system it does still have image artifacts present and needs refinement to produce a higher quality image. We believe that further refinement of the system and optimization of user procedures could produce a practical tool for either *ex situ* or *in situ* nondestructive root system architecture visualization and measurement.

REFERENCES

[1] A. Borem and S. C. K. Milach, "Plant breeding in the turn of the millennium," *Brazilian Archives of Biology and Technology*, vol. 3, pp. 1-7, 1998.

[2] U. N. FAO, "2018 The state of food secrutiy and nutrition in the world," United Nations, [Online]. Available: http://www.fao.org/state-of-food-security-nutrition/en/. [Accessed 1 April 2018].

[3] International Society of Precision Agriculture, "ISPA," [Online]. Available: ispag.org. [Accessed 4th April 2020].

[4] J. V. Stafford, "Implementing precision agriculture in the 21st century," *Journal of Agriculture Engineering Research*, pp. 267-275, 2000.

[5] V. L. Mulder, S. d. Bruin, M. E. Schaepman and T. R. Mayr, "The use of remote sensing in soil and terrain Mapping- A review," *Geoderma*, vol. 162, pp. 1-19, 2011.

[6] K. Temizel, "Mapping of some soil properties due to precision irrigation in agriculture," *Agronomy Research*, vol. 14, pp. 959-966, 2016.

[7] T. A. Thomasson and R. Sui, "Mississippi cotton yield monitor: Three years of field test results," *Applied Engineering in Agriculture*, vol. 19, no. 6, pp. 631-636, 2003.

[8] N. R. Peralta, Y. Assefa, J. Du, C. J. Barde and I. A. Ciampitti, "Mid-season high resonlution satellite imagery for forecasting site specific corn yield," *Remote Sensing*, vol. 8, no. 848, pp. 1-16, 2016.

[9] J. L. Araus and J. E. Cairns, "Field high-throughput phenotyping: New crop breeding frontier," *Trends in Plant Science*, vol. 19, no. 1, pp. 52-61, 2014.

[10] V. Weber, J. L. Araus, J. E. Cairns, C. Sanchez, A. E. Melchinger and E. Orsini, "Predition of grain yield using reflectance spectra of canopy and leaves in maize plants grown under different water regimes," *Field Crops Research*, vol. 128, pp. 82-90, 2012.

[11] S. Kefauver, R. Vicente, O. Vergara-Diaz, J. A. Fernandez-Gallego, S. Kerfal, A. Lopez, J. P. E. Melichar, M. D. Serret Molins and J. L. Araus, "Comparative UAV and field phenotypig to assess yield and nitrogen use efficiency in hybrid and vonventional barley," *Frontiers in Plant Science*, vol. 8, 2017.

[12] J. Xue and B. Su, "Significant remote sensing vegetation indicies: A review of developments and applications," *Journal of Sensors*, vol. 2017, pp. 1-17, 2017.

[13] R. Ishimwe, K. Abutaleb and F. Ahmed, "Applications of thermal imaging in agriculture: A review," *Advances in Remote Sensing*, vol. 3, pp. 128-140, 2014.

[14] M. Wojtowixz, A. Wojtowicz and J. Piekarczyk, "Applications of remote sensing methods in agriculture," *Comunications in Biometry and Crop Science*, vol. 11, no. 1, pp. 31-50, 2016.

[15] J. P. Lynch, "Rightsizing root phenotypes for drought resistance," *Jornal of Experimental Botany*, vol. 69, no. 13, pp. 3279-3292, 2018.

[16] J. Zhu, P. A. Ingram, P. N. Benfey and T. Elich, "From lab to field, new approaches to phenotyping root sytem architecture," *ScienceDirect*, vol. 14, pp. 310-317, 2011.

[17] J. Lynch, "Root architecture and plant productivity," *Plant Physiology,* vol. 109, pp. 7-13, 1995.

[18] E. D. Rogers and P. N. Benfey, "Regulation of plant root system architecture: implications for crop andvancement," *ScienceDirect,* vol. 32, pp. 93-98, 2015.

[19] C. Atzberger, "Advances in remote sensing of agricultur: Context description, existing operational monitoring systems and major information needs," *Remote Sensing,* vol. 5, pp. 949-981, 2013.

[20] J. Batz, M. A. Mendez-Dorado and J. A. Thomasson, "Imaging for high throughput phenotyping in energy sorghum," *Jorunal of Imaging,* vol. 2, no. 4, pp. 1-12, 2016.

[21] C. Nansen, A. J. Sidumo, X. Martini, K. Stefanova and J. D. roberts, "Reflectance-based assessment of spider mite "bio-response" to maze leaves and plant potassium content in different irrigation regimes," *Computers and Electronics in Agriculture,* vol. 97, pp. 21-26, 2013.

[22] J. Penuelas, J. A. Gamon, A. L. Fredeen, J. Merino and C. B. Field, "Reflectance indicies associated with physiological changes in nitrogen and water limited sunflower leaves," *Remote Sensing of Enviornment,* vol. 48, no. 2, pp. 135-146, 1994.

[23] J. Zhang, C. Yang, H. Song, W. C. Hoffmann, D. Zhang and G. Zhang, "Evaluation of an Airborne remote sensing platform consisting of two consumer grade cameras for crop indentification," *Remote Sensing,* vol. 8, no. 3, pp. 1-23, 2016.

[24] A. Brook and E. B. Dor, "Supervised vicarious calibration (SVC) of hyperspectral remote-sensing data," *Remote Sensing of Environment,* vol. 115, pp. 1543-1555, 2011.

[25] G. M. Smith and E. J. Milton, "The use of the emperical line method to calibrate remotely sensed data to reflectance.," *International Journal of Remote Sensing,* vol. 20, no. 13, pp. 2653-2662, 1999.

[26] G. Guyot and X. F. Gu, "Effect of radiometric corrections on NDVI-determined from Spot- HRV and Landsat-TM data," *Remote Sensing of Environment,* vol. 49, pp. 169-180, 1994.

[27] J. C. Price, "Calibration of satellite radiometers and the comparison of vegetation indicies," *Remote Sensing of Environment,* vol. 21, no. 15, pp. 15-27, 1987.

[28] R. Muller, "Calibration and verification of remote sensing intstruments and observations," *Remote Sensing,* vol. 6, pp. 5692-5695, 2014.

[29] N. Yu, L. Li, N. Schmitz, L. F. Tian, J. A. Greenberg and B. W. Diers, "Development of methods to improve soybean yiedls estimation and predict plant maturity with an unmanned aerial vehicle based platform," *Remote Sensing of Environment,* vol. 187, pp. 91-101, 2016.

[30] K. Anderson and K. J. Gaston, "Lightweight unmanned aerial vehicles will revolutionize spatial ecology," *Frontiers in Ecology and the Enviornment,* vol. 11, no. 3, pp. 138-146, 2013.

[31] D. Giordan, M. A., R. Remondino and F. Nex, "Use of unmanned aerial vehicles in monitoring application and management of natural hazards," *Geomatics, Natural Hazards and Risk*, vol. 8, no. 1, pp. 1-4, 2017.

[32] J. Everaerts, "PEGASUS – Bridging the gap between airborne and spaceborne remote sensing.," in *New Strategies for European Remote Sensing*, Dubrovnik, 2018.

[33] N. Shakoor and T. C. Mockler, "High throughput phenotyping to accelerate crop breeding and monitoring of diseases in the field," *Current Opinion in Plant Biology,* vol. 38, pp. 184-192, 2017.

[34] C. Frankenberg, J. b. Fisher, J. Worden, G. Badgley, S. S. Saatchi, J.-E. Lee, G. C. toon, A. Butz, M. Jung, A. Kuze and T. Yokota, "New global observations of the terrestrial carbon cycle from GOSAT: Patterns of plant fluorescence with gross primary productivity," *Geophysical Research Letters*, vol. 38, no. 17, pp. 1-6, 2011.

[35] A. Matese, P. Toscano, S. F. D. Genaro, L. Genesio, F. P. Vaccari, J. Primicerio, C. Belli, A. Zaldei, R. Bianconi and B. Gioli, "Intercomparison of UAV, aircraft and satellite remote sensing platfomrs for precision viticulture," *Remote Sensing*, vol. 7, no. 3, pp. 2971-2990, 2015.

[36] Q. Weng, "Land use change analysis in the Zhujiang Delta of China using satellite remote sensing, GIS and stochastic modelling," *Journal of Environmental Mangagment*, vol. 64, no. 3, pp. 273-281, 2002.

[37] S. I. Corp., "WorldView-2 Satellite Sensor," 1 June 2018. [Online]. Available: https://www.satimagingcorp.com/satellite-sensors/worldview-2/.

[38] W. W. M. LLC, "Land info," 1 June 2018. [Online]. Available: http://www.landinfo.com/satellite-imagery-pricing.html.

[39] NASA, "Landsat Science," 9 August 2017. [Online]. Available: https://landsat.gsfc.nasa.gov/landsat-8/landsat-8-overview/.

[40] AirBus, "intelligence-aribusds.com," 1 January 2019. [Online]. Available: www.intelligence-airbusds.com/file/pmedia/public/r48725_9_airbuds_intelligence_pricelist_1.1.19.pdf. [Accessed 15 July 2020].

[41] C. Yang, "Aerial imaging with manned aircraft for precision agriculture," *Resource Engineering and Technology for a Sustainable World*, pp. 25-27, 5 July 2016.

[42] Y. Shi, Thomasson, J. Alex, C. Yang, D. Cope and C. Sima, "A case study of comparing radiometrically calibrated reflectance of an image mosaic from unmanned aerial system with that of a single image from manned aircraft over a same area," in *Autonomous Air and Ground Sensing Systems for Agricultural Optimization and Phenotyping II*, Anaheim, 2017.

[43] S. Sankaran, L. R. Khot, C. Z. Espinoza, S. Jarolmasjed, V. R. V. G. J. Sathuvalli, P. N. Miklas, A. H. Carter, M. O. Pumphrey, N. R. Knowles and M. J. Pavek, "Low-altitude, high-resolution aerial imaging systems for row and field crop phenotyping: A Review," *European Journal of Agronomy*, vol. 70, pp. 112-123, 2015.

[44] U. S. D. o. Transportation, "FAA," United States of America, 3rd July 2018. [Online]. Available: http://www.faa.gov/news/fact_sheets/news_story.cfm. [Accessed 21st June 2020].

[45] H. Zheng, T. Cheng, D. Li, X. Zhou, X. Yao, Y. Tian, W. Cao and Y. Zhu, "Evaluation of RGB, color infrared and multispectral images acquired from unmanned aerial systems for the estimation of nitrogen accumulation in rice.," *Remote Sensing,* vol. 10, no. 824, pp. 1-17, 2018.

[46] R. Ludovisi, F. Rauro, R. Salvati, S. Khoury, G. S. Mugnozza and A. Harfouche, "UAV based thermal imaging for high throughput field phenotyping of black poplar response to drought," *Frontiers in Plant Science,* vol. 8, pp. 1684-1699, 2017.

[47] J. C. Padro, F. J. Munoz, L. A. Avila, L. Pesquer and X. Pons, "Radiometric correction of Landsat-8 and Sentinel-2A scenes using drone imagery in synergy with field spectroradiometry," *Remote Sensing,* vol. 10, pp. 1-26, 2018.

[48] C. Wang and S. W. Myint, "A simplified emperical line method of radiometric calibration for small unmanned aircraft systems-based remote sensing," *Journal of Selected Topics in Applied Earth Observations and Remote Sensing,* vol. 8, no. 5, pp. 1876-1885, 2015.

[49] S. D. Pozo, P. Rodriguez-Gonzalvez, D. Hernadez and B. fleipe, "Vicarious radiometric calibration of a multispectral camera on board unmanned aerial system," *Remote Sensing,* vol. 6, pp. 1948-1937, 2014.

[50] F. Iqbal, A. Lucieer and K. Barry, "Simplified radiometric calibration for UAV-mounted mulispectral sensor," *European Journal of Remote Sensing,* vol. 51, no. 1, pp. 301-313, 2018.

[51] M. Mafanya, P. Tsele, J. O. Botai, P. Manyama, G. J. Chirima and T. Monate, "Radiometric calibration framework for ultra-high-resolution UAV-derived orthomosaics for large scale mapping of invasive alien plants in semi-arid woodlands: Harrisia pomanensis as a case study," *International Journal of Remote Sensing,* pp. 1-22, 2018.

[52] A. S. Laliberte, M. A. Gogorth, C. M. Steele and A. Rango, "Multispectral Remote Sensing from Unmanned Aircraft: Image Processing Workflows and Applications for Rangeland Environments," *Remote Sensing,* vol. 3, pp. 2529-2551, 2011.

[53] J. M. McKinion, J. N. Jenkins, J. L. Willers and A. Zumanis, "Spatially variable insecticide applications for early season control of cotton insect pests," *Computers and Electronics in Agriculture,* vol. 67, pp. 71-79, 2009.

[54] J. L. Willers, J. N. Jenkins, W. Ladner, P. D. Gerard, D. L. Boykin, K. B. Hood, P. L. Mckibben, S. A. Samson and M. M. Bethel, "Site specific approaches to cotton insect control. Sampling and remote sensing analysis techniques," *Precision Agriculture,* vol. 6, pp. 431-452, 2005.

[55] J. M. Mckinion, J. N. Jenkins, J. L. Willers and A. Zumanis, "Spatially variable insecticide applications for early season control of cotton insect pests," *Computers and Electronics in Agriculture,* vol. 67, pp. 71-79, 2009.

[56] P. Armengaud, K. Zambaux, A. Hills, R. Sulpice, P. J. Pattison, M. R. Blat and A. Amtmann, "EZ-Rhizo: integrated software for the fast and accurate measurment of root system architecture," *The Plant Journal,* vol. 57, pp. 945-956, 2009.

[57] S. J. Mooney, T. P. Pridemore, H. J. and M. J. Bennett, "Developing X-ray computer tomography to non-invasively image 3-D root system architecture in soil," *Plant and Soil,* vol. 352, pp. 1-22, 2012.

[58] X. Zhou and X. Luo, "Advances in non-destruct measurment and 3-D visualization methods for plant roots based on machine vision," in *2nd International Conference on Biomedical Engineering and Informatics*, Tianjin, 2009.

[59] S. Trachsel, S. M. Kaeppler, K. M. Brown and J. P. Lynch, "Shovelomics: high throughput phenotyping of maize (Zea mays L.) root architecture in the field.," *Plant and Soil,* vol. 341, pp. 75-87, 2011.

[60] A. P. Araujo, A. M. Fernades, F. Y. Kubota, F. C. Brasil and M. G. Teixeira, "Sample size for measurement of root traits on common bean by image analysis," *Pesquisa Agropecuaria Brasileria,* vol. 39, pp. 313-318, 2004.

[61] R. J. Flavel, C. N. Guppy, S. M. Rabbi and I. M. Young, "Non-destructive quantification of cereal roots in soil using high-resolution x-ray tomography," *Journal of Experimental Botany,* vol. 63, pp. 2503-2511, 2012.

[62] R. J. Flavel, C. N. Guppy, S. M. Rabbi and I. M. Young, "An image processing and analysis tool for identifying and analyzing complex plant root systems in 3-D soil using non-destructive analysis: Root1," *PLOS ONE,* vol. 10, pp. 1-18, 2017.

[63] J. A. Lafond, L. Han and P. Duiteul, "Concepts and analyses in the CT scanning of root systems and leaf canopies: a timely summary," *Frontiers in Plant Science,* vol. 6, pp. 1-7, 2015.

[64] J. A. Atkinson, P. M. P., M. J. Bennett and D. M. Wells, "Uncovering the hidden half of the plant using new advances in root phenotyping," *ScienceDirect*, vol. 55, pp. 1-8, 2019.

[65] S. Jahnke, M. I. Menzel, D. Dusschoten, G. W. Roeb, J. Buhler, S. Minwuyelet, P. Blumler, V. M. Temperton, T. S. M. Hombach, S. Beer, M. Khodaverdi, K. Ziemons, H. H. Coenen and U. Schurr, "Combined MRI-PET dissects dynamic changes in plant structures and functions," *The Plant Journal*, vol. 59, pp. 634-644, 2009.

[66] A. Koch, F. Meunier, J. Vanderborght, S. Garre, Pohlmeier and J. M. A., "Functional-structrual root system model validation using a soil MRI experiment," *Journal of Experimental Botany,* vol. 70, pp. 2797-2809, 2019.

[67] R. Metzner, D. Dusschoten, J. Buhler, U. Schurr and S. Jahnke, "Belowground plant development measured with magnetic resonance imaging (MRI): exploiting the potential for non-invasive trait quantification using sugar beet as a proxy," *Frontiers in Plant Science*, vol. 5, pp. 1-11, 2014.

[68] L. D. Hall, M. H. G. Agmin, M. Sanda, J. Votrubova, K. S. Richards, R. J. Chorley and M. Cislerova, "MR properties of water in saturated soils and resulting loss of

MRI signal in water content detection at 2 tesla.," *Geoderma,* vol. 80, pp. 431-448, 1997.

[69] J. Votrubova, M. Sanda, M. Cislerova, M. H. G. Amin and L. D. Hall, "The relationship between MR parameters and the water content in packed samples of two soils," *Geoderma,* vol. 95, pp. 267-282, 2000.

[70] R. E. Prebble and J. A. Currie, "Soil Water measurement by a row resolution nuclear magnetic resonance technique.," *Journal of Soil Science,* vol. 21, pp. 273-288, 1970.

[71] H. H. Rogers and P. A. Bottomly, "In situ nuclear magnetic resonance imaing of roots: influence of soil type ferromagnetic particl content and soil water," *Agronomy Journal,* vol. 79, pp. 957-965, 1987.

[72] D. Pfugfelder, R. Metzner, D. V. Dusschoten, R. Reichel, S. Jahnke and R. Koller, "Non-invasive imaging of plant roots in different soils using magnetic resonance imaging (MRI)," *Plant Methods,* vol. 13, pp. 1-9, 2017.

[73] D. Dusschoten, R. Metzner, J. Kochs, J. A. Postma and D. Pflugfelder, "Quantitative 3D analysis of plant roots growing in soil using magnetic resonance imaging," *Plant Physiology,* vol. 170, pp. 1176-1188, 2016.

[74] R. Brown, Y. Cheng, M. Haacke, M. Thompson and R. Venkatensan, Magnetic resonance imaging: physical principles and sequence design., Wiley and Sons, 2014.

[75] E. Fukushima and S. B. W. Roeder, Experimental pule NMR: a nuts and bolts approach, Boco Raton: CRC Press, 1982.

[76] P. Callaghna, Principles of nuclear magnetic resonance microscopy, Oxford: Oxford University Press, 1994.

[77] J. P. Hornak, The basics of NMR, http://www.cis.rit.edu/htbooks/nmr/index.html, 1997.

[78] H. Ayalew, X. Ma and G. Yang, "Screening wheat (Triticum spp) genotypes for root length under contrasting water regimes: potential sources of variability for drought resistance breeding," *Journal of Agronomy and Crop Science,* vol. 201, pp. 189-194, 2015.

[79] B. A. Fenta, S. E. Beebe, K. J. Kunert, J. D. Burridge, K. M. Barlow, J. P. Lynch and C. H. Foyer, "Field phenotyping of soybean roots for drought stress tolerance," *Agronomy,* vol. 4, no. 3, pp. 418-435, 2014.

[80] T. Garnett, V. Conn and B. N. Kaiser, "Root based approaches to improving nitrogen use effieciency in plants," *Plant, Cell and Environment,* vol. 32, no. 9, pp. 1272-1282, 2009.

[81] K. Paustian, N. Campbell, C. Dorich, E. Marx and A. Swan, "Assessment of potential greenhouse gas mitigation from changes to crop root mass and architecture," United States of America Department of Engergy ARPA-E, January 2016. [Online]. Available: https://arpa-e.energy.gov/?q=publications/assessment-potential-greenhouse-gas-mitigation-changes-crop-root-mass-and-architecture. [Accessed 13 August 2020].

[82] G. C. Bagnall, N. Koonjoo, S. Altobelli, M. Conradi, E. Fikushima, D. O. Kuethe, J. E. Mullet, H. Neely, W. L. Rooney, K. Stupic, B. Weers, B. Zhu, M. S. Rosen and C. Morgan, "Low field magnetic resonance imaging of roots in intact clayey and silty soils," *Geoderma,* vol. 370, 2020.

[83] A. Henry, V. R. P. Gowda, R. O. Torres, M. L. L. and R. Serraj, "Variation in root system architecture and drought response in rixe (Oryzz Sativa): phenotyping of Oryza SNP panel in rainfed lowland fields," *Field Crops Research,* vol. 120, pp. 205-214, 2011.

[84] M. Kano-Nakata, T. Nakamura, S. Mitsuya and A. Yamauchi, "Plasticity in root system architecture of rice genotypes exhibited under different soil water distribution in soil profile," *Plant Production Science,* vol. 22, no. 4, pp. 501-509, 2019.

[85] L. Lopez-Bacio, A. Cruz-Ramierez and L. Herrera-Estrella, "The role of nutrient avaliblity in regulating root architecture," *Current Opinion in Plant Biology,* vol. 6, no. 3, pp. 280-287, 2003.

[86] A. Paez-Garcia, C. M. Motes, W. Scheible, R. Chen, E. B. Balancaflor and M. J. Montereos, "Root traits and phenotyping strategies for plant improvment," *Plants,* vol. 4, pp. 334-355, 2015.

[87] A. Wasaya, X. Zhang, Q. Fang and Z. Yan, "Root phenotyping for drought tolerance: a review," *Agronomy,* vol. 8, pp. 241-260, 2018.

[88] L. T. Koevoets, J. H. Venema, J. T. M. Elzenga and C. Testerink, "Roots withstanding their environmentL exploiting root systems architecture response to abiotic stress to improve corp tolerance," *Frontiers in Plant Science,* vol. 7, 2016.

[89] L. Ma, Y. Shi, O. Siemianowski, B. Yuan, T. Egner, S. V. Mirnezami, K. R. LInd, B. Ganapathysubramanian, V. Venditti and L. Cademartiri, "Hydrogel based transparent soils for root phenotyping in vivo.," *Proceedings of the National Academy of Science of the United States of America,* vol. 116, no. 2, 2019.

[90] L. Pingault, P. Zogli, J. Brooks and M. Libault, "Enhancing phenotyping and molecular analysis of plant root systems using ultrasound aeroponic technology," *Current Protocols in Plant Biology,* vol. 3, no. 4, 2018.

[91] T. E. Grift, J. Novais and M. Bohn, "Highthroughput phenotyping technology for maize roots," *Biosystem Engineering,* vol. 110, pp. 40-48, 2011.

[92] A. Bucksch, J. Burridge, L. M. York, A. Das, E. Nord, J. S. Weitz and J. P. Lynch, "Image based high-throughput field phenotyping of crop roots," *Plant Physiology,* vol. 166, no. 2, pp. 470-486, 2014.

[93] C. M. Iversen, M. T. Murphy, M. F. Allen, J. Childs, D. M. Eissenstat, E. A. Lilleskov, T. M. Sarjala, V. L. Sloan and P. F. Sullivan, "Advancing the use of minirhizotrons in wetlands," *Plant and Soil,* vol. 352, pp. 23-39, 2012.

[94] O. Chloupek, "Evaluation of the size of plant root system using its electrical capacitance," *Plant and Soil,* vol. 48, no. 2, pp. 525-532, 1997.

[95] R. Messmer, Y. Frachebound, M. Banziger, P. Stamp and J. Ribaut, "Drought stress and tropical maize: QTLs for leaf greenness, plant senescence, and root capacitance.," *Field Crops Research,* vol. 124, no. 1, pp. 93-103, 2011.

[96] A. P. Wasson, G. J. Rebetzke, J. A. Kirkegaard, J. Christopher, R. A. Richards and M. Watt, "Soil coring at multiple field environments can directly quantify variation in deep root traits to select wheat genotypes for breeding," *Journal of Experimental Botany,* vol. 65, no. 21, pp. 6231-6249, 2014.

[97] S. Mairhofer, S. Zappala, S. Tracy, C. Sturrock, M. J. Bennett, S. J. Mooney and T. P. Pridmore, "Recovering complete plant root system architectures from soil via X-ray micro computer tomography," *Plant Methods,* vol. 9, no. 8, 2013.

[98] R. Metzner, A. Eggert, D. V. Dusschoten, D. Pfugfelder, S. Gerth, U. Schurr and N. J. S. Uhlmann, "Direct comparison of MRI and X-ray CT technologies for 3D imaging of root systems in soil: potential and challenges for root trait quantification.," *Plant Methods,* vol. 11, no. 17, pp. 1-11, 2015.

[99] M. L. Grewel, "In situ magnetic resonance imaging of plant roots," *Vadose Zone Journal*, vol. 13, no. 3, pp. 1-8, 2014.

[100] C. Hillnhuntter, R. A. Sikora, C. Oerke and D. Van Dusschoten, "Nuclear magnetic resonance: a tool for imaging belowground damage caused by heterodera schachtti and rhizoctonia solani on sugar beet," *Journal of Experimental Bontony,* vol. 63, no. 1, pp. 319-327, 2012.

[101] B. H. Suits and D. E. Wilken, "Improving magnetic field gradient coils for NMR imaging," *Journal of Physics E.: Scientific Instrumentation*, vol. 22, no. 8, pp. 565-573, 1989.

[102] J. W. Eaton, D. Bateman, S. Hauberg and R. Wehbring, *GNU Octave version 5.1.0: a high level interactive language for numerical computatations*, https://www.gnu.org/software/octave/doc/v5.1.0/, 2019.

APPENDIX A

UAV AUTO EXPOSURE METADATA BUBBLE PLOTS

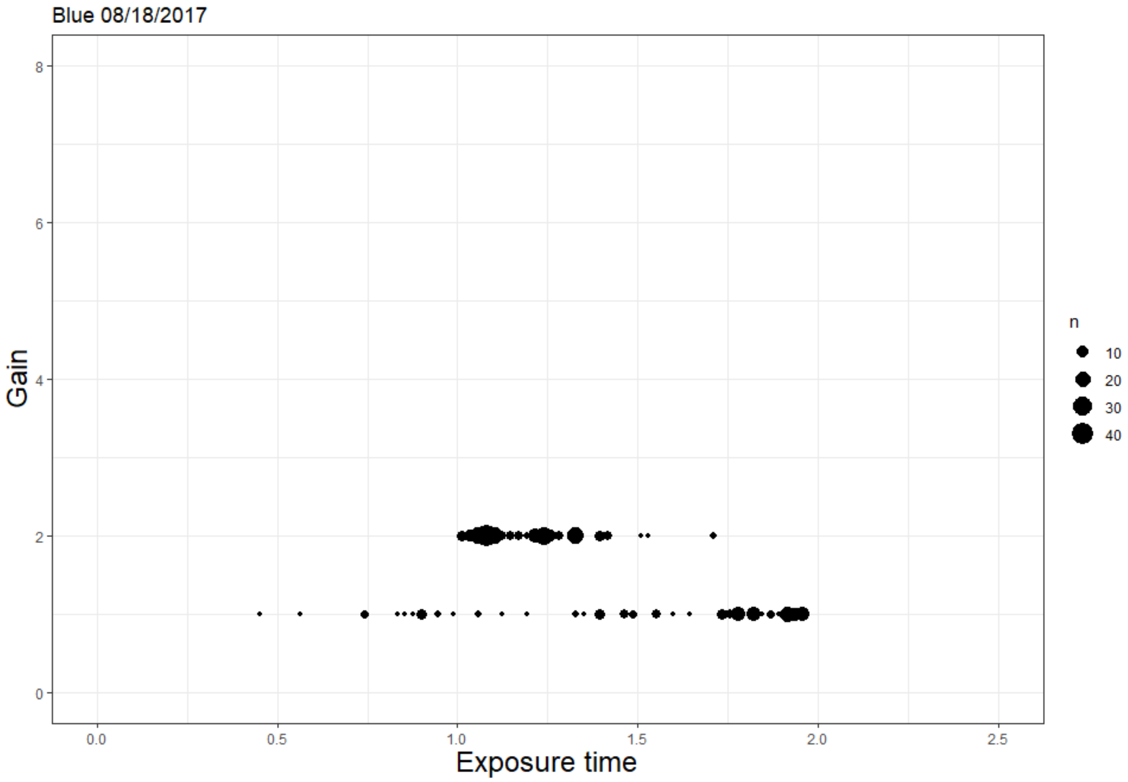

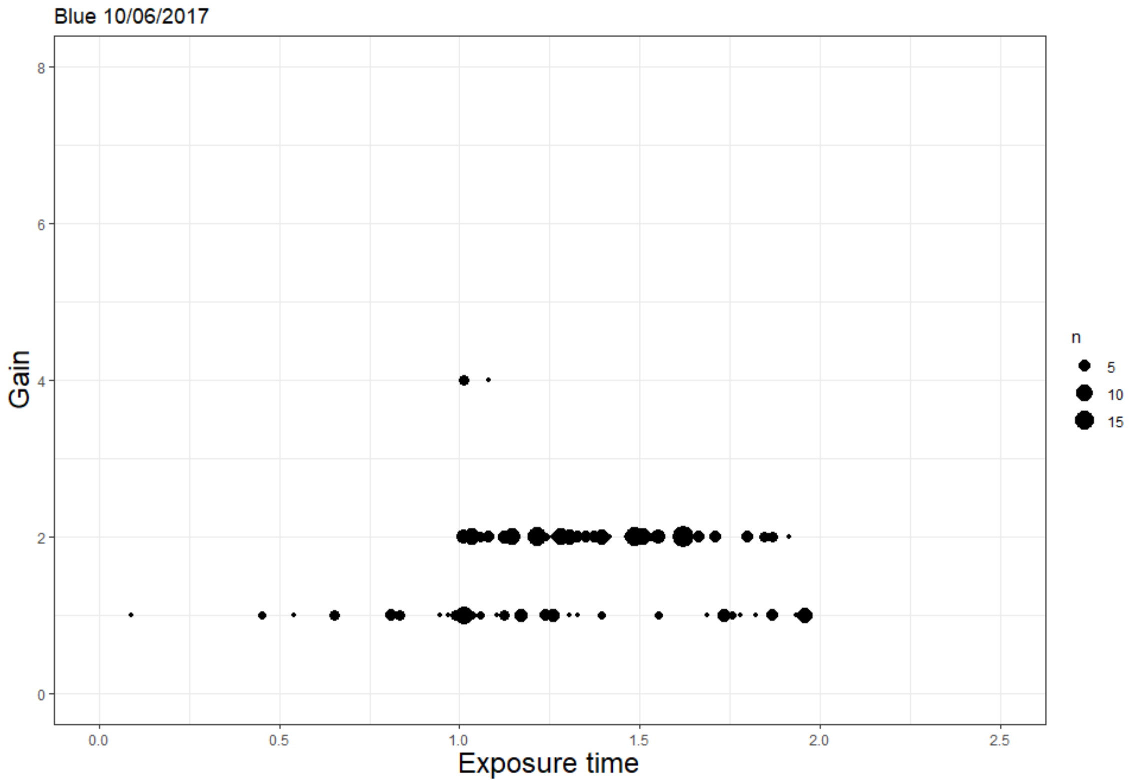
Blue 10/06/2017
Gain
0
2
4
6
8
Exposure time
0.0
0.5
1.0
1.5
2.0
2.5
n
5
10
15

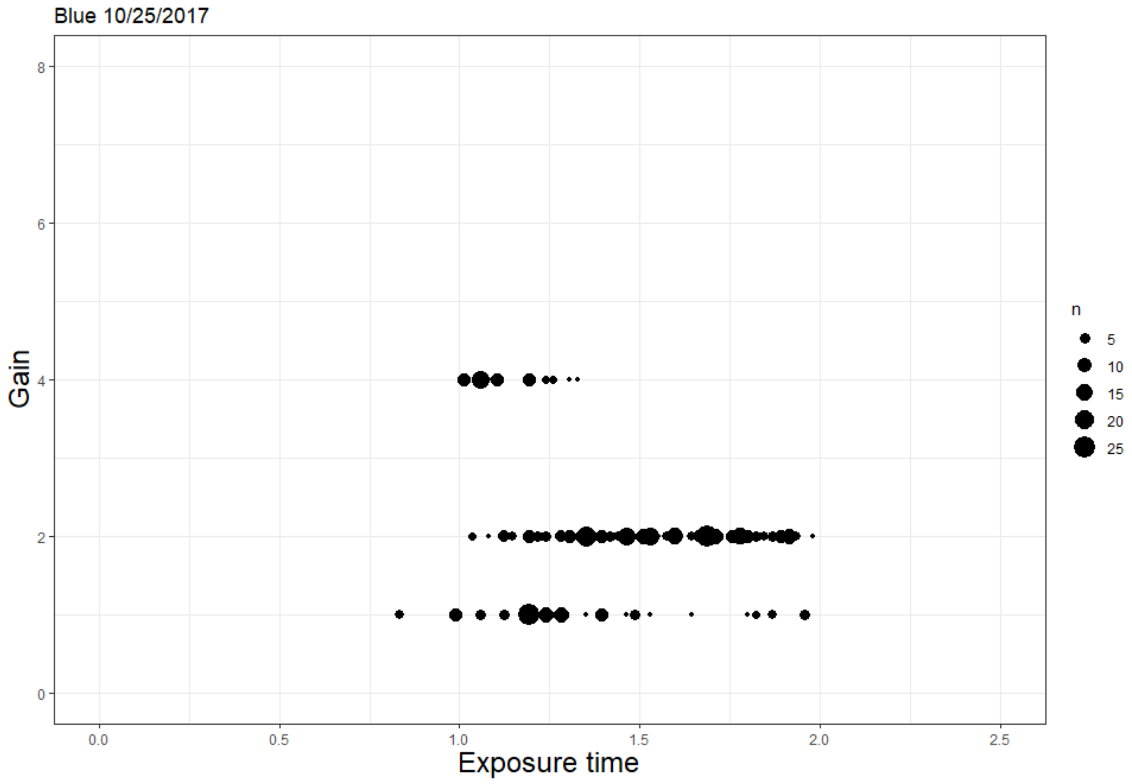
Blue 10/25/2017
Gain
0
2
4
6
8
Exposure time
0.0
0.5
1.0
1.5
2.0
2.5
n
5
10
15
20
25

Blue 11/30/2017

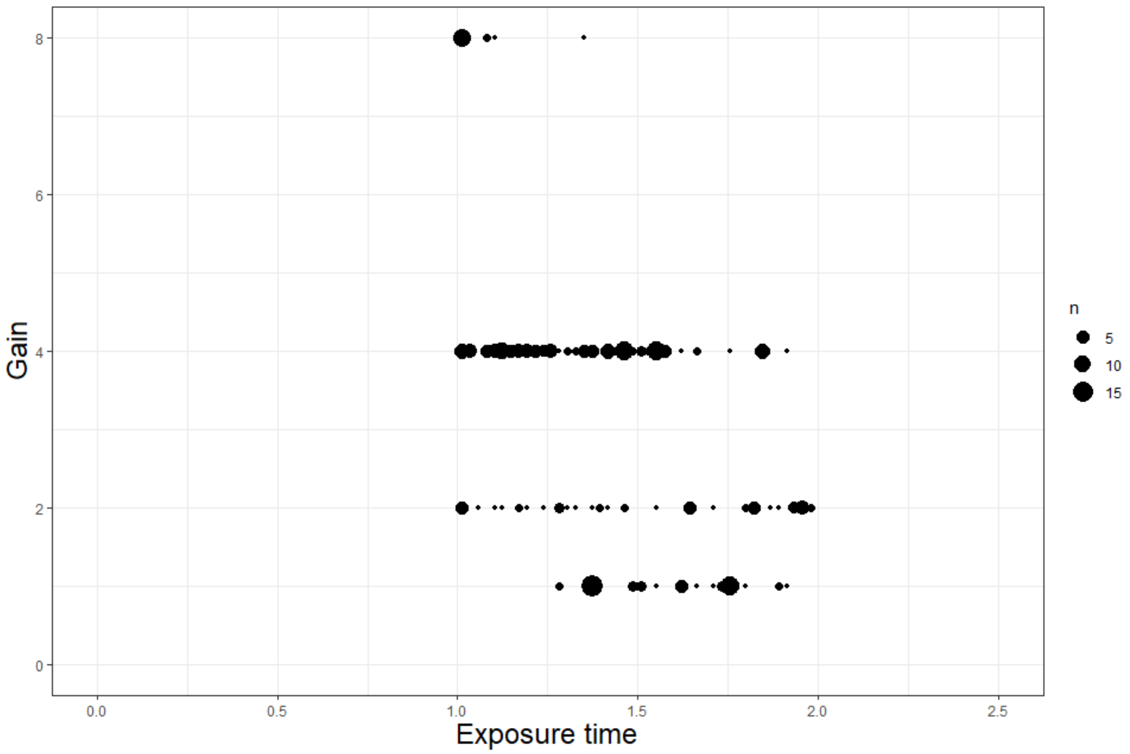

green 08/18/2017

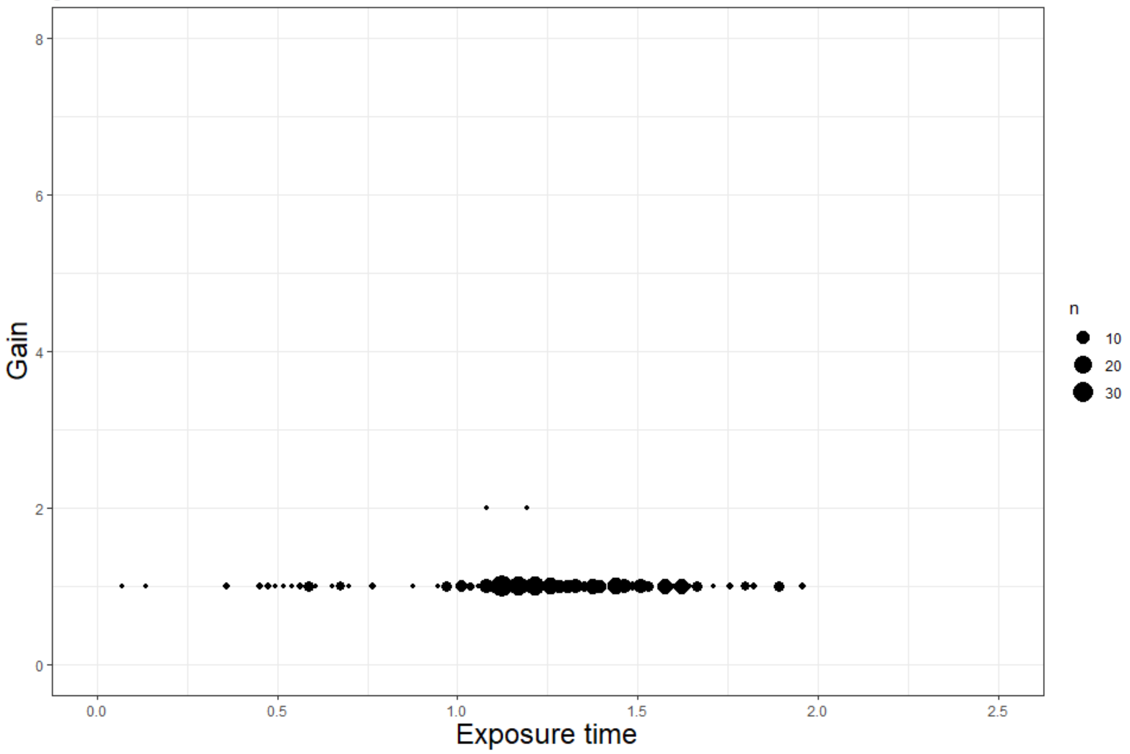

green 10/06/2017

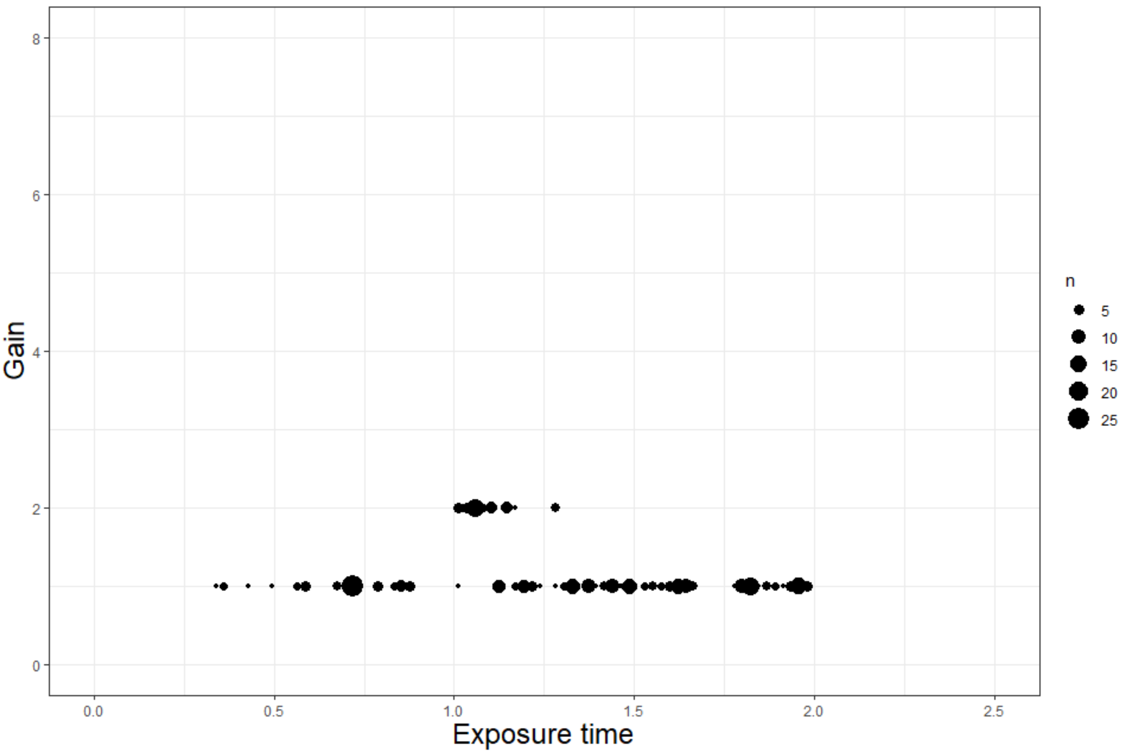

green 10/25/2017

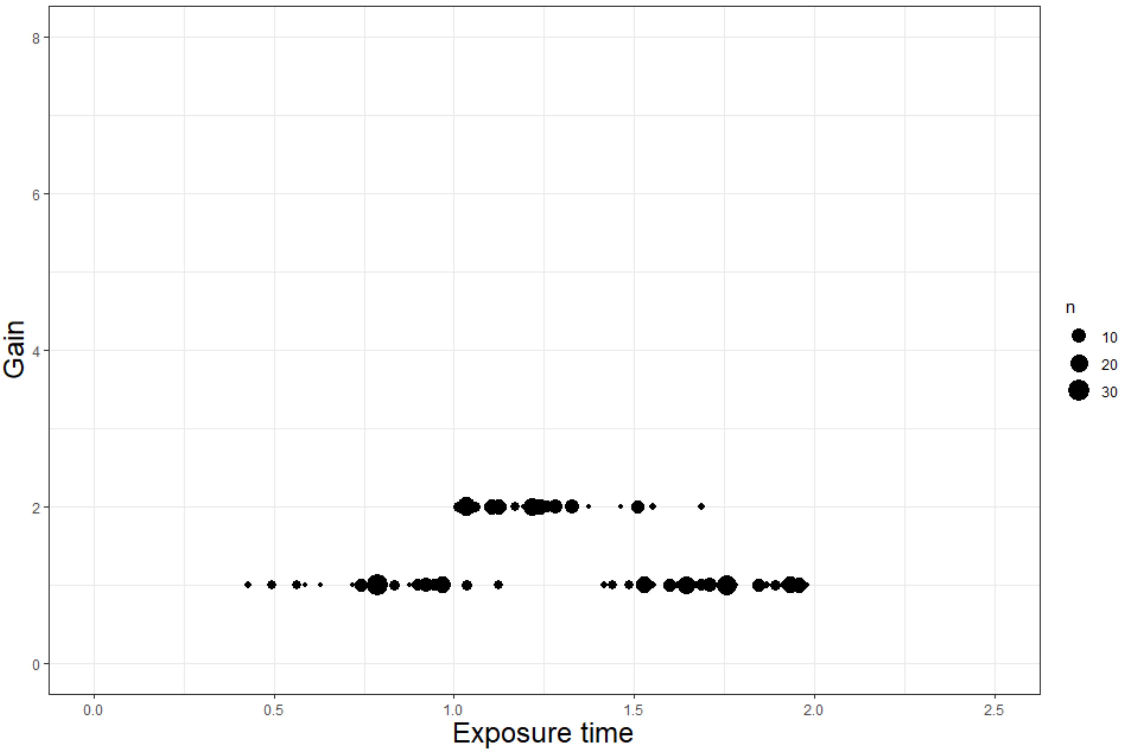

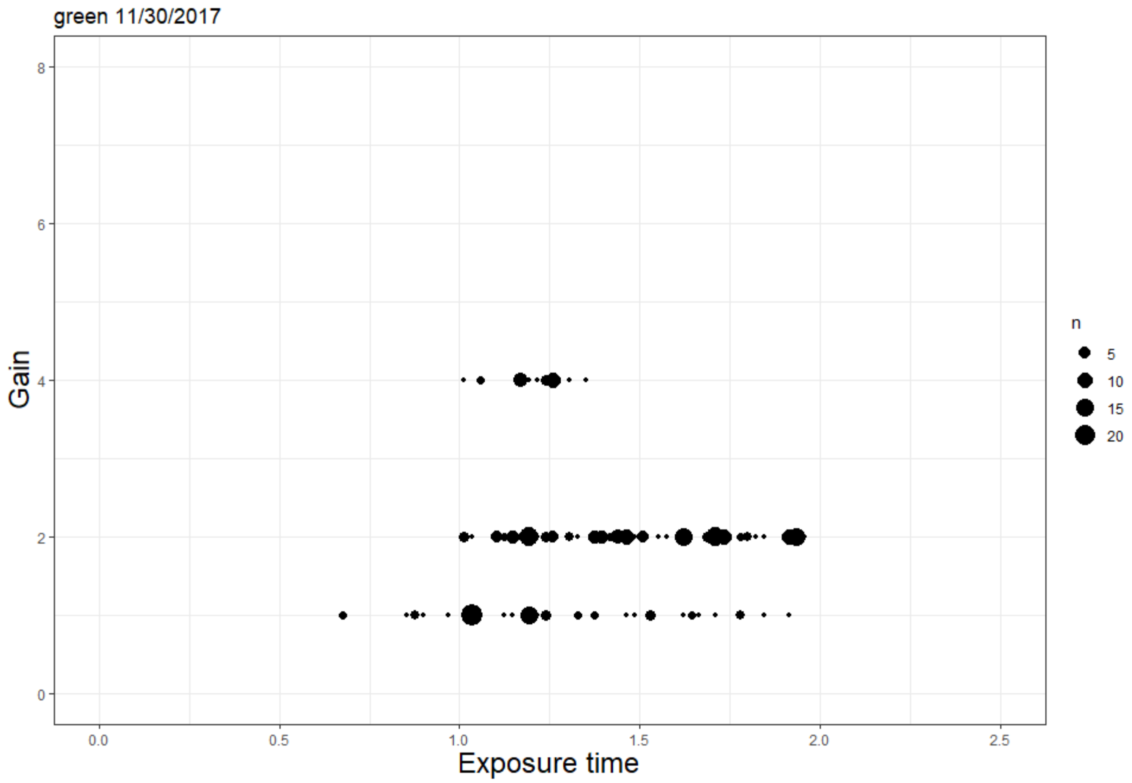
green 11/30/2017
Gain
Exposure time
0
2
4
6
8
0.0
0.5
1.0
1.5
2.0
2.5
n
5
10
15
20

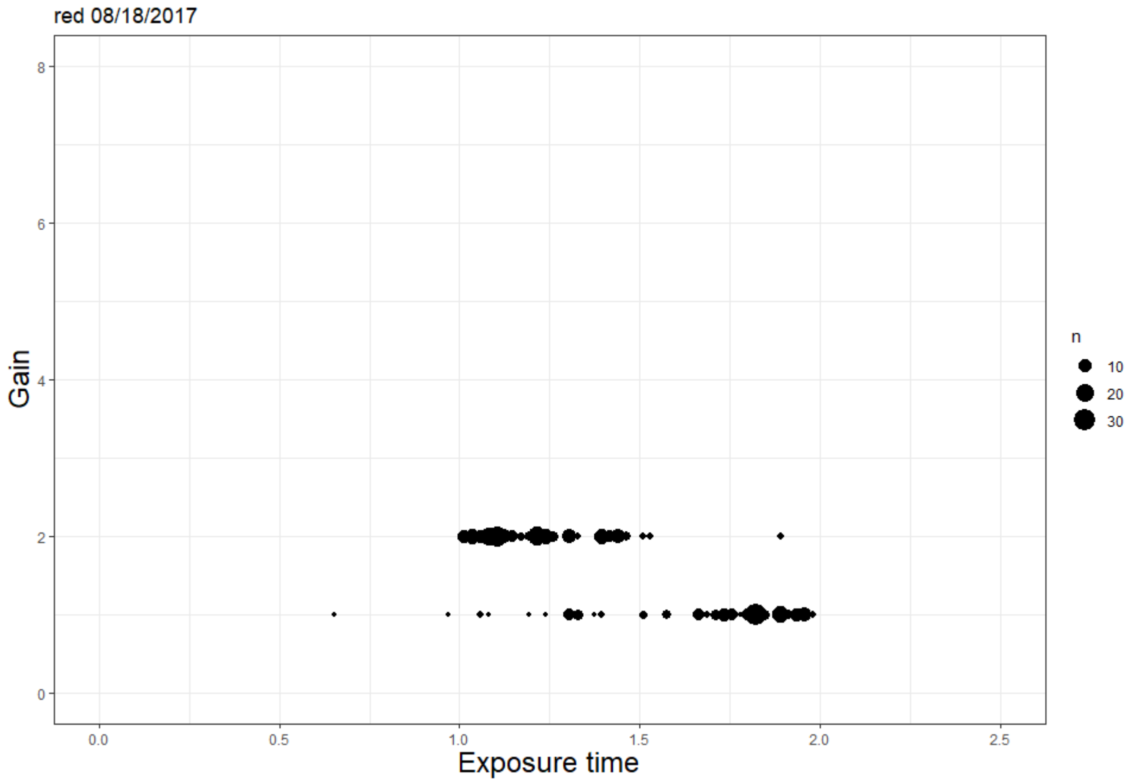
red 08/18/2017
Gain
Exposure time
0
2
4
6
8
0.0
0.5
1.0
1.5
2.0
2.5
n
10
20
30

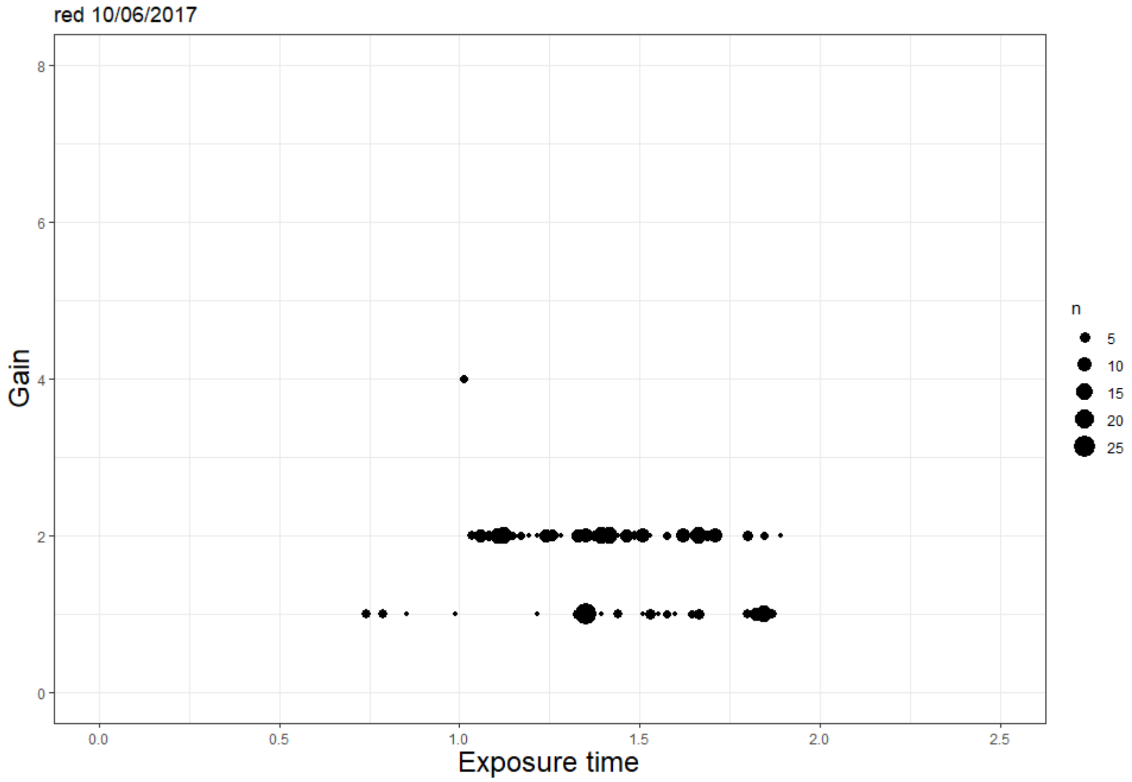
red 10/06/2017

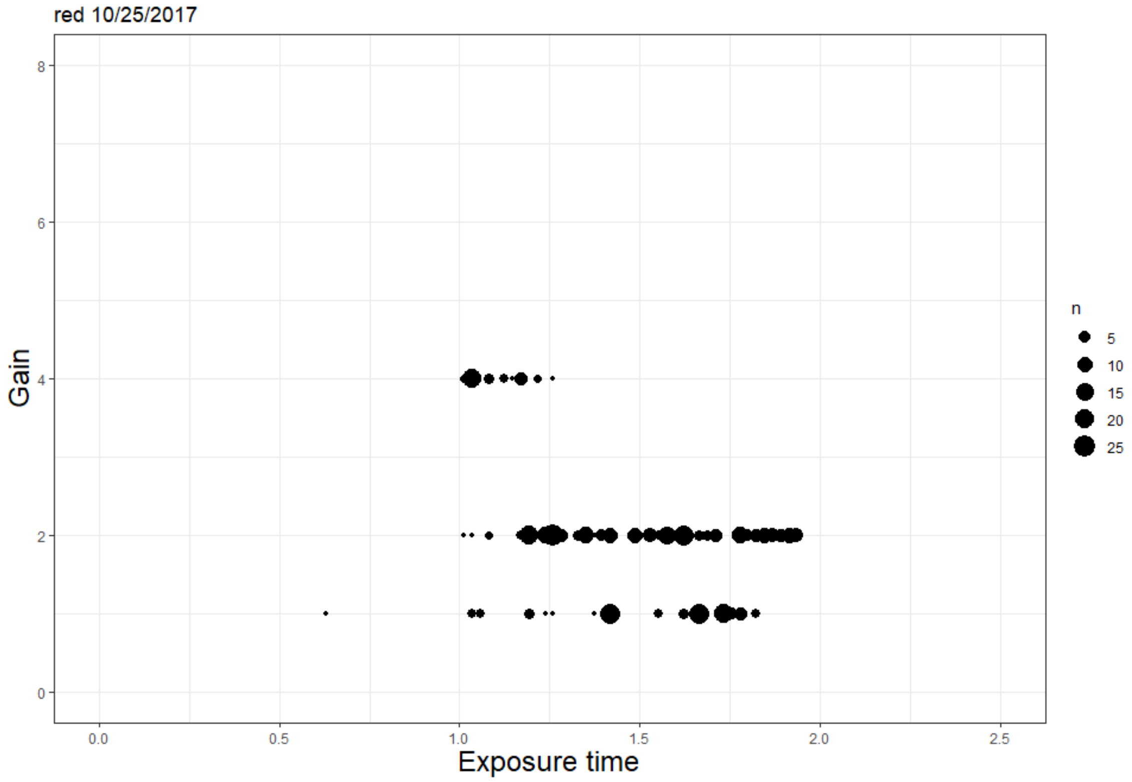
red 10/25/2017

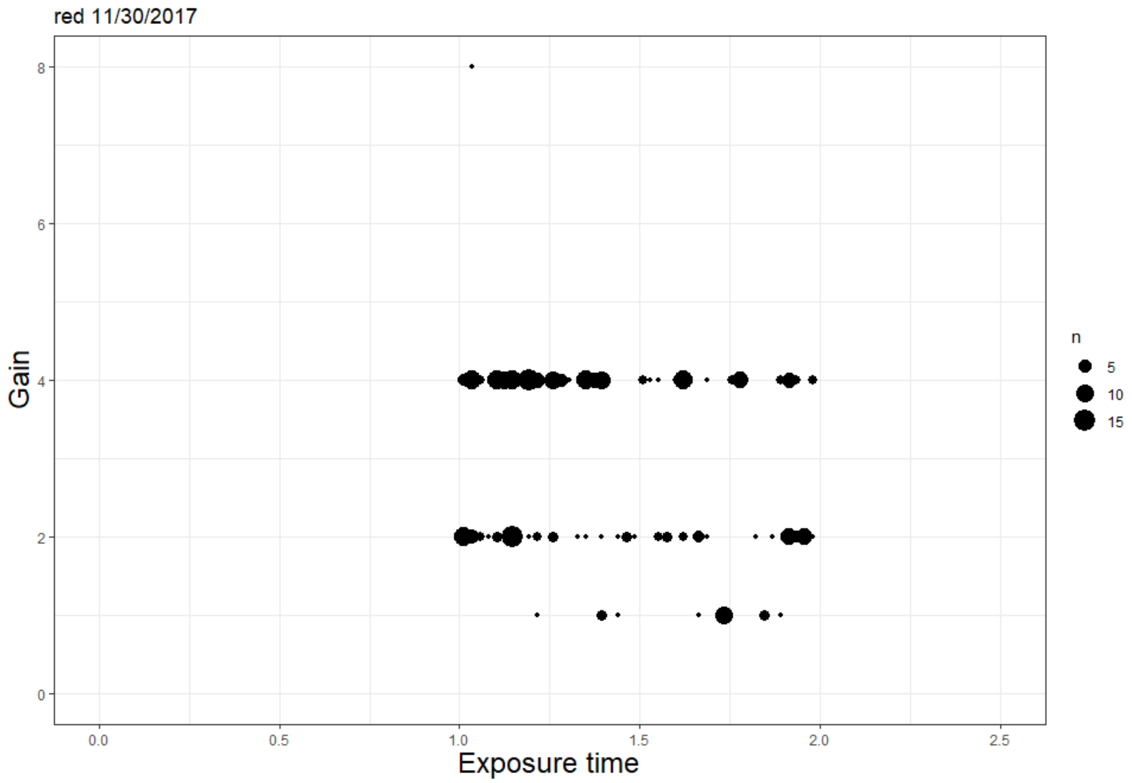
red 11/30/2017
Gain
8
6
4
2
0
0.0
0.5
1.0
1.5
2.0
2.5
Exposure time
n
5
10
15

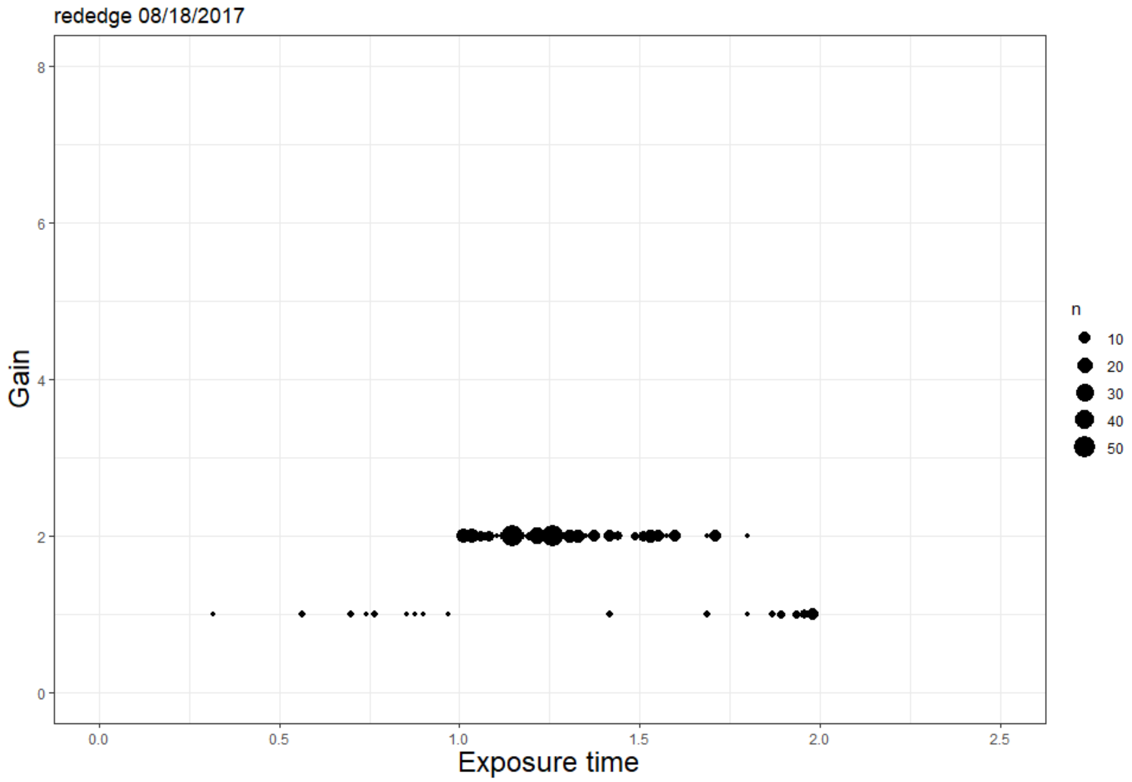
rededge 08/18/2017
Gain
8
6
4
2
0
0.0
0.5
1.0
1.5
2.0
2.5
Exposure time
n
10
20
30
40
50

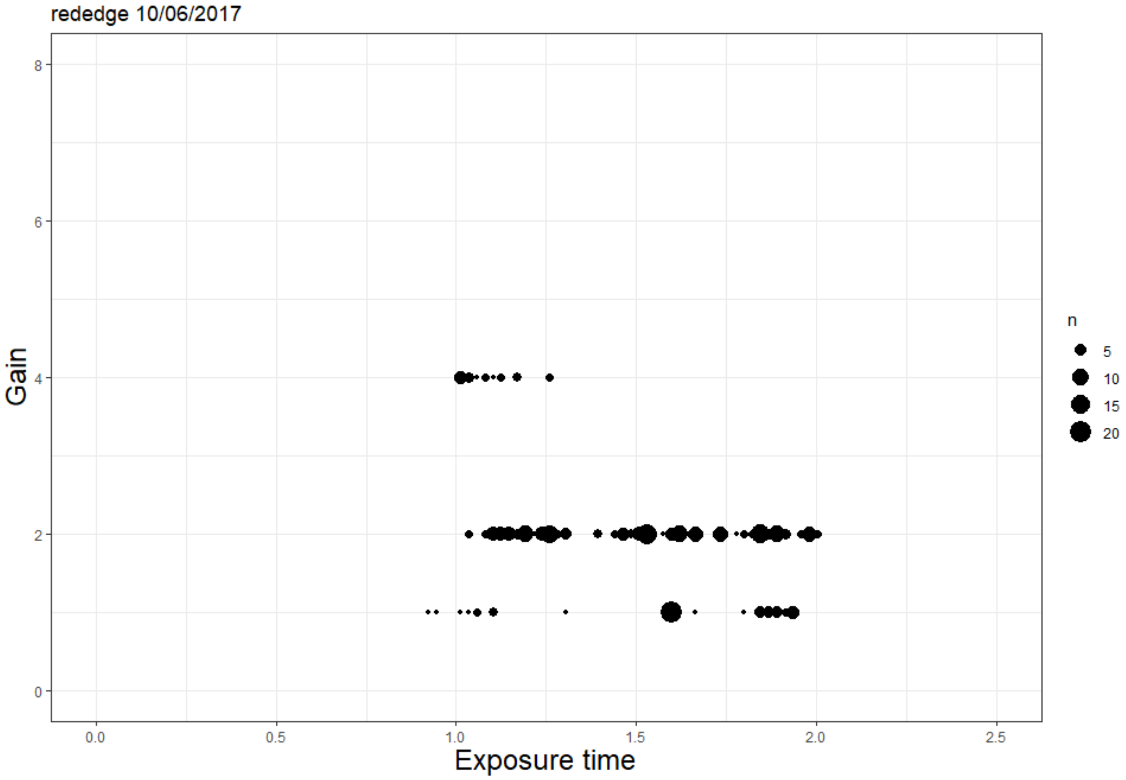
rededge 10/06/2017
Gain
Exposure time
0
2
4
6
8
0.0
0.5
1.0
1.5
2.0
2.5
n
5
10
15
20

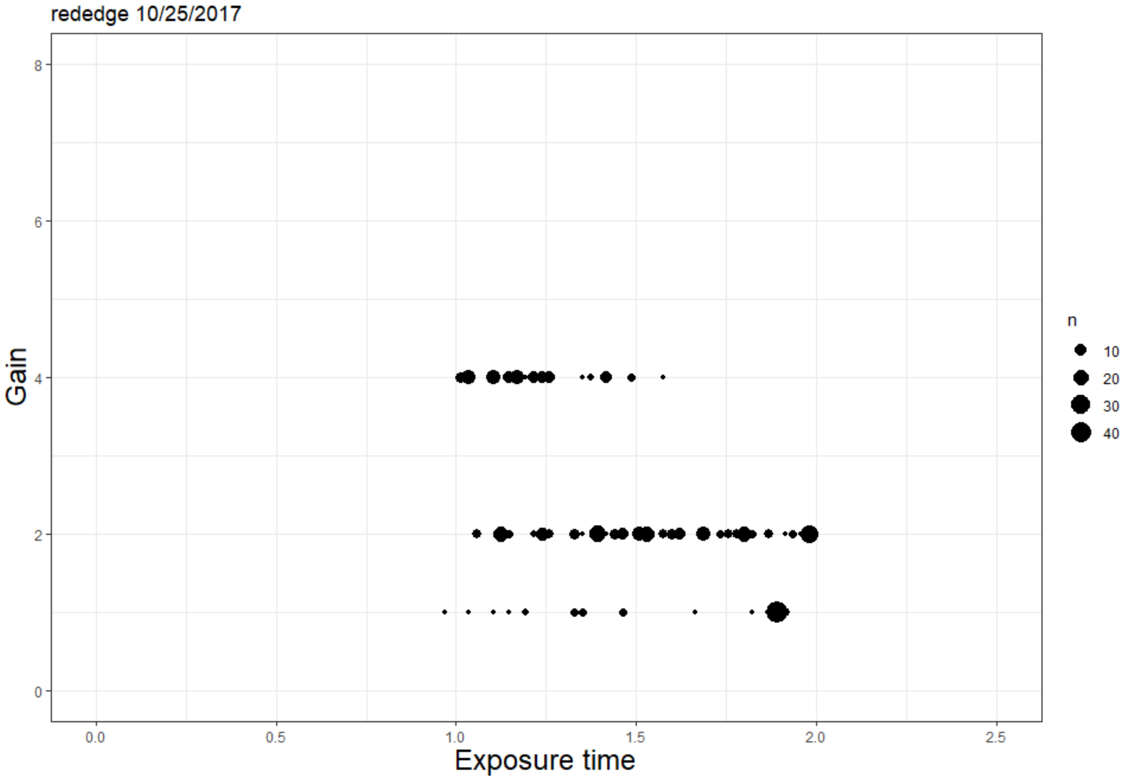
rededge 10/25/2017
Gain
Exposure time
0
2
4
6
8
0.0
0.5
1.0
1.5
2.0
2.5
n
10
20
30
40

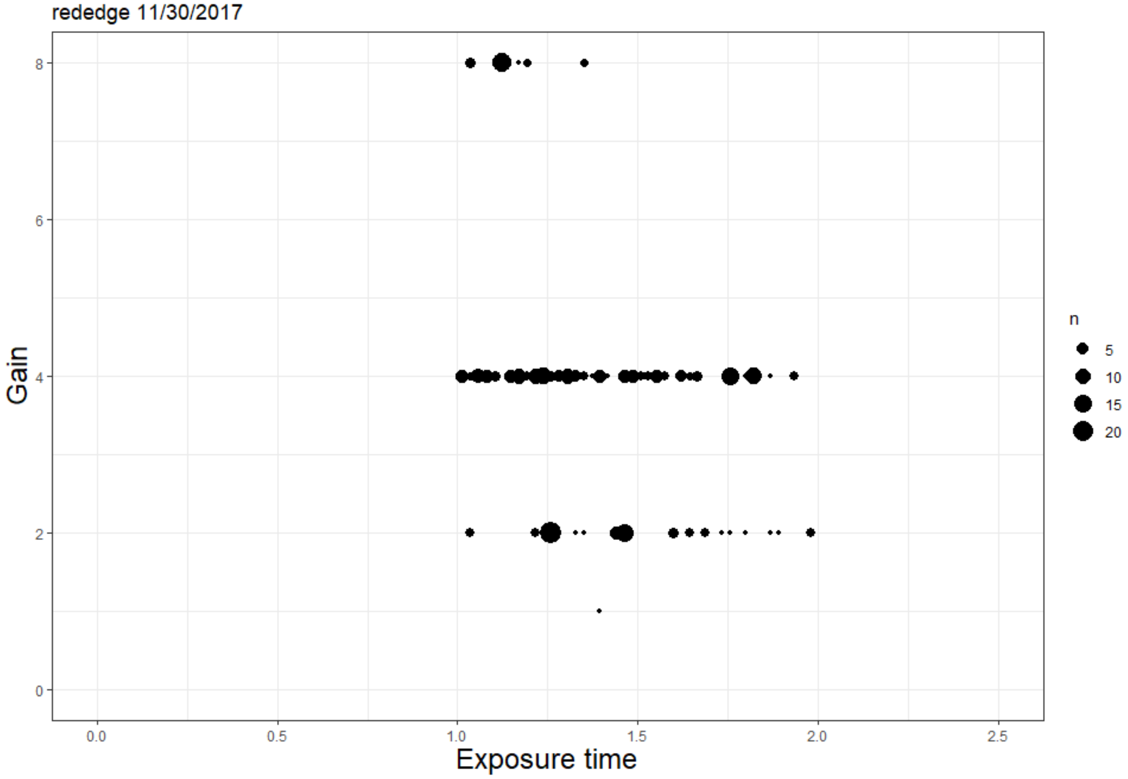
rededge 11/30/2017
Gain
Exposure time
0
2
4
6
8
0.0
0.5
1.0
1.5
2.0
2.5
n
5
10
15
20

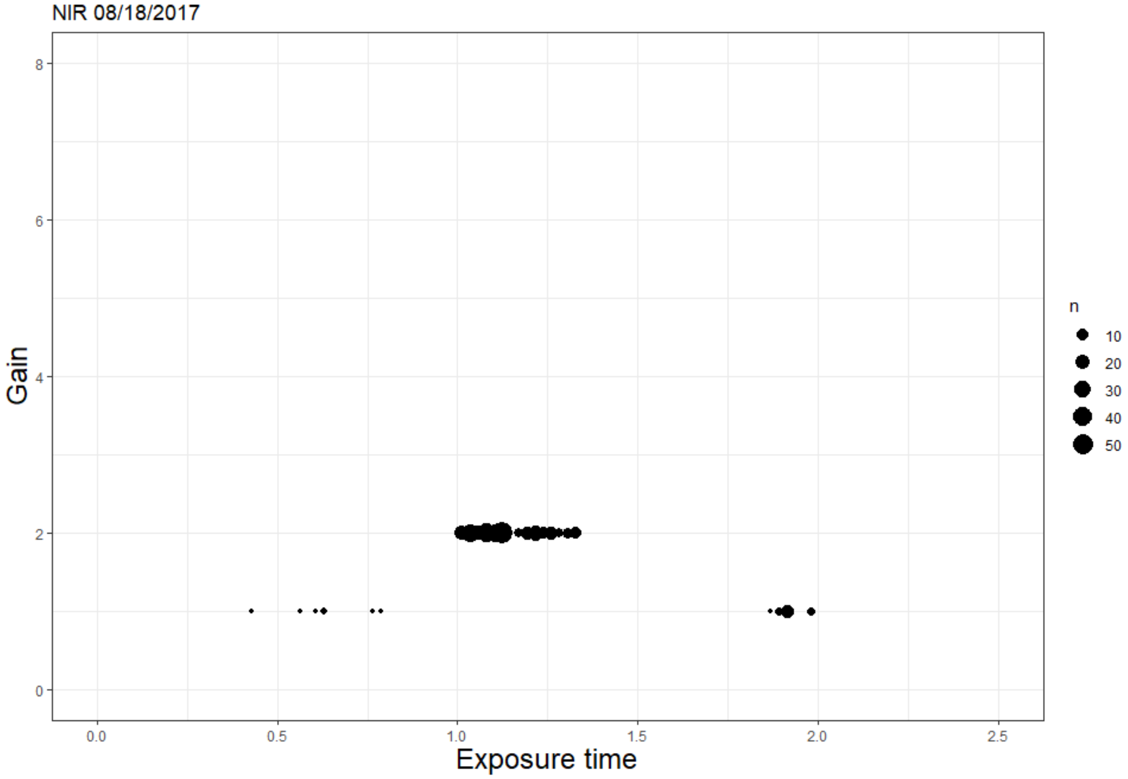
NIR 08/18/2017
Gain
Exposure time
0
2
4
6
8
0.0
0.5
1.0
1.5
2.0
2.5
n
10
20
30
40
50

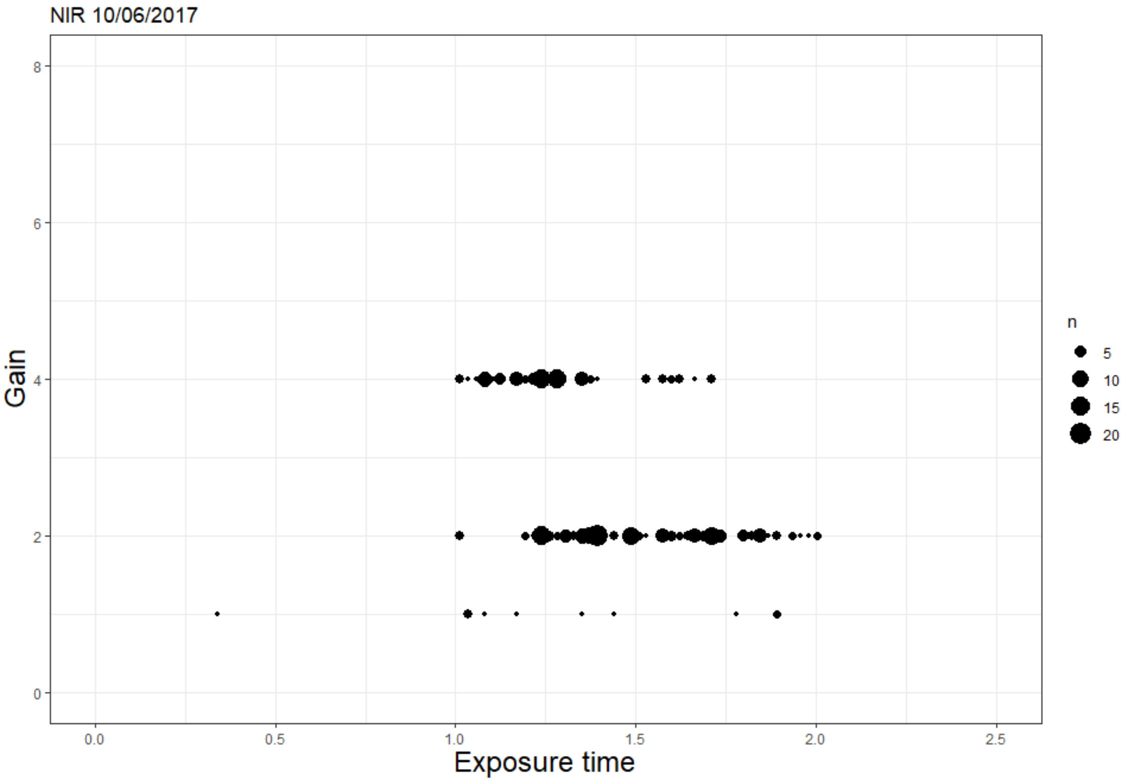
NIR 10/06/2017
Gain
8
6
4
2
0
Exposure time
0.0
0.5
1.0
1.5
2.0
2.5
n
5
10
15
20

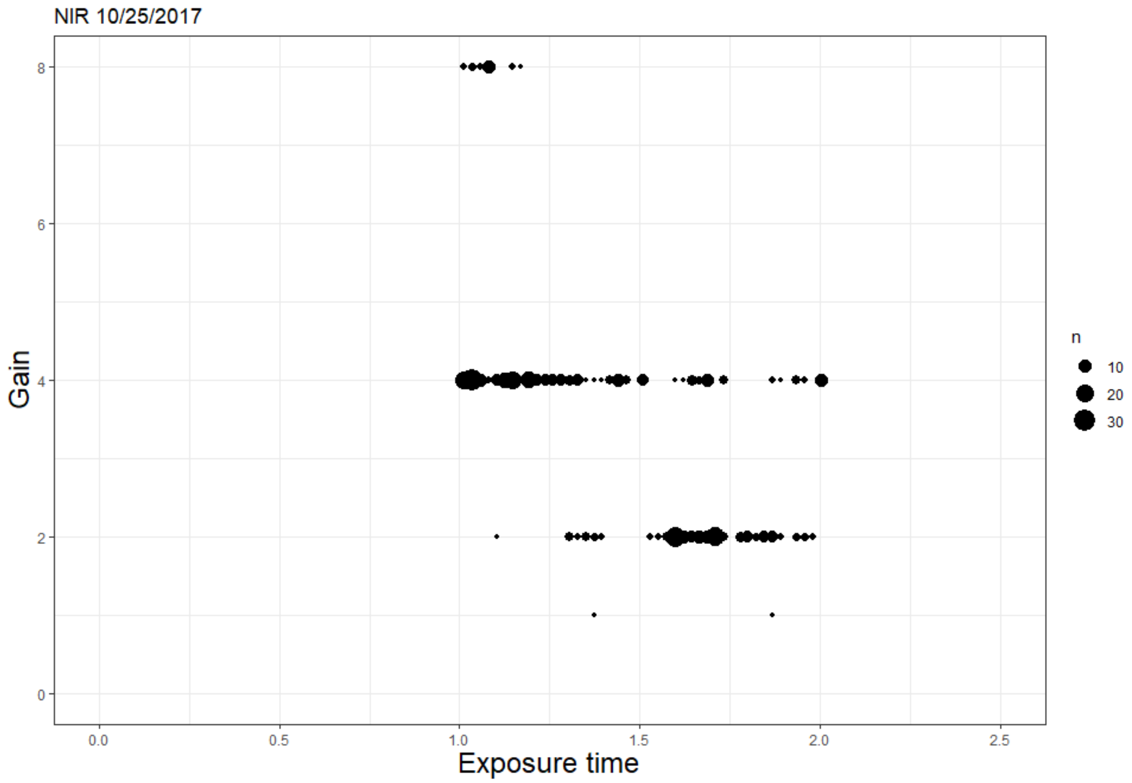
NIR 10/25/2017
Gain
8
6
4
2
0
0.0
0.5
1.0
1.5
2.0
2.5
Exposure time
n
10
20
30

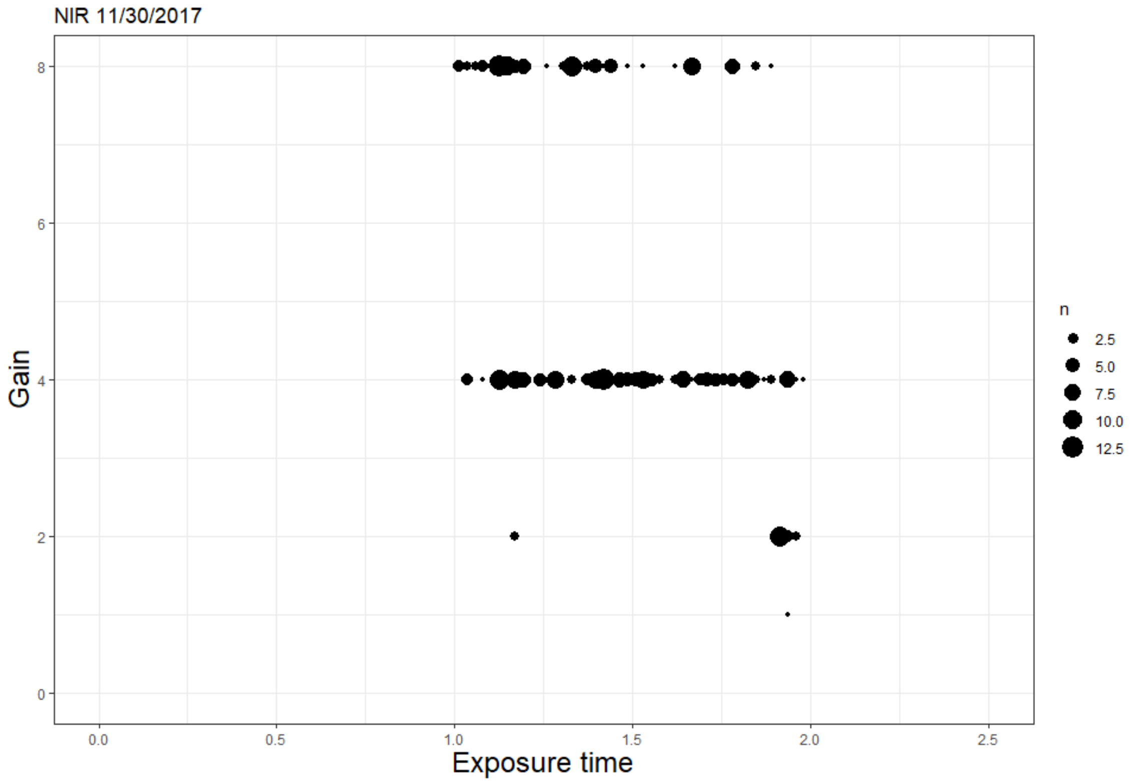
NIR 11/30/2017
Gain
8
6
4
2
0
0.0
0.5
1.0
1.5
2.0
2.5
Exposure time
n
2.5
5.0
7.5
10.0
12.5

APPENDIX B

LF-MRI ROOT BIOMASS LAB BASED CALIBRATION

Roots were weighted and measured using a 0-D scan on a 2 MHz, 8 cm bore LF-MRI system. The roots were dried and reweighted. Table 6-1 shows their signal strength and measured root metrics.

Table 0-1: Root fresh weight, dry weight and calculated root water along with the signal strength and T_2 relaxation time collected from bare root samples in the 8 cm bore LF-MRI.

Root ID	Wet Mass (g)	Dry Mass (g)	Water (g)	Weighted Sums	M_0	T_2 (ms)
CR-1	9.52	2.42	7.10	28929	4653	98.5
CR-2	10.45	2.77	7.68	43939	5494	149.8
CR-5	11.64	3.29	8.35	37279	4470	157.6
CR-6	22.68	6.67	16.01	57543	6606	169.6
L-3	4.56	0.72	3.84	23054	2814	152.3
L-5	9.49	1.39	8.11	53468	6692	147.9
L-6	2.82	0.42	2.40	16169	1925	161.6
L-9	2.28	0.25	2.04	15394	1691	184.1
M-1	4.34	0.80	3.54	17203	2300	133.8
M-3	7.11	1.14	5.97	35751	4859	128.8
M-4	8.41	1.33	7.08	44130	5311	157.3
M-5	3.34	0.51	2.84	18589	2166	166.3
M-6	3.11	0.47	2.64	14108	1959	126.8
PS-1	35.51	12.33	23.17	123994	14589	162.4
PS-2	4.37	1.26	3.11	20097	2432	158.0
PS-3	23.64	8.44	15.20	97037	12711	140.8
PS-4	27.25	10.18	17.08	75215	13746	85.6
PS-5	7.84	2.11	5.74	49260	4870	234.2
S-2	5.55	1.06	4.49	22869	3174	127.2
S-3	4.61	0.97	3.65	17867	2703	112.8
S-4	3.26	0.55	2.71	15723	2351	114.1
S-6	2.52	0.48	2.04	9350	1573	97.3
S-8	1.32	0.25	1.07	4795	802	100.7
VL-1	13.42	1.94	11.48	74482	8472	171.9
VL-3	18.78	2.88	15.90	100039	12209	150.1
VL-4	5.11	0.85	4.26	26341	3481	134.2
VL-5	7.48	1.26	6.23	41768	4950	161.0
VS-3	3.83	0.84	2.99	22124	3039	130.6
VS-4	10.17	2.71	7.46	65788	8681	139.3
VS-5	0.54	0.11	0.43	2456	390	107.2
VS-6	0.97	0.17	0.80	5497	817	116.0
VS-7	7.78	1.86	5.92	39235	5515	125.2
VS-8	7.82	1.59	6.22	45577	6025	138.3
VS-9	12.56	5.42	7.14	69780	9357	135.9

The root fresh weight was plotted as a function of the 0-D signal strength with good result. The RMSE is 3 g, and R^2 of 0.82. The two outliers are a partial sorghum stalk and a set of nodal roots. However, this relationship did not translate well into predicting root fresh weight in the field. It is possible that these two plant sections hold water differently than the smaller roots and contribute to the difficulty in using this model for field scans that include more of these types of plant sections.

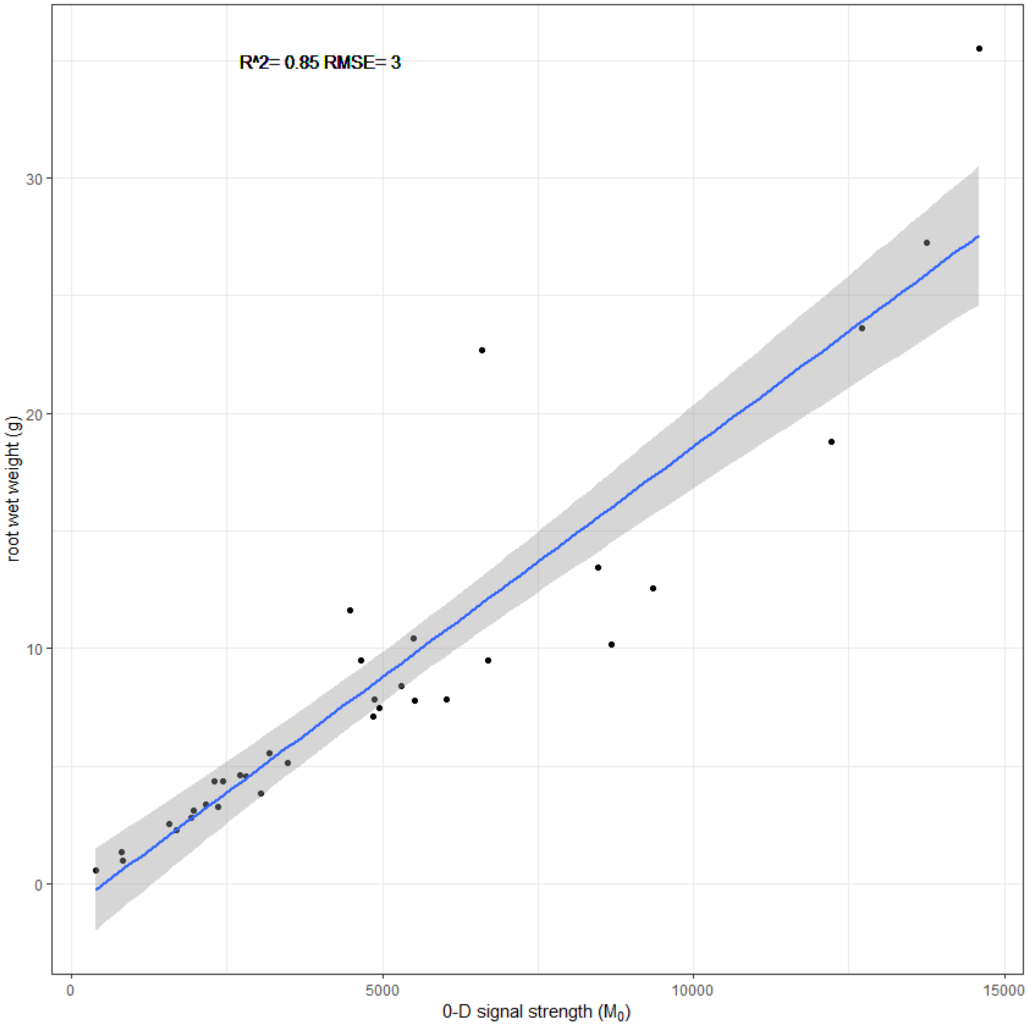

Figure 0-1: The root wet weight is plotted against the 0-D signal strength from bare roots using the 8 cm bore LF-MRI system. The R^2 and RMSE show promise but this equation did not predict root wet weight of field data.